INVESTIGATION OF ACOUSTIC WAVES UNDER SUBSURFACE CONDITIONS TO IMPROVE THE PREDICTIONS OF ROCK MECHANICAL PROPERTIES AND NATURAL FRACTURE CHARACTERISTICS

By

SHERIF ELKHOLY

Bachelor of Science in Petroleum Engineering
Cairo University
Cairo, Egypt
2010

Master of Science in Petroleum Engineering
Heriot-Watt University
Edinburgh, United Kingdom
2019

Submitted to the Faculty of the
Graduate College of the
Oklahoma State University
in partial fulfillment of
the requirements for
the Degree of
DOCTOR OF PHILOSOPHY
December, 2024

INVESTIGATION OF ACOUSTIC WAVES UNDER SUBSURFACE CONDITIONS TO IMPROVE THE PREDICTIONS OF ROCK MECHANICAL PROPERTIES AND NATURAL FRACTURE CHARACTERISTICS

Dissertation Approved:

Dr. Mileva Radonjic

Dissertation Chair

Dr. Hunjoo Peter Lee

Dissertation Advisor

Dr. Mohammed F. Al-Dushaishi

Committee Member

Dr. Daniel A. Laó-Dávila

External Committee Member

DEDICATION

"Allah raises those who have believed among you and those who have been granted knowledge, by degrees. And Allah is well-acquainted with all what you do." Al-Mujadala (58:11 Quran)

Dedication reflects the views of the author and are not endorsed by committee members or Oklahoma State University.

ACKNOWLEDGEMENTS

Completing a PhD is a long and rewarding journey, filled with countless nights of experimental work and a myriad of challenges. The path was marked by both failures and successes, each contributing to my growth as a researcher. The countless hours spent troubleshooting, analyzing data, and refining my experiments have shaped me into a, hopefully, more resilient and knowledgeable individual. This journey has been an extraordinary learning experience, one that I will carry forward in my future endeavors.

First and foremost, I would like to thank Almighty God for what He has granted, facilitated, helped, decreed, and favored. I dedicate this dissertation to my parents, whose unwavering support and love have been my foundation. My father, who passed away in 2015, only three months after immigrating from Egypt to the US, always provided honest and invaluable advice. Though he did not live to see me become a doctor, his wisdom and encouragement have guided me throughout this journey. To my mother, who has taken care of me since my first day of life, your sacrifices and endless support have been my driving force. This accomplishment is as much yours as it is mine.

I am deeply grateful to my advisor, Dr. Hunjoo Lee, for giving me the opportunity to join Oklahoma State University during the challenging COVID-19 times and for his unwavering support and guidance throughout my PhD. My heartfelt thanks also go to my committee members for their dedication and invaluable feedback. Special thanks to Dr. Mileva Radonjic, whose constant support and permission to join the Caney shale project have been instrumental. I also extend my gratitude to Dr. Mohammed Al-Dushaishi and Dr. Daniel Laó-Dávila for their support and insightful guidance. This dissertation would not have been possible without each of you.

Name: SHERIF ELKHOLY

Date of Degree: DECEMBER, 2024

Title of Study: INVESTIGATION OF ACOUSTIC WAVES UNDER SUBSURFACE CONDITIONS TO IMPROVE THE PREDICTIONS OF ROCK MECHANICAL PROPERTIES AND NATURAL FRACTURE CHARACTERISTICS

Major Field: PETROLEUM ENGINEERING

Abstract:
Mechanical properties and natural fracture characteristics are critical to investigate for subsurface engineering applications, including carbon storage, well drilling, and stimulation, as they govern rock stability, fluid flow, and mechanical behavior under stress. This dissertation integrates experimental and machine learning approaches to enhance the prediction and understanding of these properties by analyzing acoustic wave behavior under varied subsurface conditions. First, the influence of temperature, pore pressure, and supercritical CO_2 ($scCO_2$) saturation on poroelastic properties is examined using Gray Berea sandstone samples. The results show that temperature and pore pressure significantly affect the bulk modulus and Biot's coefficient, while $scCO_2$ saturation impacts rock compressibility, informing strategies for effective geological carbon storage. The study extends this understanding by experimentally evaluating the impact of reservoir depletion on the dynamic mechanical properties of the emerging Caney shale in South Oklahoma with the employment of unsupervised machine learning to predict static mechanical properties across the Caney shale. Integrating petrophysical data and chemostratigraphy, the workflow—featuring K-means clustering, principal component analysis (PCA), and inverse distance weighting (IDW)—improves stratigraphic characterization and the estimation of static-to-dynamic modulus ratios, which is vital for optimizing drilling and stimulation strategies. Finally, the work explores how natural fracture characteristics in shale influence acoustic waveforms and shear wave splitting (SWS) analysis. Experimental data on fractured samples under different stress and temperature conditions, combined with machine learning models such as K-nearest neighbors (KNN) and extreme gradient boosting (XGBoost), reveal key fracture properties impacting SWS and wave propagation. Together, these studies provide a comprehensive framework for linking acoustic wave behavior with rock properties, advancing the methods for monitoring and predicting geomechanical changes. The insights offered valuable implications for safer, more efficient CO_2 injection, hydrocarbon extraction, and subsurface management.

TABLE OF CONTENTS

Chapter Page

LIST OF TABLES

Table Page

LIST OF FIGURES

Figure Page

Figure Page

CHAPTER I

1 Introduction

1.1 Background and Motivation

Subsurface rocks exhibit a complex range of characteristics; while some formations are relatively intact and homogeneous, others are naturally fractured, presenting significant variability in their mechanical behavior (Alpay, 1972; Jones, 1987; Suarez-Rivera et al., 2005; Tang et al., 2018; Tavakoli, 2020). This complexity necessitates precise monitoring of mechanical properties, such as Young's modulus, Poisson's ratio, bulk modulus, and Biot's coefficient, particularly during production and injection applications (Alam et al., 2014; Ameen et al., 2009; Lamy-Chappuis et al., 2016; Pradhan et al., 2015; Sone and Zoback, 2013; Vidal et al., 2002). In addition, the characterization of natural fractures is crucial, especially in the vicinity of the wellbore, to avoid drilling and stimulation issues such as wellbore instability and fluid loss (Majidi et al., 2010; Razavi et al., 2017; Sanfillippo et al., 1997). These properties are essential in subsurface applications, including geologic carbon storage, hydrocarbon production, and well drilling and stimulation (Bratton et al., 2006; Gale et al., 2007). Accurate mechanical characterization ensures the stability and integrity of subsurface formations, optimizing operational efficiency and minimizing environmental risks.

In the context of geologic carbon storage, monitoring mechanical properties is essential for assessing the feasibility and long-term stability of injection zones. The mechanical integrity

of the storage site must be ensured to prevent leakage and ensure the safe containment of injected CO_2 (Rutqvist, 2012). Mechanical properties such as rock strength and deformation behavior under subsurface conditions are crucial in evaluating the potentialfor induced seismicity and caprock integrity. Accurate characterization and continuous monitoring of these properties can help in developing robust models to predict the behavior of the reservoir under different stress conditions, facilitating effective risk management (Yun and Song, 2022).

In unconventional shale reservoirs, good knowledge of mechanical properties (e.g., Young's modulus and Poisson's ratio) during production is critical to assess remaining hydrocarbon in place, and to better monitor surface deformation that might occur (King, 2012). In the meantime, natural fractures are abundant in unconventional reservoirs, significantly influencing the efficiency of hydraulic fracturing and subsequent oil and gas production. Detailed knowledge of fracture characteristics, including strike, dip, roughness, density, and aperture, is crucial for optimizing well placement and stimulation strategies. These fracture properties affect the propagation of induced hydraulic fractures and the overall connectivity of the fracture network, directly impacting hydrocarbon flow and recovery rates. Moreover, understanding fracture characteristics helps identify potential drilling hazards and mitigate issues such as wellbore instability and fluid loss during drilling. Thus, the objective of this dissertation is to enhance the knowledge of mechanical properties during oil production from Caney shale or CO_2 injection into Berea sandstone and natural fracture characteristics for Caney shale in the vicinity of wellbore through the incorporation of acoustic velocities measurement and machine learning.

1.2 Geologic Carbon Storage (GCS)

Recent climate change has drawn attention to low-carbon solutions, such as Geological

Carbon Storage (GCS), aimed at reducing the carbon footprint of the energy industry and thereby minimizing the risk of climate change (Cox et al., 2000; Meinshausen et al., 2009). This method involves injecting liquified CO_2 into deep sedimentary rock, typically high permeable sandstone formations within either a saline aquifer or a depleted reservoir (Bachu, 2008; Benson and Cole, 2008; Newell and Ilgen, 2019). The phase of CO_2 changes to a supercritical state ($scCO_2$) as it reaches the deep sedimentary reservoir, given that the downhole temperature and pressure are generally greater than 31°C (88 °F) and 1,070 psi, respectively (Juanes et al., 2006). The change in poroelastic properties, namely bulk modulus and Biot's coefficient, of the injection horizon during GCS controls its storage capacity and the fault stability near the wellbore (Ehlig-Economides and Economides, 2010; Rutqvist, 2012). However, there has been limited experimental investigation into the influence of pore pressure, temperature, and $scCO_2$ saturation on dynamic and static poroelastic properties, namely bulk modulus and Biot's coefficient, during GCS. In this dissertation, I am going to show how this influence has been investigated since it impacts both the storage capacity and fault stability near the wellbore during GCS.

1.3 Caney Shale Exploration in South Oklahoma

Shale plays have become essential reservoirs for oil production to meet global energy demands. Extracting hydrocarbons from these unconventional reservoirs requires a profound understanding of their mechanical properties, as these properties dictate critical aspects of extraction techniques, such as reservoir stimulation and long-term production sustainability (King, 2012). The mechanical behavior of the shale formations is governed by variations in mineral composition, organic content, and depositional history, which determine shale strength, brittleness, and fracture mechanical properties (Fjær et al., 2008). Previous studies have extensively focused on assessing how subsurface conditions, such as

temperature, saturation, loading conditions, composition, bedding orientation, and depositional facies impact the mechanical properties of shale formations (Sone and Zoback, 2013; Alqahtani et al., 2013; Rybacki et al., 2015; Dong et al., 2017; Tan et al., 2022; Guo et al., 2023; Xiong et al., 2023).

Recently, Caney shale has been evaluated for hydrocarbon production as an emerging unconventional reservoir in south-central Oklahoma (Cardott, 2017). As part of this evaluation, I will show in this dissertation how I evaluated the impact of effective stress changes due to oil production on Caney's dynamic mechanical properties (Young's modulus and Poisson's ratio) using acoustic velocities measurement under triaxial conditions. Also, the petrophysical data of Caney shale have been incorporated with triaxial testing using unsupervised machine learning to predict the static Young's modulus as a function of depth.

1.4 Natural Fracture Characteristics for Caney Shale

Natural fractures are abundant mechanical structures that exist in most rock types, especially in carbonates and shale (Moore and Wade, 2013). These pre-existing discontinuities could cause several drilling issues, including mud losses (Razavi et al., 2017) and drilling breaks (Narr et al., 2006). In production engineering, natural fractures may enhance the local permeability, hence the production rate (Luffel et al., 1993; Sakhaee-Pour and Bryant, 2011; Ben et al., 2012; Al-Rubaye et al., 2020). However, in the meantime, it can also increase the gas-oil ratio and water cut, impairing hydrocarbon productivity (Aguilera, 1980; Wennberg et al., 2016). Furthermore, in hydraulic fracturing applications, these natural fractures are known to have a significant impact on the hydraulic fracture trajectory and the Stimulated Reservoir Volume (SRV) depending on their relative orientation to the hydraulic fracture propagation direction (Gale et al., 2007; Zhou et al.,

2008; Bahorich et al., 2012; Lee et al., 2015).

This dissertation evaluated the impact of natural fracture characteristics on acoustic (i.e., P-wave, S1-wave, and S2-wave) velocities for Caney shale. Also, the KNN and XGBoost models have been utilized to predict the acoustic waveforms as a function of these characteristics. This evaluation helps infer the natural fracture characteristics for Caney shale from dipole sonic logs in the vicinity of the wellbore to better design the well drilling and stimulation programs in this newly explored shale.

1.5 Research Objectives

The objectives of this dissertation can be listed as below:

- Experimentally evaluate the impact of pore pressure and temperature changes on Berea sandstone's static and dynamic poroelastic properties, including Biot's coefficient and bulk modulus, during CO_2 injection and evaluate the impact of these changes on storage capacity and fault stability.
- Experimentally evaluate the impact of effective stress on dynamic Young's modulus and Poisson's ratio due to production for Caney shale.
- Predict static-to-dynamic Young's modulus ratio (F_{ds}) as a function of depth for Caney shale by conducting Inverse Distance Weighting (IDW) and Principal Component Analysis (PCA) on five (5) available F_{ds} measurements.
- Utilize K-means Clustering to categorize conventional well logs and XRF data for Caney shale and to compare it to its depositional facies column.
- Experimentally evaluate the individual impact of natural fracture characteristics (including strike, dip, and volume) on the acoustic P-wave, S1-wave, and S2-wave velocities for Caney shale and Eagle Ford shale under triaxial reservoir conditions.
- Predict the P, S-1, and S2 waveforms from the natural fracture characteristics and

reservoir conditions using K-nearest neighbors (KNN) and Extreme Gradient Boosting (XGBoost) models for Caney shale and Eagle Ford shale.

1.6 Dissertation Outline

The dissertation is made of five chapters. Chapter I introduces the research topics and the specific objectives of the dissertation. Chapter II discusses the effect of temperature and pore pressure on static and dynamic poroelastic properties during CO_2 Storage for Berea sandstone. Chapter III evaluates the impact of effective stress on Caney shale's dynamic mechanical properties during production and predicts the static Young's modulus for the whole Caney interval by integrating triaxial measurements and unsupervised machine learning methods. Chapter IV discusses how the acoustic (P-wave, S1-wave, and S2-wave) waveforms can be predicted as a function of natural fracture characteristics and subsurface conditions for Caney shale. Finally, chapter V discusses integrating the results with conclusions and future work.

1.6.1 Articles contributing to the main body of the dissertation

- **Kholy, S. M.**, Lee, H. P. 2024. Inferring Natural Fracture Characteristics in Shale Rocks from Acoustic Waveforms using Supervised Machine Learning. "Internal Review before Submission".
- **Kholy, S. M.**, Puckette, J. O., Lee, H. P. 2024. Predicting the Static-to-Dynamic Modulus Ratio from Petrophysical Data and Chemostratigraphy using Unsupervised Machine Learning. *SPE Journal* "Submitted and Under Review".
- **Kholy, S. M.**, Lee, H. P. 2024. Effect of Temperature and Pore Pressure on Static and Dynamic Poroelastic Properties during CO_2 Storage. "Internal Review before Submission".
- **Kholy, S. M.**, Lee, H. P., and Radonjic, M. 2024. Integrating Experiments and Well Logs to Predict Caney Shale Static Mechanical Properties during Production with Supervised Machine Learning. Paper presented at the Unconventional Resources Technology Conference held in Houston, Texas, USA.
- **Kholy, S. M.**, Lee, H. P. 2023. Experimental Investigation of Fracture Orientation in Rocks using Shear Wave Splitting. Paper presented at the 57th U.S. Rock Mechanics/Geomechanics Symposium, Atlanta, Georgia, USA. ARMA 23-0792.

1.6.2 Complete list of contributions since joining Oklahoma State University

- **Kholy, S. M.**, Lee, H. P. 2024. Inferring Natural Fracture Characteristics in Shale Rocks from Acoustic Waveforms using Supervised Machine Learning. "Internal Review before Submission."
- **Kholy, S. M.**, Puckette, J. O., Lee, H. P. 2024. Predicting the Static-to-Dynamic Modulus Ratio from Petrophysical Data and Chemostratigraphy using Unsupervised Machine Learning. *SPE Journal* "Submitted and Under Review."
- **Kholy, S. M.**, Lee, H. P. 2024. Effect of Temperature and Pore Pressure on Static and Dynamic Poroelastic Properties during CO_2 Storage. "Internal Review before Submission."
- **Kholy, S. M.**, Lee, H. P., and Radonjic, M. 2024. Integrating Experiments and Well Logs to Predict Caney Shale Static Mechanical Properties during Production with Supervised Machine Learning. Paper presented at the Unconventional Resources Technology Conference held in Houston, Texas, USA.
- **Kholy, S. M.**, Lee, H. P. 2024. Investigating the Impact of Reservoir Temperature Variation on the Geological CO2 Storage Capacity. Abstract virtually presented at the 12th Congress of the Balkan Geophysical Society, Kopaonik Mt., Serbia.

- **Kholy, S. M.**, Lee, H. P. 2024. Evaluating Acoustic Velocities to Monitor Poroelastic and Mechanical Properties of Gray Berea Sandstone during Geologic CO_2 Storage. Poster presented at the 2024 AAPG TechFest, Stillwater, Oklahoma, USA.
- **Kholy, S. M.**, Lee, H. P. 2023. Experimental Investigation of Fracture Orientation in Rocks using Shear Wave Splitting. Paper presented at the 57th U.S. Rock Mechanics/Geomechanics Symposium, Atlanta, Georgia, USA. ARMA 23-0792.
- **Kholy, S. M.**, Lee, H. P. 2023. Experimental Analysis of Dynamic Mechanical Properties for Caney Shale. Poster presented at the 2023 Caney Symposium, Oklahoma City, Oklahoma, USA.
- **Kholy, S. M.**, Lee, H. P. 2023. Identifying Lost-Circulation Zones from Shear Wave Slowness in Volve Field-North Sea using Machine Learning. Paper presented at the 2023 AADE National Technical Conference and Exhibition, Midland, Texas, USA. AADE-23-NTCE-047.
- **Kholy, S. M.**, Lee, H. P. 2023. Measurement and Prediction of P-Wave Velocity Under Anisotropic Stress Conditions for Synthetic and Actual Rocks. Poster presented at the 2023 GSA South Central Meeting, Stillwater, Oklahoma, USA.
- **Kholy, S. M.**, Lee, H. P. 2022. Inferring Compressional Wave (P-Wave) Travel Time from Conventional Well Logs using Supervised Machine Learning: Case Studies from Texas Basins. Paper presented at the 56th US

Rock Mechanics/Geomechanics Symposium, Santa Fe, New Mexico-USA. 26-29 June. Paper ARMA 22-0461.

CHAPTER II

2 Effect of Temperature and Pore Pressure on Static and Dynamic Poroelastic Properties during CO_2 Storage for Berea Sandstone

Abstract

In geological carbon storage (GCS), understanding the poroelastic properties of a reservoir is crucial for monitoring its integrity and storage. This study evaluates the static and dynamic poroelastic properties, namely bulk modulus and Biot's coefficient, for a water-saturated Gray Berea sandstone sample at initial reservoir condition, temperature of 80 °C, and various pore pressure values. This was done by measuring the changes in volumetric strain and acoustic velocities using a triaxial Hoek cell. Afterwards, carbon dioxide was injected into the sample at 50 °C to evaluate the same properties due to the near-wellbore cooling. Finally, the $scCO_2$ saturated sample was heated to the initial reservoir temperature of 80 °C to evaluate the same properties when the reservoir temperature stabilizes after long-term storage.

The experimental results suggest that the $scCO_2$ saturation does not have a clear impact on the Biot's coefficient, while it has a negative correlation with the derived bulk modulus due to the change in compressibility. The temperature negatively correlates with Biot's coefficient and the derived bulk modulus. The pore pressure is positively correlated with the Biot's coefficient and negatively correlated with the bulk modulus. The dynamic

to static correction factor generally showed a negative correlation with the pore pressure, while it had a positive correlation with the $scCO_2$ saturation. The findings of this study help understanding the impact of temperature, pore pressure, and $scCO_2$ saturation on the poroelastic properties and ultimately predicting the geomechanical issues associated with the injection process during GCS applications.

2.1 Introduction

Several geomechanical issues are associated with the GCS applications, including fault reactivation, induced strain and stress changes, and uplifting (Rutqvist, 2012). The injection zone pressurization might cause surface uplifting, as has been reported in the Salah GCS project in Algeria of 2.5 cm (Rutqvist, 2012), or as much as 20 cm in the Venice Lagoon in Italy (Comerlati et al., 2006). Also, this pressurization causes a continuous decrease in the local effective stresses around the injection source, which might yield an irreversible failure when the fracture pressure of the injection zone is exceeded (Rutqvist and Tsang, 2005). As the $scCO_2$ propagates away from the wellbore, it typically migrates upward and remains in contact with the cap rock due to buoyancy effects (Hesse et al., 2009). The loss of cap rock integrity might occur during GCS when the pore pressure exceeds the capillary pressure of the cap rock (Chadwick et al., 2008). Thus, it is important to comprehend the poroelastic properties of the reservoir and their evolution during the injection process to accurately assess alterations of in-situ effective stresses and rock strength during the GCS to mitigate these issues.

Previous studies utilized acoustic velocities from either seismic surveys or sonic logs to monitor CO_2 plume movement, fault stability evaluation, stress changes, or mechanical

properties changes during CO_2 injection (Zhou et al., 2009; Gilbert et al., 2010; Gutierrez et al., 2013; Falcon-Suarez et al., 2016; Piane and Sarout 2016; Agofack et al., 2018; Tarokh et al., 2020; Yun and Song 2022; Raziperchikolaee 2023). Gilbert et al. (2010) evaluated the strike-slip faults re-activation in the Naylor field due to the GCS into Waarre sandstone by incorporating the 3D seismic survey and computed stress path analytical solution. In addition, Gutierrez et al. (2013) utilized the acoustic velocities to monitor the CO_2 plume movement as they showed that the P-wave velocity kept decreasing for Berea sandstone sample during the displacement of water by $scCO_2$, while S-wave velocity was not affected. The same observations were noticed by Agofack et al. (2018) for Castlegate sandstone samples. Also, Yun and Song (2022) evaluated the acoustic waveforms for a water-saturated Berea sandstone sample to monitor the $scCO_2$ saturation, and they explained that the increase in $scCO_2$ saturation lowered the amplitude and raised the phase lag of the waveforms.

Tarokh et al. (2020) found that both the static and dynamic Young's moduli of Berea sandstone decreased by 15% after saturating them in $scCO_2$ for 22 days compared to the water-saturated sample. Zhou et al. (2009) showed that the $scCO_2$ injection lowered both the static and dynamic Young's modulus by 20-30% of Indiana limestone, while soaking the tested sample in $scCO_2$ for 4 days did not show clear changes in the rock strength. Similarly, Piane and Sarout (2016) presented that the $scCO_2$-saturated Berea sandstone samples exhibited a 20% decrease in elastic moduli at low pore pressures and a 50% decrease at high pore pressures compared to the water-saturated sample. Also, Falcon-Suarez et al. (2016) demonstrated that $scCO_2$-saturated synthetic sandstone sample had lower dynamic bulk and elastic moduli at room temperature compared to the water-

saturated sample. Furthermore, recent studies investigated the Biot's coefficient for GCS applications. Raziperchikolaee et al. (2020) experimentally evaluated the positive correlation between the pore pressure and the static Biot's coefficient for kerosene-saturated Brown Niagaran limestone samples at room temperature. The measurements were then incorporated into a numerical modeling simulator to evaluate the stress changes and possible uplifting during GCS. Also, Raziperchikolaee (2023) showed that the incorporation of Biot's coefficient to the effective stress in hydromechanical modeling yielded a larger uplifting magnitude compared to utilizing a fixed Biot's coefficient.

However, there has been limited experimental investigation into the effects of pore pressure, temperature, and $scCO_2$ saturation on both static and dynamic poroelastic and mechanical moduli during GCS. Therefore, the objective of this work is to comprehensively assess the impact of pore pressure on these properties, specifically Biot's coefficient and the bulk modulus, using Gray Berea sandstone samples at three distinct testing conditions: (1) fully water-saturated sample at of 80 ^{o}C and confining stress of 5,000 psi, (2) partially $scCO_2$ saturated sample at 50 ^{o}C, and (3) partially $scCO_2$ saturated sample at 80 ^{o}C. These testing conditions are designed to represent the initial reservoir state, the conditions shortly after CO_2 injection to evaluate the cooling effect, and the ultimate reservoir conditions once the temperature stabilizes after long-term storage, respectively. Lastly, the findings of this study were utilized to assess the storage capacity and in-situ stress changes during the CO_2 injection.

2.2 Materials and Methods

2.2.1 Static Biot's Coefficient and Bulk Modulus

Effective stress is a fundamental concept in poroelasticity, describing the distribution of external loads within a porous medium between the solid grains and the fluid-filled pores. It captures the interaction between the solid grains skeleton and pore fluid under applied loads, influencing the mechanical behavior of the subsurface materials. Terzaghi (1923) suggested the effective stress (σ) for unconsolidated sediments, which deform homogeneously as:

$$\sigma = P_c - P_p \tag{1}$$

where P_c is the confining pressure, and P_p is the pore pressure. Nur and Byerlee (1971) suggested the introduction of Biot's coefficient (α_p) to Terzaghi's effective stress to better describe the realistic rocks in the subsurface as:

$$\sigma_{eff} = P_c - \alpha_p P_p \tag{2}$$

The Biot's coefficient (α_p) is related to the bulk modulus (K_b) and the grain modulus (K_g) of the rock as (Geertsma, 1957; Skempton, 1984):

$$\alpha_p = 1 - \frac{K_b}{K_g} \tag{3}$$

However, Equation (3) is not suitable for rocks of heterogenous structure with several minerals (e.g., carbonates), and thus, Todd and Simmons (1972) suggested that the Biot's coefficient can be estimated based on the relative participation of confining and pore pressures on any physical characteristic (Q) as:

$$\alpha_p = 1 - \frac{\frac{\partial \sigma}{\partial Q}|_{P_p=const}}{\frac{\partial P_p}{\partial Q}|_{\sigma=const}} \tag{4}$$

Ma and Zoback (2017) utilized the volumetric strain (ε_v) as the physical characteristic parameter in Equation (4) and derived the static Biot's coefficient (α_p^{static}) as:

$$\alpha_p^{static} = 1 - \frac{\frac{\partial \sigma}{\partial \varepsilon_v}|_{P_p=const}}{\frac{\partial P_p}{\partial \varepsilon_v}|_{\sigma=const}} \quad (5)$$

where $\frac{\partial \sigma}{\partial \varepsilon_v}|_{P_p=const}$ represents undrained bulk modulus (K_b^{static}) and $\frac{\partial P_p}{\partial \varepsilon_v}|_{\sigma=const}$ represents the jacketed grain modulus (K_g).

Previous studies have discussed several methods for experimentally estimating Biot's coefficient. One method involves stepping up confining pressure at constant pore pressure, followed by increasing the pore pressure at constant confining pressure. Equation (2) is then applied by plotting σ_{eff} against ε_v, assuming an initial Biot's coefficient of 1, followed by a trial-and-error on the Biot's coefficient to obtain its optimum value that corresponds to the maximum R-squared of the plot (Kasani and Selvadurai, 2022). Another method utilizes the measurement of both undrained bulk modulus and jacketed grain modulus of the tested sample (Wang, 2000) along with Equation (5) to estimate Biot's coefficient. Undrained bulk modulus is determined by calculating the slope of the increasing σ against changes in ε_v at fixed pore pressure. In addition, jacketed grain modulus is estimated by calculating the slope of the increasing P_p against changes in ε_v at a fixed σ. In this study, we employed the second method to estimate the static poroelastic and mechanical moduli.

2.2.2 Dynamic Biot's Coefficient and Bulk Modulus

The dynamic Biot's coefficient ($\alpha_p^{dynamic}$) can be calculated from the acoustic P-wave velocity (V_p) by replacing ε_v in Equation (5) with V_p as (Asadollahpour et al., 2021):

$$\alpha_p^{dynamic} = 1 - \frac{\frac{\partial \sigma}{\partial V_p}|_{P_p=const}}{\frac{\partial P_p}{\partial V_p}|_{\sigma=const}} \quad (6)$$

where $\frac{\partial \sigma}{\partial V_p}|_{P_p=const}$ is the slope of σ versus V_p at constant P_p and $\frac{\partial P_p}{\partial V_p}|_{\sigma=const}$ represents the slope of P_p versus V_p at constant σ.

Nielsen and Kohlhaas (1979) demonstrated the use of acoustic compressional travel time (Δt_p) and shear travel time (Δt_s) to estimate formation mechanical properties. First, the velocity ratio (R_v) and the Poisson's ratio (v) are calculated from the given sonic logs as:

$$R_v = \frac{\Delta t_s}{\Delta t_p} \tag{7}$$

$$v = \frac{0.5R_v^2 - 1}{R_v^2 - 1} \tag{8}$$

The dynamic shear modulus (G), Young's modulus (E) and bulk modulus ($K_b^{dynamic}$) are estimated using,

$$G = 1.34 \times 10^{10} \frac{\text{RHOB}}{\Delta t_s^2} \tag{9}$$

$$E = 2G(1 + v) \tag{10}$$

$$K_b^{dynamic} = \frac{E}{3(1-2v)} \tag{11}$$

where the dynamic moduli are in psi, and the RHOB is the bulk density in g/cc, and Δt_s is in µsec/ft.

2.2.3 Sample Description

Lamy-Chappuis et al. (2016) discussed that water-saturated sandstone samples with calcite content ≥ 5 wt%, soaked in $scCO_2$ for 3 days, yielded a 4% reduction in compressive strength due to calcite dissolution. Similarly, Yang et al. (2023) showed that brine-saturated

sandstone with a calcite content of 11.6 wt%, soaked in $scCO_2$ for 2 days, exhibited a 6% drop in both tensile strength and the uniaxial compressive strength compared to the DI water-saturated sample under the same conditions. Their findings suggest that the brine accelerates the geochemical interaction between minerals and $scCO_2$.

For the long-term impact of CO_2 storage on reservoir integrity, the geochemical interaction between the CO_2 and the reservoir becomes important. However, in this study, we focused on the short-term response. Thus, to minimize the geochemical impact and concentrate solely on the geomechanical response to short-term CO_2 injection, we used Gray Berea sandstone obtained from an outcrop in Ohio, which has a relatively low calcite content of 2 wt% and a total clay content of 10 wt% (Table 1). It was selected since it is a typical porous, permeable medium ideal for GCS projects. Also, we saturated the Gray Berea sandstone samples with de-ionized (DI) water rather than brine.

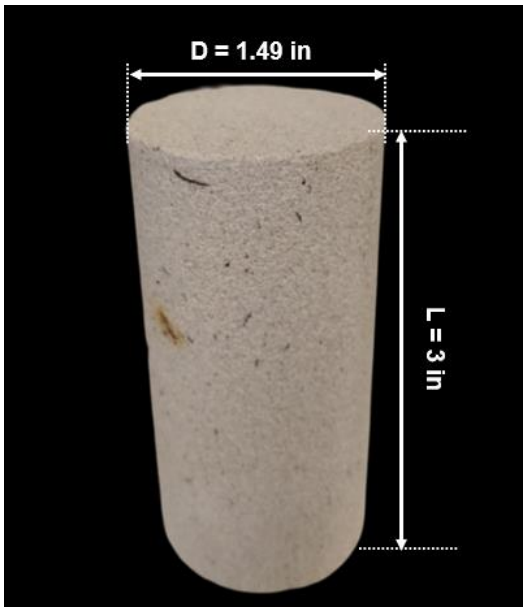

Figure 1: Tested Gray Berea sandstone sample.

The sample had a cylindrical shape, with dimensions of 3 inches in length and 1.49 inches in diameter, and a dry mass of 186 grams. The porosity was estimated at 19.95% by

dividing the mass difference between the dry and fully water-saturated samples by the total bulk volume. The permeability was measured to be 60 mD during the saturation process using DI water.

Table 1: Gray Berea sandstone mineralogical composition.

Mineral	Composition (wt%)	Grain Modulus (Mpsi)
Quartz	87	4.35 (Cataldo et al., 2022)
Kaolinite	6	0.73 (Mondol, 2008)
Albite	3	8.12 (Mondol, 2008)
Illite	2	2.18 (Mondol, 2008)
Calcite	2	8.41 (Cataldo et al., 2022)

2.2.4 Experimental Setup

The experimental setup of this study consisted of five main components, as shown in Figure 2.a: a loading frame, a triaxial Hoek cell, two ISCO syringe pumps, a box controller, a CO_2 cylinder, and a de-ionized (DI) water tank. The loading frame applied axial stress (S_1) on the cylindrical sample, which was placed vertically inside the triaxial Hoek cell after wrapping it with thermal duct tape to prevent contamination from the confining fluid. The Hoek cell was connected to two ISCO syringe pumps, one to regulate the confining pressure (P_c) and the other to control the DI water or CO_2 pore pressure (P_p) within the sample.

Radial strain was measured across the X and Y axes using four cantilever beam sensors surrounding the cell sleeve. In addition, axial strain was measured using two axial transducers mounted externally to the top piston at the front and back of the cell. The Hoek cell was also equipped with one compressional wave and two orthogonal shear wave piezoelectric transducers at each end of the tested sample (Figure 2.b) to measure both the

P-wave and S-wave velocities. The latter velocity represents the average of the two velocities from the two orthogonal shear transducers.

The box controller was utilized to deliver high-voltage electrical pulses to energize the transmitting transducers and capture both the transmitted and received waveforms, and to manage the cell temperature by heating the confining fluid.

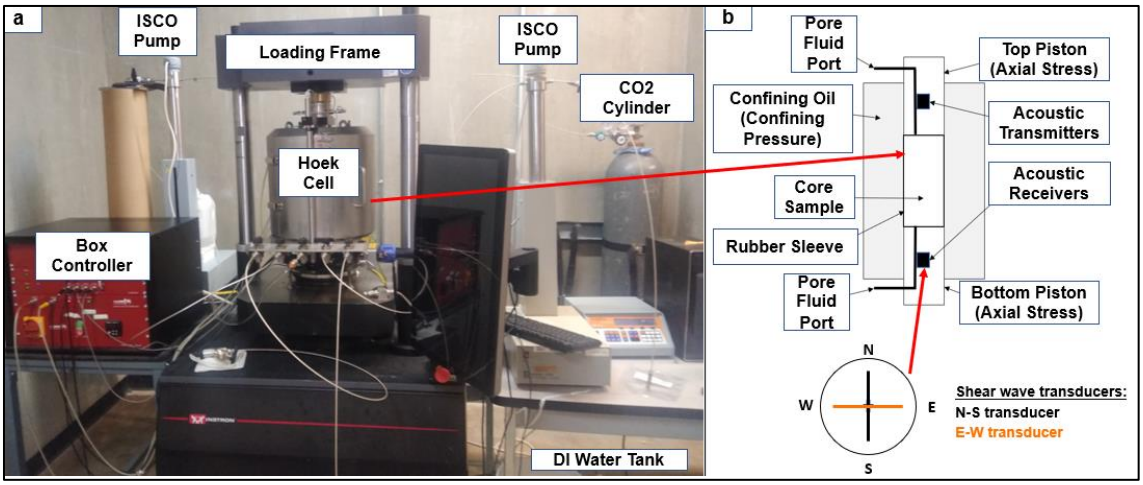

Figure 2: Experimental setup: (a) Main components and (b) Triaxial Hoek cell (after Kholy and Lee, 2023).

2.2.5 Experimental Procedures

DI Water Saturated Gray Berea Sandstone

To fully saturate the sample with DI water before the test, DI water was injected into the sample from the bottom through the pore fluid port of the Hoek cell (Figure 1.b). The top pore fluid port was kept open and connected to a bleeding bucket through transparent rubber tubing to monitor the displacement of air bubbles. The saturation process was completed after 45 minutes, when no more air bubbles were observed through the transparent tubing. The fully DI-water saturated sample will be referred to as H_2O-saturated sample in this study. After saturation, the top pore fluid port was closed to ensure an undrained condition, and the ISCO pump applied constant pore pressure through the

bottom port. Also, the temperature was raised to 80 °C to evaluate the measurements under initial reservoir conditions.

The K_g was measured following the jacketed testing procedure (Wang, 2000), summarized in Table 2. The confining pressure (P_c) was increased in four steps from 950 to 3,950 psi while increasing the P_p to keep the effective stress (σ) at 950 psi. It should be noted that the axial stress (S_1) was kept 50 psi higher than the P_c to avoid leakage of confining fluid into the sample. The K_b^{static} was measured following the undrained testing procedure, described in Table 3 (Wang, 2000), where the P_p was maintained constant, while P_c was increased in seven steps from 1,950 to 4,950 psi.

Table 2: Grain Modulus (K_g) testing schedule for the H_2O-saturated sample.

Step #	S_1 (psi)	P_c (psi)	P_p (psi)
1	1,000	950	0
2	2,000	1,950	1,000
3	3,000	2,950	2,000
4	4,000	3,950	3,000

Table 3: Static bulk modulus (K_b^{static}) testing schedule for the H_2O-saturated sample.

Step #	S_1 (psi)	P_c (psi)	P_p (psi)	T (°C)
1	2,000	1,950	0, 500, 1,000, 1,100, 1,500, 1,700, 2,300, 3,000 (H_2O)	80
2	2,500	2,450		
3	3,000	2,950		
4	3,500	3,450		
5	4,000	3,950		
6	4,500	4,450		
7	5,000	4,950		

The static Biot's coefficient (α_p^{static}) was then measured for each of P_p values using Equation (5). The P-wave and S-wave velocities were measured during each testing step

in Tables 2 and 3 to derive the corresponding dynamic Biot's coefficient ($\alpha_p^{dynamic}$) and dynamic bulk modulus ($K_b^{dynamic}$) using Equations (6) and (7-11), respectively.

scCO₂ Saturated Gray Berea Sandstone

The second sample was prepared by injecting liquified CO_2 into the fully H_2O-saturated sample. The liquified CO_2 was injected into the sample at a constant 800 psi from the top pore fluid port of the Hoek cell while keeping the bottom pore fluid port partially open to the atmosphere. This is done to easily displace the DI water from the sample utilizing the buoyancy force of the liquified CO_2 since it is lighter than water (Hesse et al., 2009).

Table 4: Measured density and saturation for dry, H_2O-saturated, and $scCO_2$-saturated samples.

Case #	Sample Mass (g)	Fluid Type	Bulk Density (g/cc)	H_2O Saturation (%)	CO_2 Saturation (%)
0	186	-	2.17	0.0	0.0
1	203.1	H_2O	2.369	100.0	0.0
2	194.5	H_2O+$scCO_2$	2.269	49.7	50.3

The saturation procedure lasted for 20 minutes, resulting in a CO_2 saturation of 50.3 %. The CO_2 saturation was calculated by dividing the difference between the mass of the CO_2-saturated sample and the mass of the dry sample by the difference between the mass of fully H_2O-saturated mass and the mass of the dry sample. We attempted to saturate the Gray Berea sandstone sample with CO_2 for 10 minutes, 20 minutes, and 45 minutes to achieve various CO_2 saturation conditions. However, based on our experimental setup, we only achieved CO_2 saturation of 50.3 wt% regardless of the saturation time. Previous studies experimentally found that the connate water saturation for Berea sandstone ranged between 40 wt% and 47 wt% (Garg et al., 1996; Shehata, 2016; Yun and Song, 2022). Thus,

the measured CO_2 saturation of 50.3% is possibly close to the maximum saturation for our Berea sandstone sample. Although the sample's pores were filled by both H_2O and CO_2, we will refer to this case as the $scCO_2$-saturated sample for convenience. During the test, pore pressure was maintained at or above 1,100 psi to satisfy the supercritical condition of CO_2. Table 4 summarizes the tested sample mass, bulk density, and CO_2 saturation values during parts one and two of the experiment.

After saturation, the bottom pore fluid port was closed, and the ISCO pump controlled the pore pressure through the top port. The temperature was initially set to 50 °C to evaluate the impact of reservoir cooling in the vicinity of the wellbore on the measured properties during the CO_2 injection. Subsequently, measurements were repeated at 80 °C to evaluate the same properties when the reservoir temperature stabilizes after the injection.

Table 5: Grain modulus (K_g) testing schedule for the $scCO_2$ saturated sample.

Step #	S_1 (psi)	P_c (psi)	P_p (psi)
1	2,000	1,950	1,100
2	2,300	2,250	1,400
3	2,600	2,550	1,700
4	2,900	2,850	2,000
5	3,200	3,150	2,300

Table 6: Static bulk modulus (K_b^{static}) testing schedule for the $scCO_2$-saturated sample.

Step #	S_1 (psi)	P_c (psi)	P_p (psi)	T (°C)
1	2,000	1,950	1,100, 1,700, 2,300 ($scCO_2$)	50, 80
2	2,500	2,450		
3	3,000	2,950		
4	3,500	3,450		
5	4,000	3,950		
6	4,500	4,450		
7	5,000	4,950		

The grain modulus, bulk modulus, and Biot's coefficient were measured following the same procedures described earlier for the H_2O-saturated sample. The main difference was in the testing schedule for the grain modulus, which maintained a constant σ of 850 psi, and the P_p was above the CO_2 critical state of 1,070 psi to ensure super-critical condition (Table 5). Bulk moduli were measured at P_p values of 1,100, 1,700, and 2,300 psi as listed in Table 6.

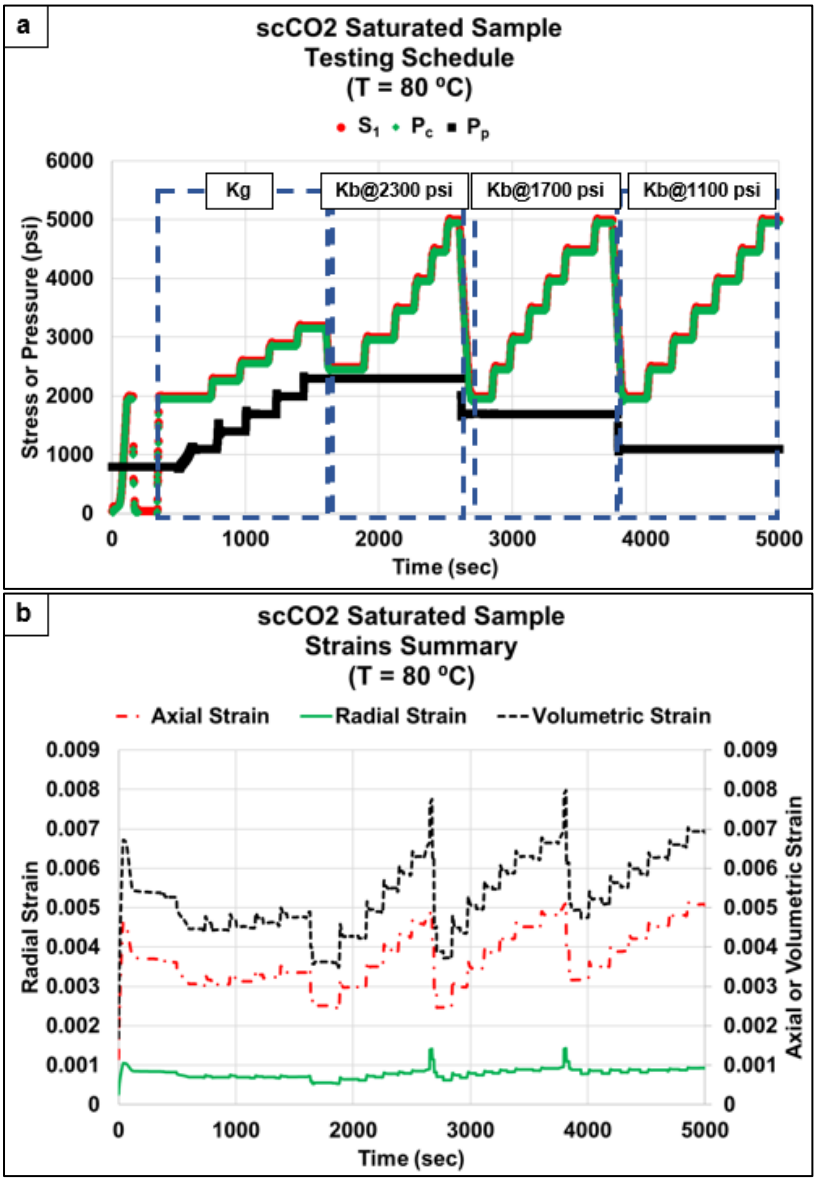

Figure 3: (a) Testing procedure for S_1, P_c, and P_p for the $scCO_2$ saturated sample at 80 °C. (b) Axial, radial, and volumetric strains summary of the shown testing schedule.

Figure 3 shows the overall testing schedule of S_1, P_c, and P_p for the $scCO_2$-saturated sample at 80 °C. In Figure 3.a, the first part in the dashed box corresponds to the K_g measurement and the subsequent sections are for the bulk modulus measurements at each P_p condition. Figure 3.b shows the corresponding axial strain (ε_a), radial strain (ε_r), and the derived volumetric strain (ε_v), where ε_v is ε_a plus two times ε_r, $\varepsilon_v = (\varepsilon_a + 2\varepsilon_r)$.

2.3 Results

2.3.1 Static Measurements

First, the K_b^{static} measurement of the fully H_2O-saturated sample was validated and compared with previous studies (Hart and Wang, 1995; Raziperchikolaee, 2023) to ensure measurement accuracy (Figure 4.b). This was achieved by evaluating the slope of the σ versus ε_v for pore pressure values of 0, 500, 1,000, 1,500, and 3,000 psi at a room temperature of 21 °C. The measured K_b^{static} ranged between 0.81 and 1.2 Mpsi, and it showed a negative correlation with P_p, presumably due to the inflation of pores (Figure 4.a). These results were comparable to measurements conducted by Hart and Wang (1995) and Raziperchikolaee (2023) on water-saturated Berea sandstone samples at room temperature (21 °C) (Figure 4.b). The decline rate of K_b^{static} with respect to P_p from our measurements fell between the trends reported by the other two studies, possibly due to our sample porosity, 19.95%, being close to the average of the other two reported porosities: 19% (Hart and Wang, 1995) and 21% (Raziperchikolaee 2023).

Second, the K_g measurement of the fully H_2O-saturated sample was validated at 21 °C by comparing it to Voigt-Reuss-Hill model (Hill, 1952) which utilized the weight fractions (wt) and grain moduli (K_g) of the individual minerals of the tested sample (Table 1) using

Equations 12-14, where K_v, K_R, and K_{VRH} are Voigt, Reuss, and Hill grain moduli, respectively. The Voigt-Reuss-Hill model yielded a K_{VRH} value of 3.75 Mpsi, which was close enough from the measured K_g at 3.51 Mpsi.

$$K_v = \sum_{i=1}^{n} wt_i K_{gi} \tag{12}$$

$$K_R = 1/\sum_{i=1}^{n} \frac{wt_i}{K_{gi}} \tag{13}$$

$$K_{VRH} = \frac{K_V + K_R}{2} \tag{14}$$

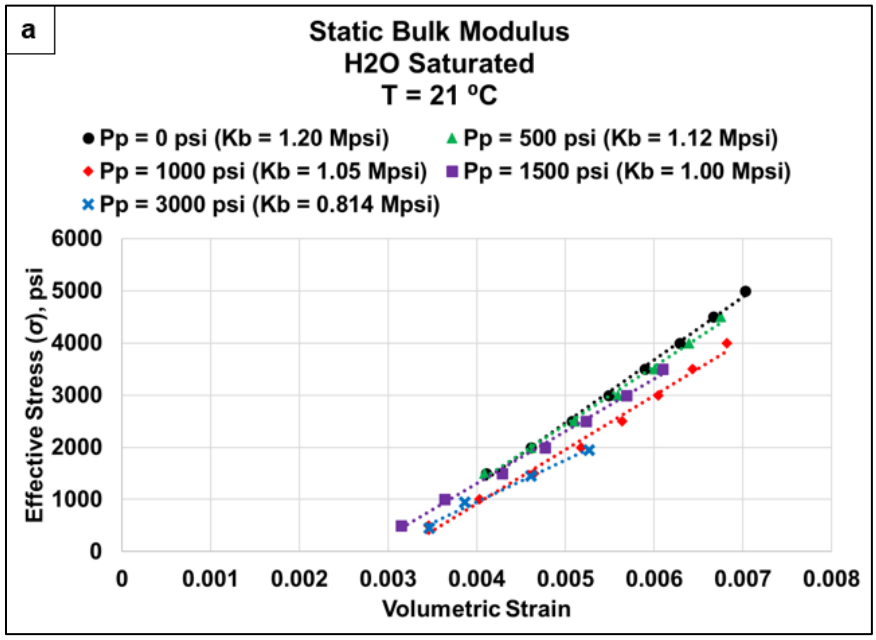

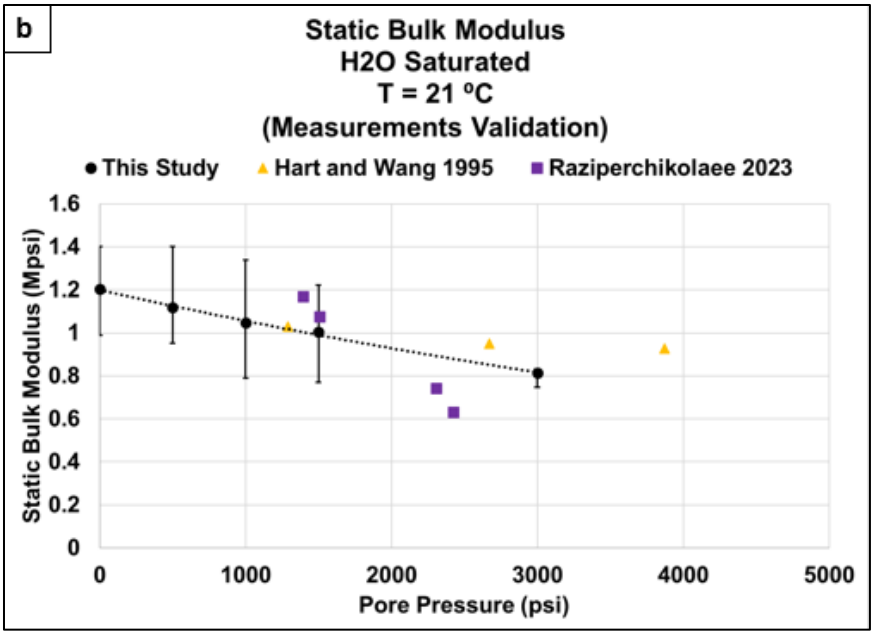

Figure 4: Validation and comparison of static bulk modulus measurements. (a) Bulk modulus estimation at P_p of 0, 500, 1,000, 1,500, and 3,000 psi for the H_2O-saturated sample at 21°C. (b) Validation and comparison between our measurements and previous studies.

Figures 5.a and 5.b show the slopes of σ versus ε_v at constant P_p for both H_2O-saturated and $scCO_2$-saturated samples at 80 °C. The slopes are nearly linear, however, to consider the K_b^{static} at low, middle, and high effective stresses (σ) portions, we selected three slope values per each P_p condition. The slopes from Figures 5.a and 5.b are utilized to estimate the K_b^{static} for all testing conditions in Figure 5.c. The error bars in Figure 5.c are from the slopes of low and high effective stress conditions.

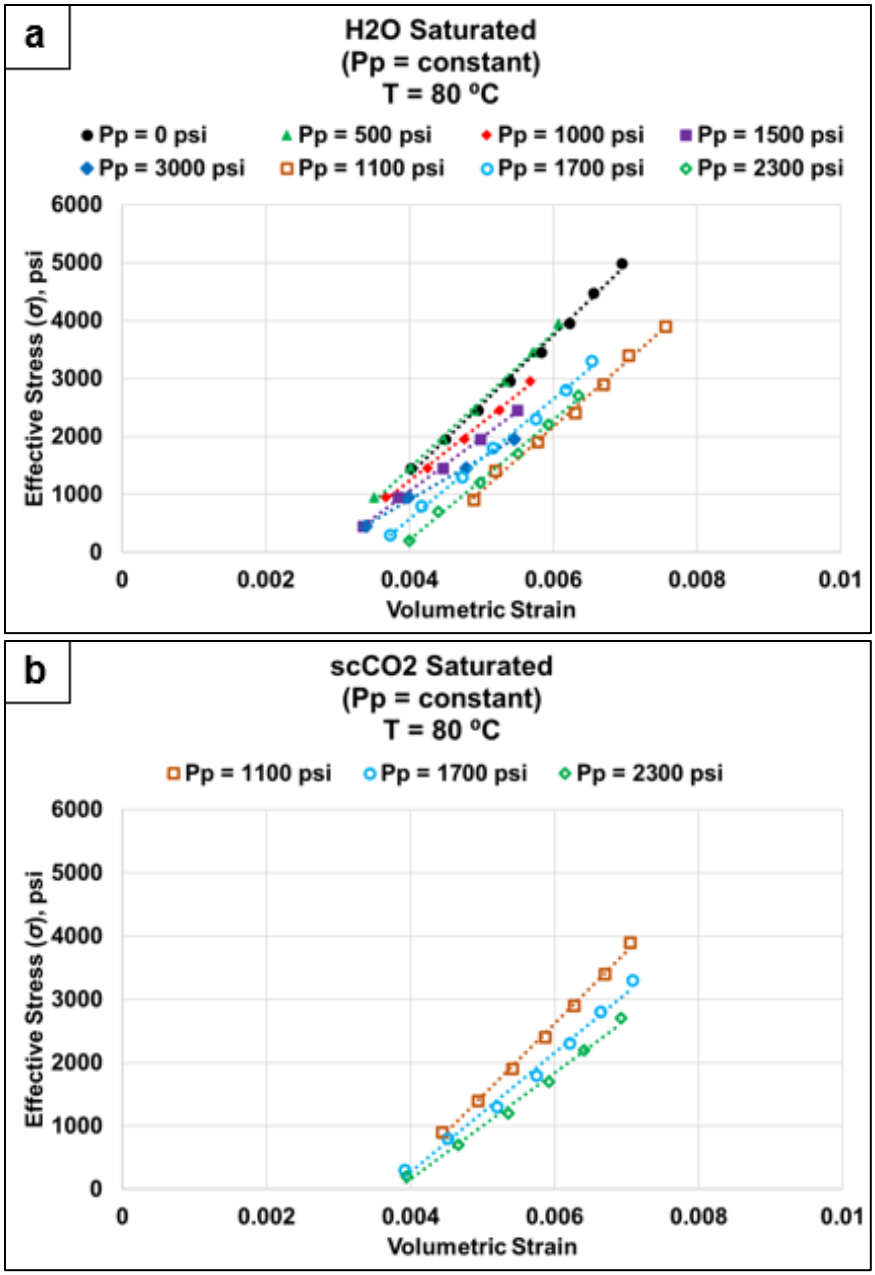
a
H2O Saturated
(Pp = constant)
T = 80 °C
Pp = 0 psi
Pp = 500 psi
Pp = 1000 psi
Pp = 1500 psi
Pp = 3000 psi
Pp = 1100 psi
Pp = 1700 psi
Pp = 2300 psi
Effective Stress (σ), psi
6000
5000
4000
3000
2000
1000
0
0
0.002
0.004
0.006
0.008
0.01
Volumetric Strain
b
scCO2 Saturated
(Pp = constant)
T = 80 °C
Pp = 1100 psi
Pp = 1700 psi
Pp = 2300 psi
Effective Stress (σ), psi
6000
5000
4000
3000
2000
1000
0
0
0.002
0.004
0.006
0.008
0.01
Volumetric Strain

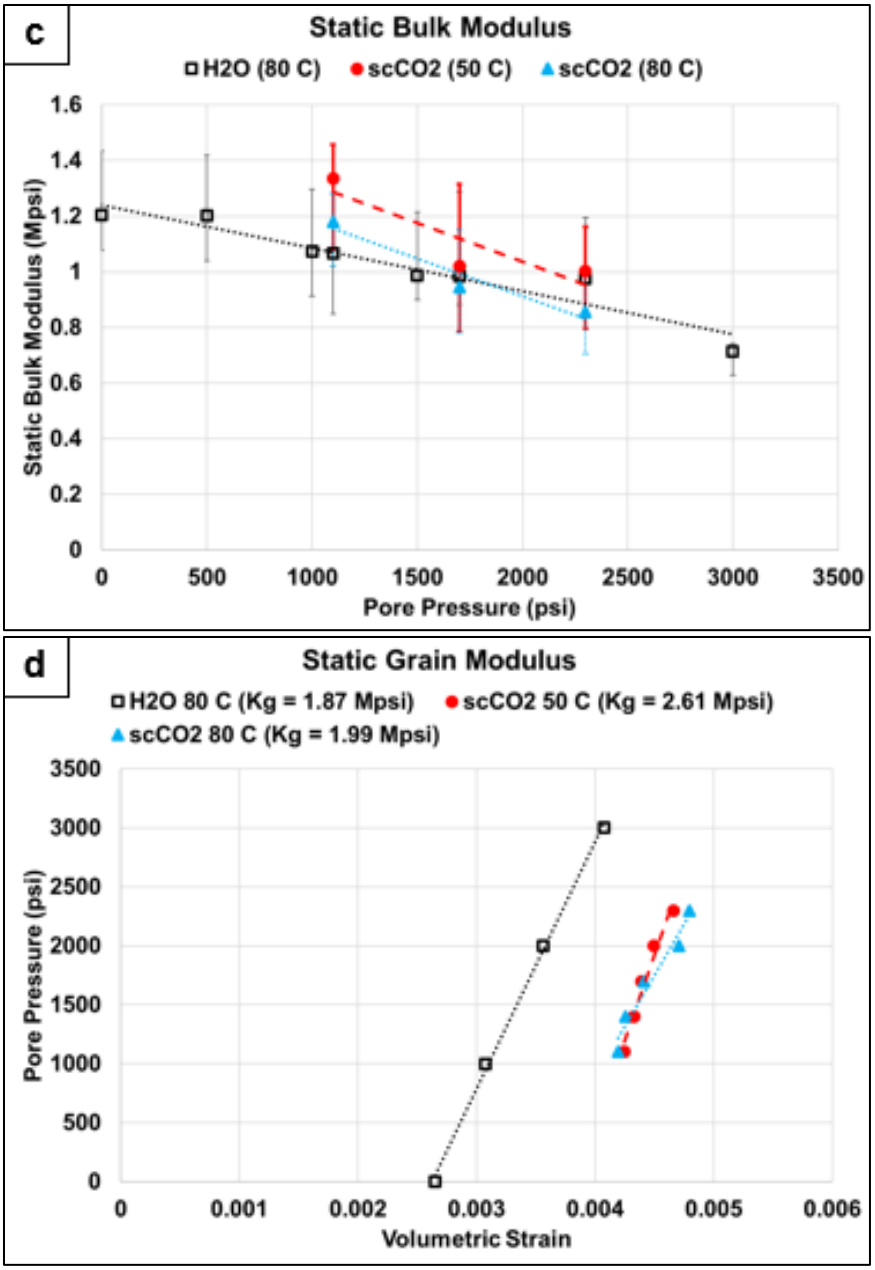

Figure 5: Static bulk modulus and Grain modulus measurements. (a) Bulk modulus estimation for H_2O-saturated sample at 80 °C and (b) Bulk modulus estimation for $scCO_2$-saturated sample at 80 °C. (c) Impact of pore pressure on bulk modulus. (d) Grain modulus for three test conditions. Black is for the H_2O-saturated sample at 80 °C, while red and blue represent the $scCO_2$-saturated sample at 50 °C and 80 °C, respectively.

Figure 5.c shows that K_b^{static} decreases for the H_2O-saturated sample from 1.2 to 0.71 Mpsi with increasing P_p, from 0 to 3,000 psi. The same trend was observed for the $scCO_2$-saturated sample, with K_b^{static} decreasing from 1.18 to 0.86 Mpsi with increasing P_p from

1,100 to 2,300 psi. The K_b^{static} of the $scCO_2$-saturated sample indicated a more significant decline with increasing P_p than the H_2O-saturated sample. In addition, the K_b^{static} value decreased by approximately 13% when the temperature was raised from 50 °C to 80 °C for the $scCO_2$ saturated sample. This might be related to increased $scCO_2$ compressibility resulting from decreased $scCO_2$ density with increasing temperature (Onyebuchi et al., 2018; Liao et al., 2023).

The grain modulus (K_g) was measured by estimating the slope of P_p against ε_v. Figure 5.d summarizes the slopes for the three test conditions: H_2O-saturated at 80 °C and $scCO_2$-saturated at 50 °C and 80 °C. The grain modulus value was 1.87 Mpsi for the H_2O-saturated sample at 80 °C, while for the $scCO_2$-saturated sample, K_g were 2.6 Mpsi at 50 °C and 1.9 Mpsi at 80 °C. The decrease in grain modulus with increasing temperature in the $scCO_2$-saturated case is likely due to the development of thermally-induced microcracks in the grains, as Asadollahpour et al. (2021) discussed.

Generally, the static Biot's coefficient (α_p^{static}), estimated from Equation (5), showed a positive correlation with P_p (Figure 6). For the H_2O-saturated sample at 80 °C, α_p^{static} increased from 0.35 to 0.61 with increasing P_p from 0 to 3,000 psi. For the $scCO_2$-saturated sample at 50 °C, α_p^{static} had the same trend but a higher range of 0.48-0.61 during the increase of P_p from 1,100 psi to 2,300 psi compared to a range of 0.42 to 0.47 for the H_2O-saturated sample at 80 °C for the same P_p values. The increase in α_p^{static} values at 50 °C for the $scCO_2$-saturated sample compared to the corresponding values at 80 °C for the H_2O-saturated sample was due to the increase of K_g from 1.87 to 2.61 Mpsi (Figure 5.d). When the temperature was raised to 80 °C for the $scCO_2$-saturated sample, α_p^{static} range dropped to 0.41-0.57, which is closer to the range of 0.42-0.47 for the H_2O-saturated sample at 80

°C. This drop is probably due to the development of thermally induced microcracks in the grains with increasing temperature, which yielded a lower K_g of 1.99 Mpsi compared to 2.61 Mpsi at 50 °C for the $scCO_2$-saturated sample (Figure 5.d). Based on the 80 °C results for both H_2O-saturated and $scCO_2$-saturated samples, it can be said that the saturation fluid type does not have a significant impact on the α_p^{static}. However, the decrease in temperature led to an increase in α_p^{static}, as shown in Figure 6.

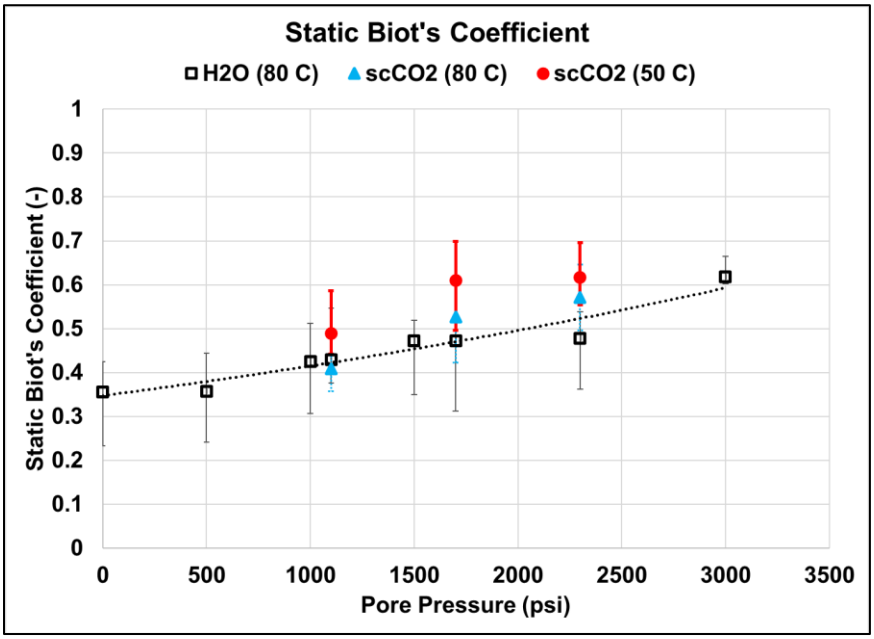

Figure 6: Summary of Static Biot's coefficient measurements.

2.3.2 Dynamic Measurements

The P-wave velocity (V_p) was measured during the testing process of both the bulk and grain moduli (Figure 3.a) to estimate the dynamic Biot's coefficient ($\alpha_p^{dynamic}$) from $\partial\sigma/\partial V_p$ and $\partial P_p/\partial V_p$ using Equation (6). The S-wave velocity (V_s) is the average of the two S-wave velocities (S1 and S2) recorded from the two orthogonal shear transducers (Figure 2.b). For the P-waveform, the compressional wave travel time is picked right before the first waveform, as shown in Figure 7, following the procedures explained by Xiwei et al. (2015).

The P-waveform for the $scCO_2$-saturated sample (Figure 7.b) showed an average amplitude attenuation of 12% and an average increase in the wavelength of 8% compared to the H_2O-saturated sample (Figure 7.a) for the testing steps 1 through 7, which agreed with the trend previously observed by Yun and Song (2022).

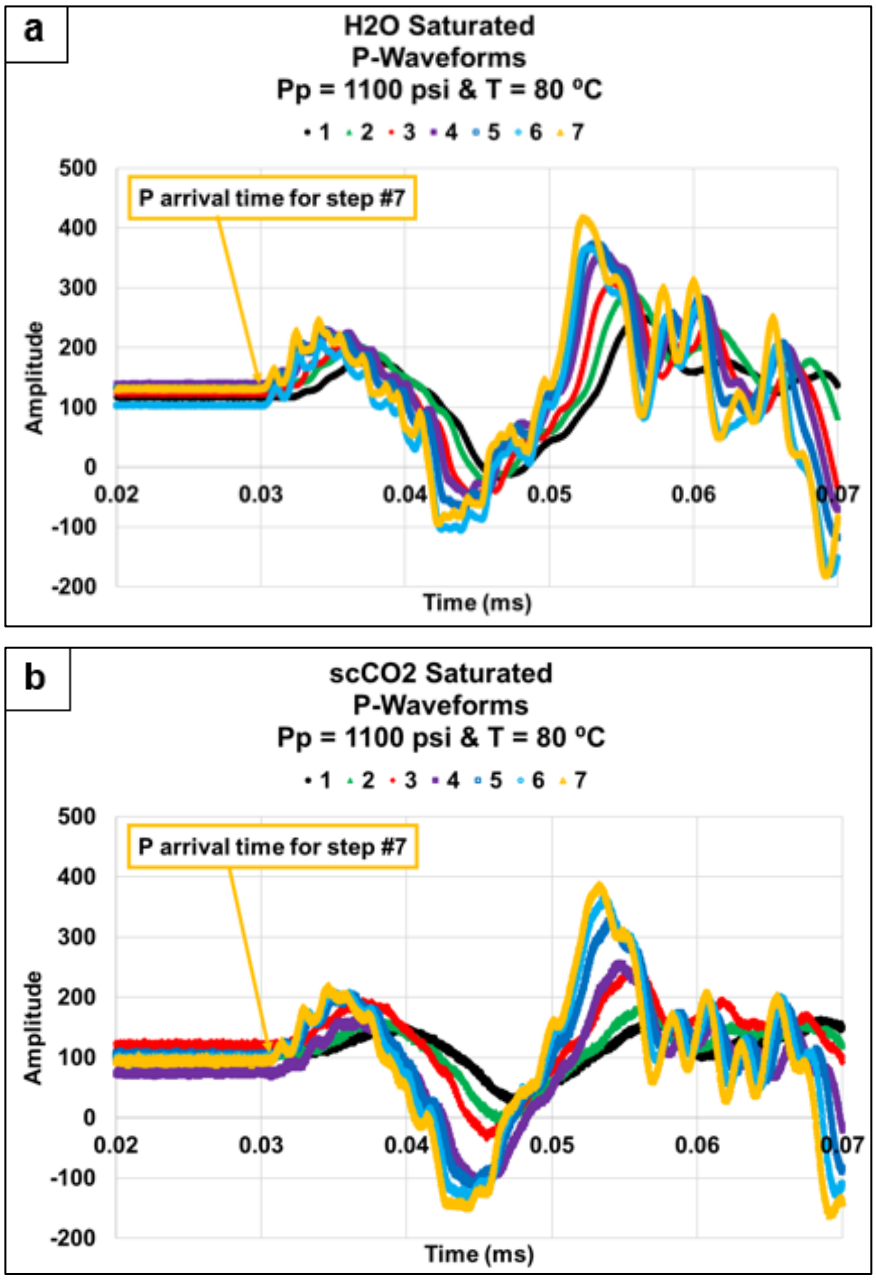

Figure 7: P-waveforms during steps 1 through 7 as described in Tables 3 and 6 at P_p of 1,100 psi and T of 80 °C: (a) H_2O-saturated and (b) $scCO_2$-saturated samples.

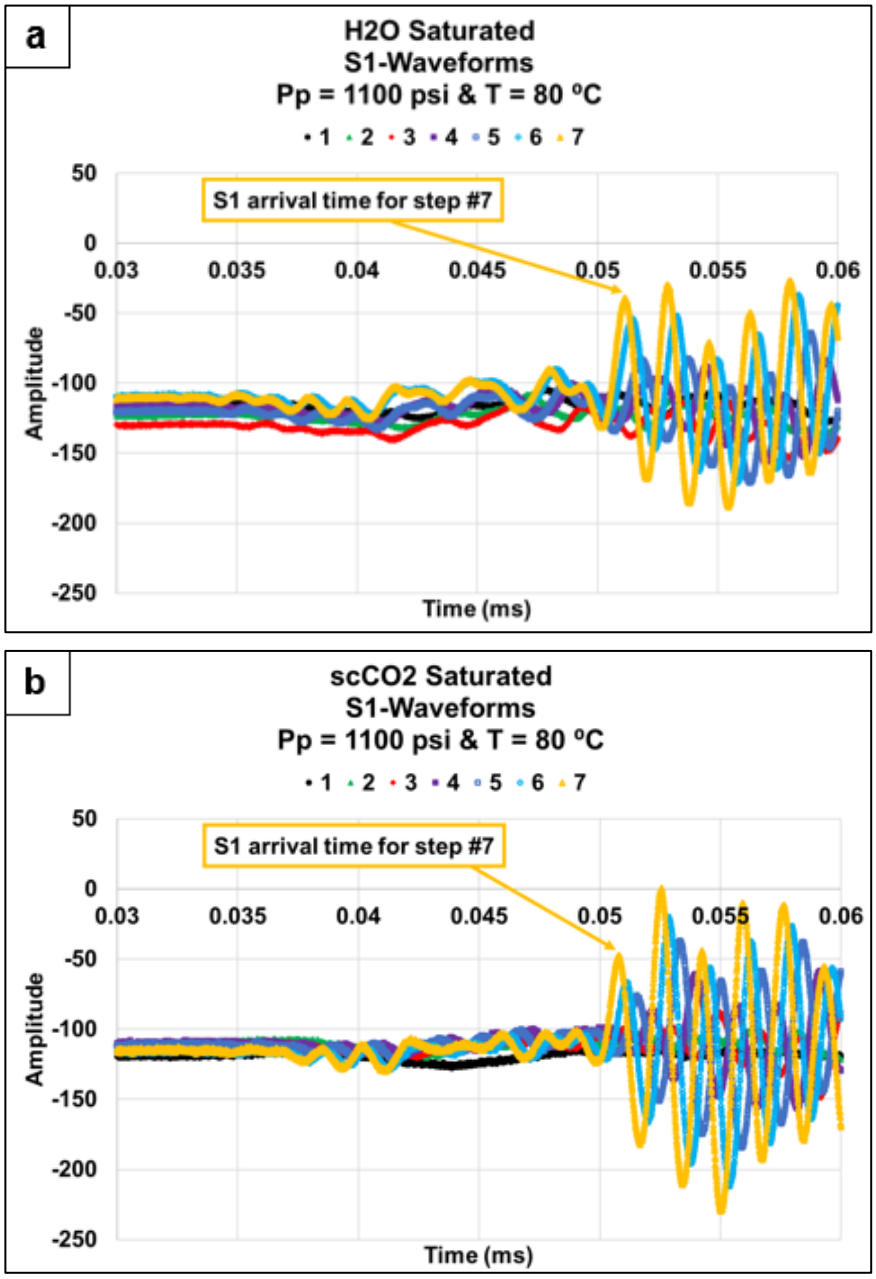

Figure 8: S1-waveforms during steps 1 through 7 as described in Tables 3 and 6 at P_p of 1,100 psi and T of 80 °C: (a) H_2O-saturated and (b) $scCO_2$-saturated samples.

For the S-waveforms, the shear wave arrival times are picked by locating the peak of the first waveform, which has high amplitude and short wavelength, as shown in Figures 8 and 9, following the standard method described by Crampin (1981). The S1 and S2 waveforms

for the $scCO_2$-saturated sample showed an average rise in the amplitude of 22% and an average drop in the wavelength of 5% for the seven testing steps (Tables 3 and 6) compared to that of the H_2O-saturated sample, as shown in Figures 8 and 9.

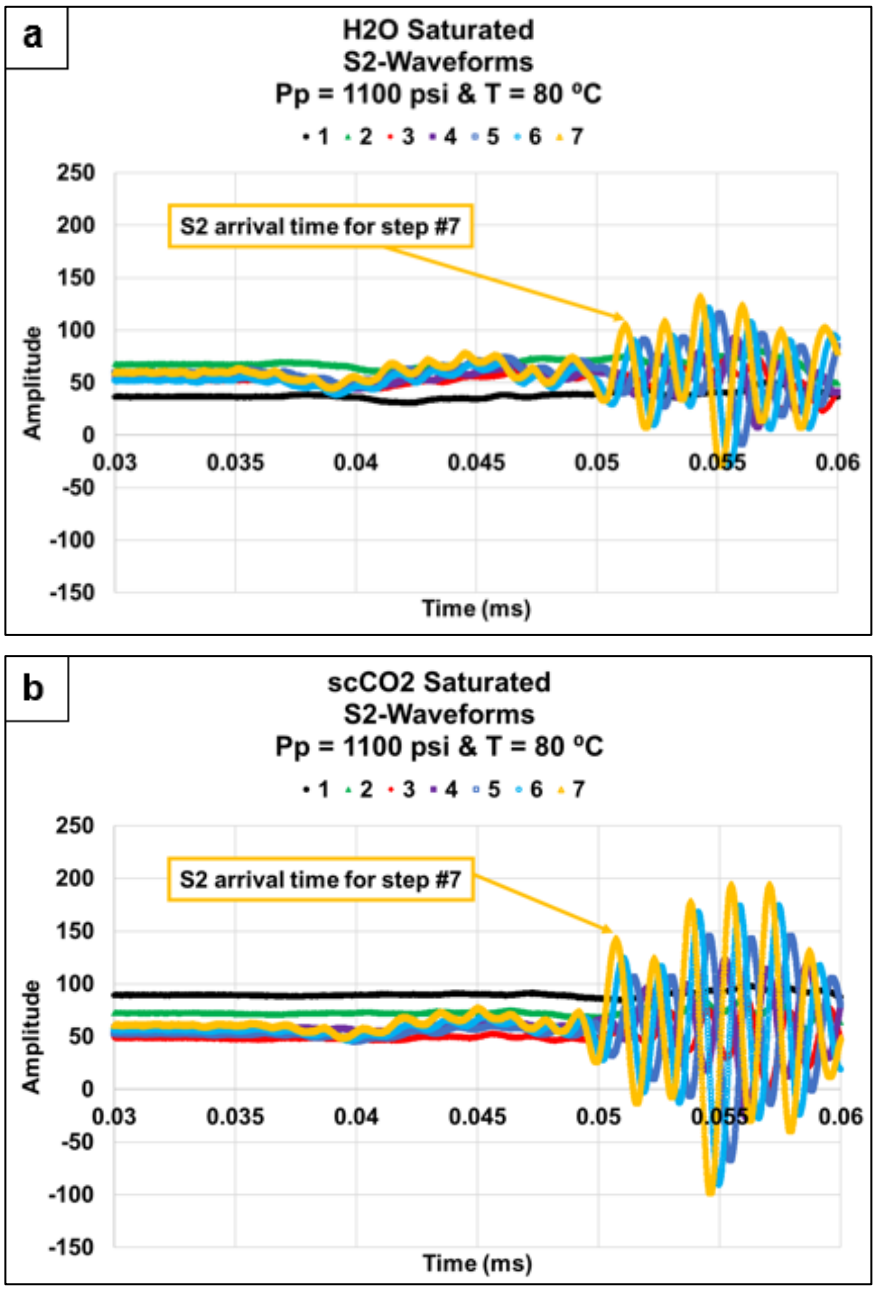

Figure 9: S2-waveforms during steps 1 through 7 as described in Tables 3 and 6 at P_p of 1,100 psi and T of 80 °C: (a) H_2O-saturated and (b) $scCO_2$-saturated samples.

Figure 10 shows V_p versus σ for both H_2O-saturated and $scCO_2$-saturated samples at pore

pressure values of 1,100, 1,700, and 2,300 psi and a temperature of 80 °C. For the H_2O-saturated sample, the gradual increase in σ from 200 to 3,900 psi yielded an increase in both the V_p from 3.1 to 3.75 Km/sec (Figure 10.a) and V_s from 2.1-2.45 Km/sec (Figure 10.b). The increase in P_p from 1,100 to 2,300 psi did not show a clear impact on the V_p, whereas a slight reduction was observed for V_s by approximately 5% when σ is below 2,000 psi. The overall trends of V_p and V_s for various P_p cases tend to converge at least within the range we tested.

However, for the $scCO_2$-saturated sample, there was a noticeable drop in both V_p and V_s with increasing P_p from 1,100 to 2,300 psi, especially when the effective stress (σ) was low. The V_s results indicated more dependence on P_p change. The V_p tends to converge above σ of 2,800 psi. Both the V_p and V_s generally showed wider ranges of 2.78 to 3.65 Km/sec (Figure 10.c) and 2.03 to 2.44 Km/sec (Figure 10.d), respectively, compared to the H_2O-saturated sample. Again, for each case, three V_p slopes were estimated, including an average slope for the entire dataset, the lowest slope at the high effective stress region, and the highest slope at the low effective stress region to estimate the error range for $\alpha_p^{dynamic}$ at each testing condition.

Figure 11 summarizes the slopes of V_p versus P_p measured during the K_g tests in Tables 2 and 5, at the previously mentioned temperature, pore pressure, and saturation conditions. For the H_2O-saturated sample, the increase in P_p from 0 to 3,000 psi at a constant σ of 950 psi yielded an increase in V_p from 3.58 to 3.69 Km/sec. For the $scCO_2$-saturated sample, the V_p increased during the increase of P_p from 1,100 to 2,300 psi at a constant σ of 850 psi with ranges of 3.31-3.38 Km/sec and 3.2-3.28 Km/sec at 50 °C and 80 °C, respectively. The V_p values for the $scCO_2$-saturated sample at 80 °C were 11% lower than the values for

the H_2O-saturated sample at the same temperature, which was probably due to the relatively higher density and lower compressibility of water compared to $scCO_2$. Although the effective stress conditions for the two samples were slightly different, we expect that this does not impact the grain modulus measurement, as discussed by Asadollahpour et al. (2021).

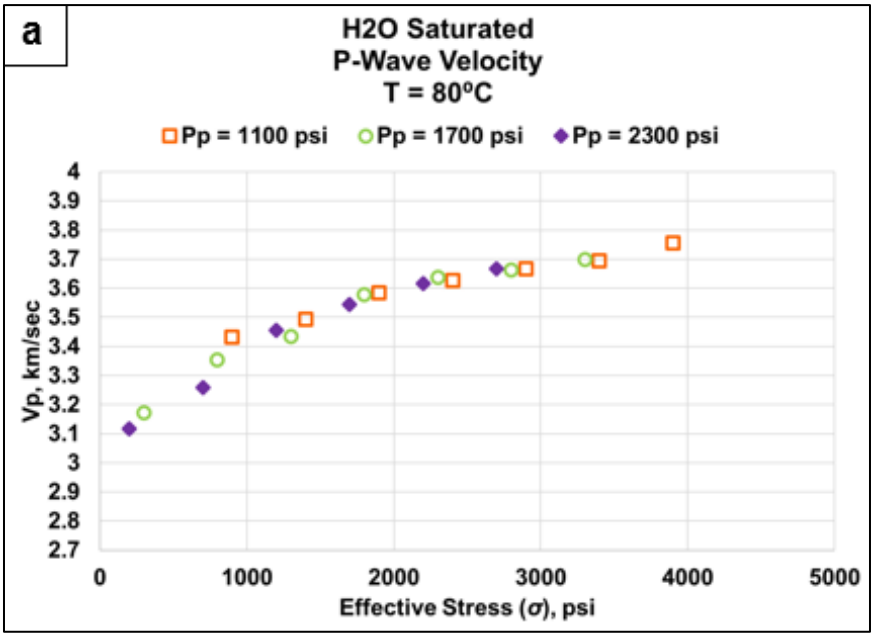

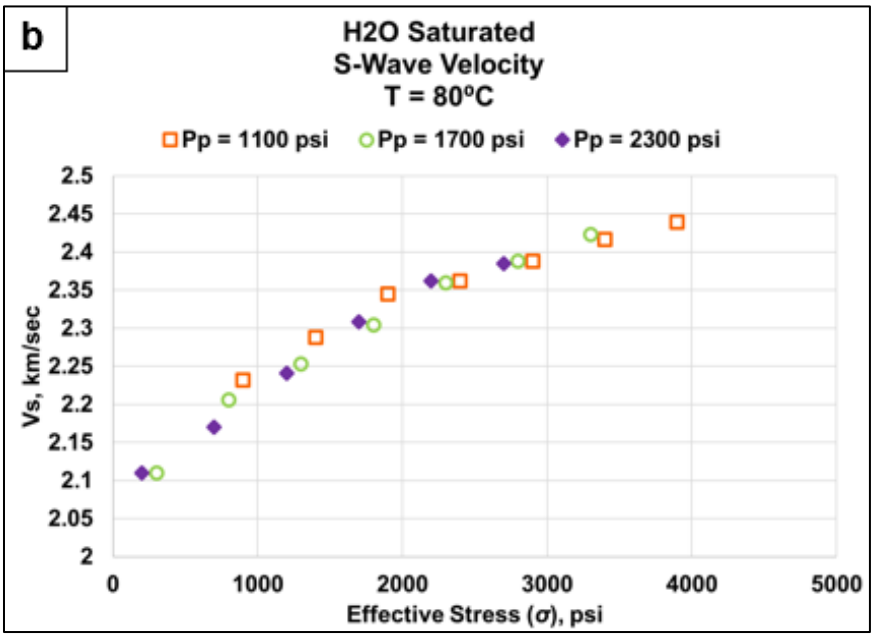

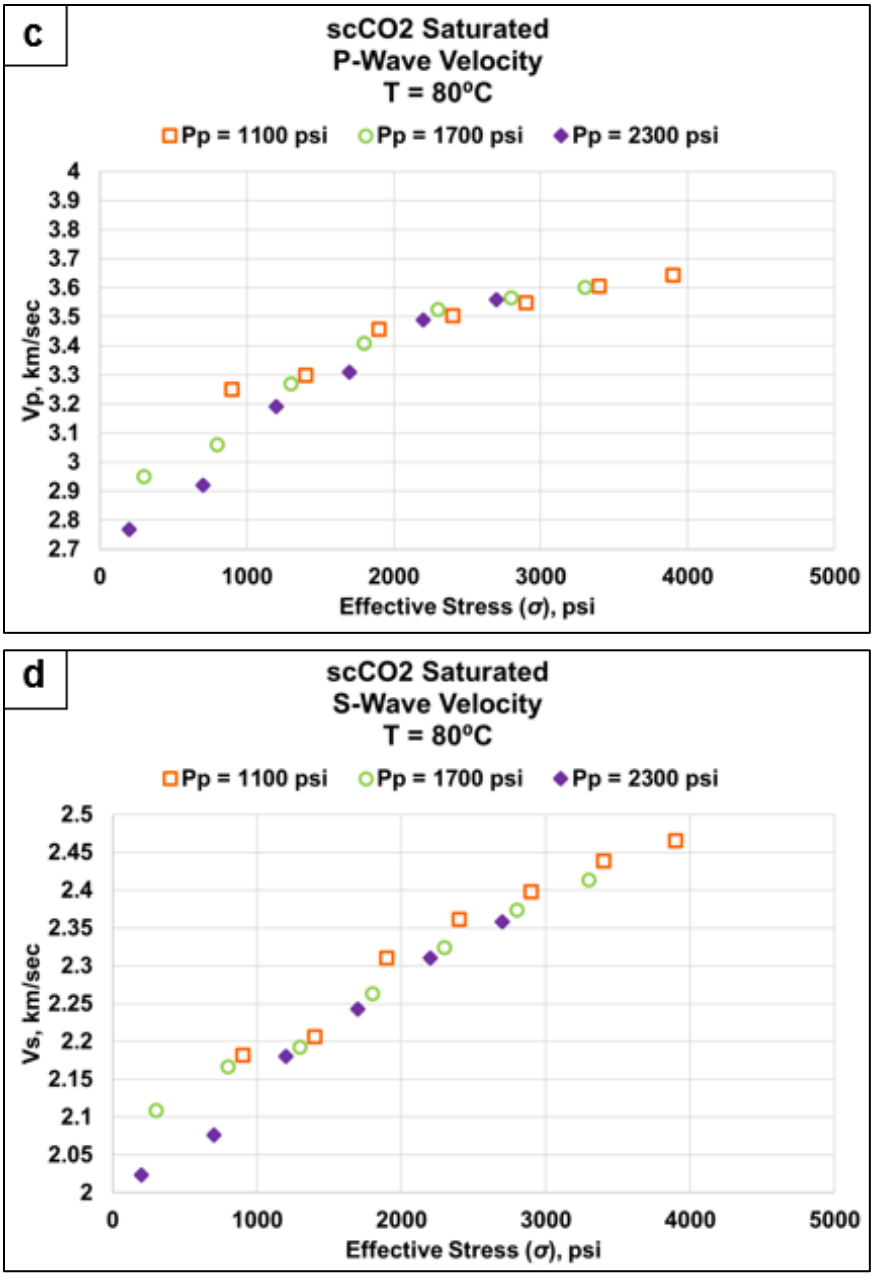

Figure 10: Dynamic poroelasticity measurements: (a) V_p versus σ for the H_2O-saturated sample. (b) V_s versus σ for the H_2O-saturated sample. (c) V_p versus σ for the $scCO_2$-saturated sample. (d) V_s versus σ for the $scCO_2$-saturated sample.

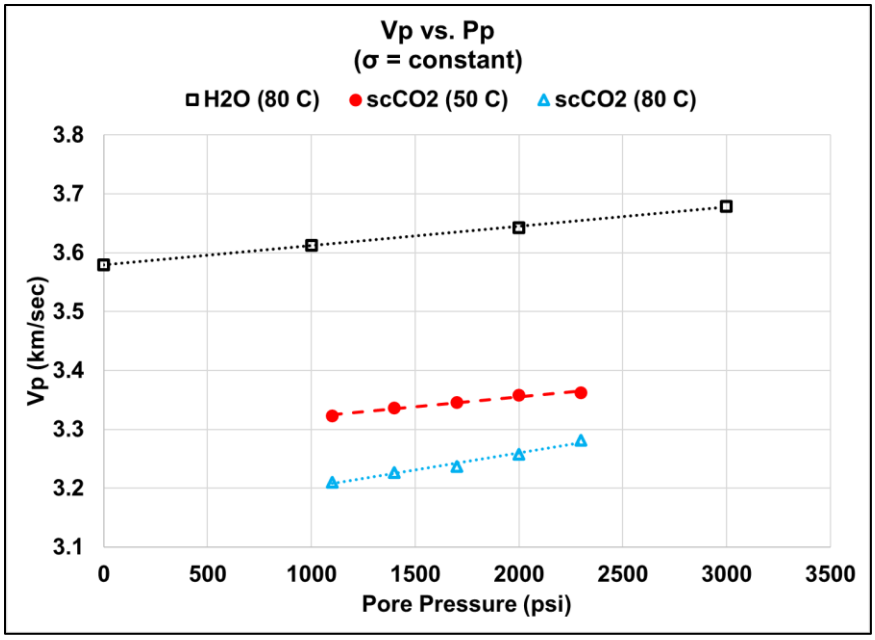

Figure 11: Dynamic poroelasticity measurements: V_p versus P_p for all cases.

Figure 12 summarizes the dynamic Biot's coefficient ($\alpha_p^{dynamic}$) calculations, which show similar trends as for the α_p^{static}. For the H_2O-saturated sample at 80 °C, the increase in P_p from 0 to 3,000 psi yielded a gradual increase in $\alpha_p^{dynamic}$ from 0.6 to 0.86, presumably due to the gradual decrease in the grain-to-grain contact area. For the $scCO_2$-saturated sample at 50 °C, $\alpha_p^{dynamic}$ increased from 0.73 to 0.89 during the gradual increase of P_p from 1,100 to 2,300 psi. These $\alpha_p^{dynamic}$ values were 8% higher than that of H_2O-saturated sample for the same P_p range (1,100-2,300 psi) and at 80 °C. When the temperature was raised from 50 °C to 80 °C for the $scCO_2$-saturated sample, $\alpha_p^{dynamic}$ dropped by approximately 10% to a range of 0.58-0.81 at the same P_p range of 1,100-2,300 psi.

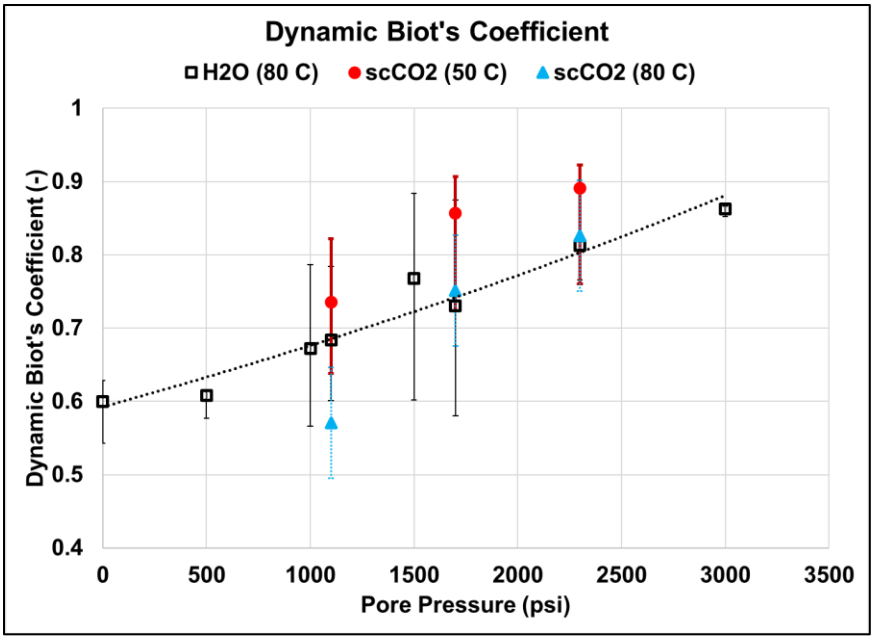

Figure 12: Impact of pore pressure on dynamic Biot's coefficient.

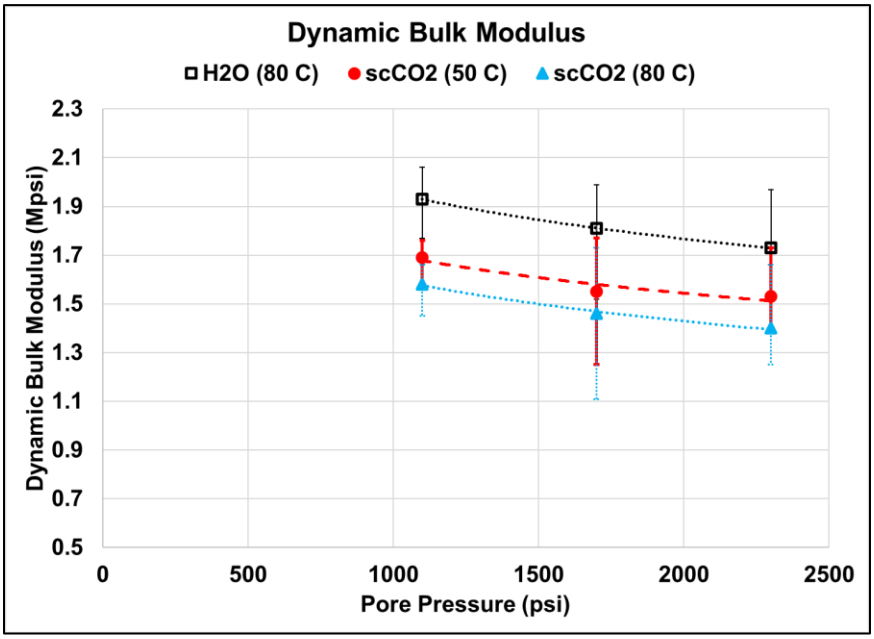

Figure 13: Impact of pore pressure on dynamic bulk modulus.

The V_s and V_p measurements were utilized to calculate the dynamic bulk modulus ($K_b^{dynamic}$) using Equations (7-11). Figure 13 shows that $K_b^{dynamic}$ generally increases with the decrease in P_p. The ranges of $K_b^{dynamic}$ for the scCO$_2$-saturated sample were 1.5-1.7 Mpsi (50 °C)

and 1.4-1.58 Mpsi (80 °C), while the range for the fully H_2O-saturated sample at 80 °C was 1.7-1.92 Mpsi. The increase in temperature from 50 °C to 80 °C lowered the dynamic bulk modulus by 20% for the $scCO_2$-saturated sample, potentially related to the increase in bulk compressibility resulting from the decrease in $scCO_2$ density, as described earlier.

2.3.3 Dynamic to Static Correction

The dynamic to static correction factor (F_{ds}) of the bulk modulus is the ratio between the static bulk modulus (K_b^{static}) and the dynamic bulk modulus ($K_b^{dynamic}$). Yale and Jamieson (1994) and Yale et al. (1995) found that the F_{ds} is directly correlated with bulk density and inversely correlated with porosity for carbonate and sandstone rocks. Figure 14 shows how the F_{ds} changes with P_p. For the H_2O-saturated sample at 80 °C, the F_{ds} was almost constant at 0.55 (ranging between 0.55-0.56) during the increase of P_p from 1,100 to 2,300 psi, which was within the F_{ds} range of 0.5-0.6 for Berea sandstone at 21 °C from Thompson et al. (1983). For the $scCO_2$-saturated sample at 50 °C, the F_{ds} decreased from 0.79 to 0.65 during the increase of P_p from 1,100 to 2,300 psi. When the temperature was raised back to 80 °C for the $scCO_2$-saturated sample, the F_{ds} values were approximately 7% lower compared to the 50 °C case for the same P_p conditions.

Overall, the dynamic Biot's coefficient measurements were generally higher than the static measurements by 40%, and they show a linear relationship for both the H_2O-saturated and $scCO_2$-saturated samples regardless of the temperature and pore pressure conditions, as shown in Figure 15. In general, the H_2O-saturated sample at 80 °C indicated the highest dynamic Biot's coefficient, and the $scCO_2$-saturated sample showed the lowest dynamic Biot's coefficient for a given static Biot's coefficient.

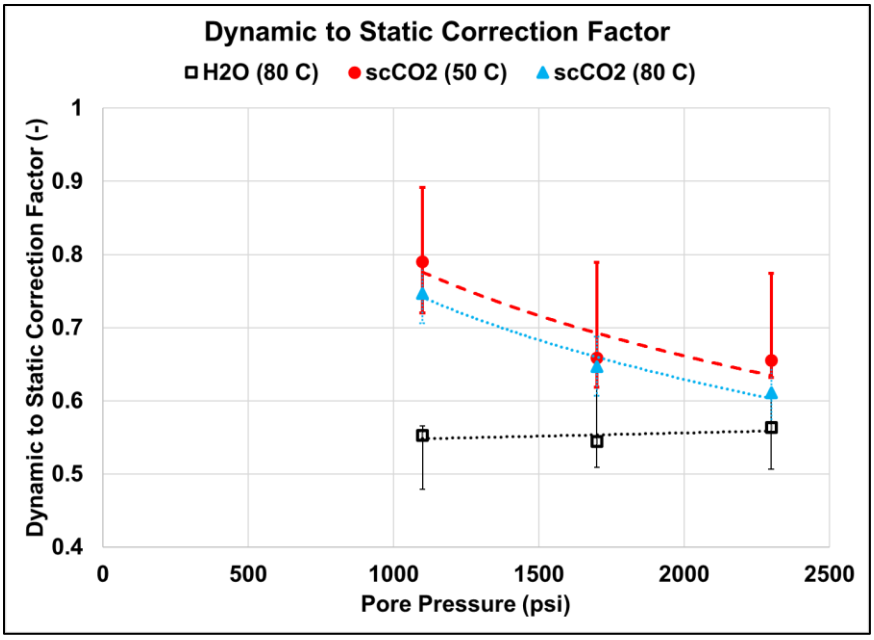

Figure 14: F_{ds} of bulk modulus versus pore pressure.

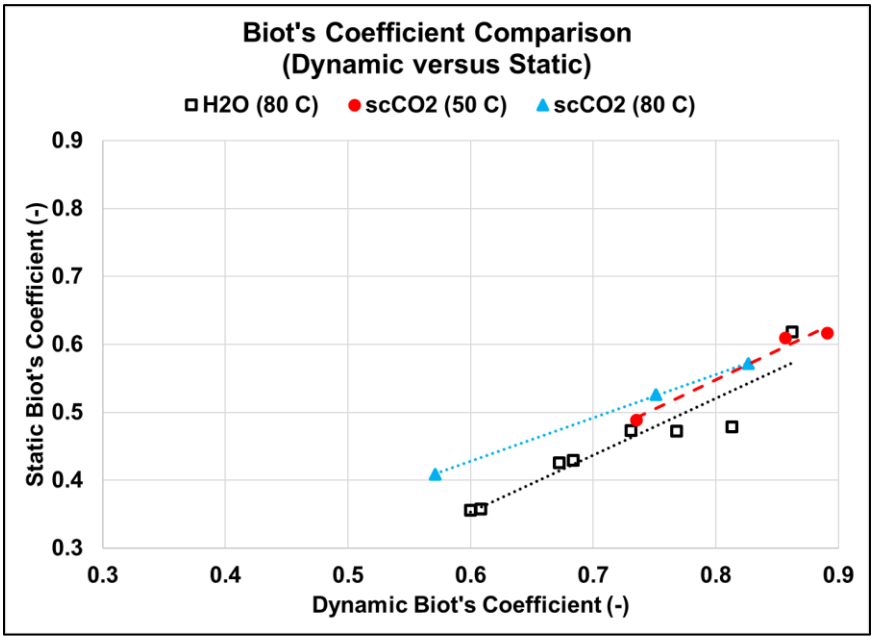

Figure 15: Static versus dynamic Biot's coefficient.

2.4 Discussion

2.4.1 Storage Capacity Evaluation

Economides et al. (2010) explained how the CO_2 storage capacity can be analytically evaluated from the material balance equation as,

$$P_{avg} = P_i + \frac{1}{c_t}\left(\frac{V_{CO2}B_g}{V_p}\right) \quad (15)$$

where P_{avg} is the average reservoir pressure in psi, P_i is the initial reservoir pressure in psi, c_t is the bulk compressibility in psi^{-1}, which is the inverse of K_b^{static}, and B_g is the gas formation volume factor for CO_2 (Jalil et al., 2012). The normalized storage term, V_{CO2}/V_p, represents the ratio between the total injected CO_2 volume (V_{CO2}) and the pore volume (V_p). The P_{avg} must not exceed the S_{hmin} to ensure the containment of the stored CO_2 within the injection horizon. In our analysis, we assumed the P_i to be 1,100 psi, the overburden stress to be 7,000 psi, and the S_{hmin} to be 4,000 psi, corresponding to an injection depth of 7,000 ft. Figure 16 summarizes the storage capacity evaluation for the two tested conditions, where the $scCO_2$-saturated sample at 80 °C showed a higher normalized storage of 0.68 compared to the same sample at 50 °C of 0.57, which might be related to the lower c_t at 80 °C (Abdelaal and Zeidouni, 2022; Neuyam et al., 2022). This suggests that the CO_2 storage in the same reservoir is more effective when the reservoir temperature drop is minimized.

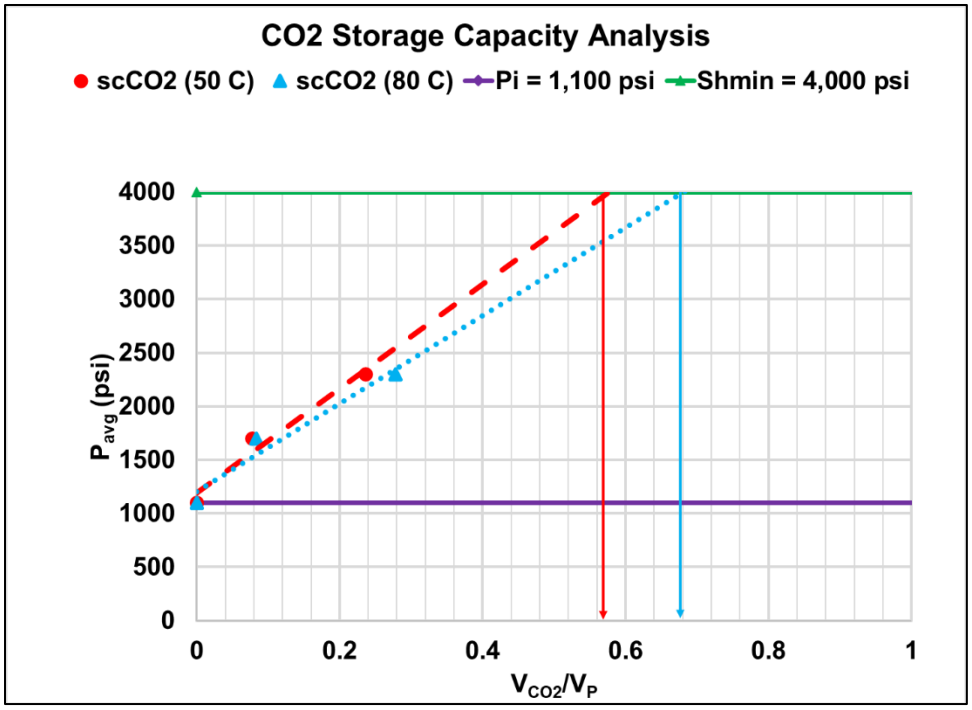

Figure 16: CO_2 storage capacity evaluation for the two tested conditions.

2.4.2 Stress Path Analysis

Another important issue to consider during CO_2 injection is fault stability, which could be affected by changes in the in-situ stress. Zoback (2007) introduced the stress path analysis, which evaluates fault stability during an increase in both pore pressure (P_p) and minimum horizontal stress (S_{hmin}) due to injection. The minimum horizontal stress (S_{hmin}) can be estimated from (Blanton and Olson, 1999):

$$S_{hmin} = \frac{\upsilon}{1-\upsilon} S_v + \frac{1-2\upsilon}{1-\upsilon} \alpha_p P_p + \frac{E}{1-\upsilon^2} \varepsilon_{tect} + \frac{E}{1-\upsilon} \alpha_T \Delta T \quad (16)$$

where, υ and E are the static Poisson's ratio (Figure 17.a) and the static Young's modulus (Figure 17.b), respectively. The υ is the ratio between radial to axial strains, and it was measured at three—low, middle, and high—effective stresses (σ) during the K_b^{static} measurement at each P_p condition (Figure 3.b). For $scCO_2$ saturated samples, the υ did not show a clear change with P_p, and its average values of 0.22 and 0.21 were utilized in S_{hmin}

calculations at 50 °C and 80 °C, respectively. For the H_2O saturated sample, the υ showed a positive correlation with P_p, and its estimated values from the trend line were utilized in S_{hmin} calculations. The E was derived from K_b^{static} by re-arranging the terms in Equation (11). The ΔT represents the difference between the reservoir temperature (i.e., 50 °C and 80 °C for this study) and the surface temperature (i.e., assumed to be 21 °C). For this exercise, the tectonic strain (ε_{tect}) was assumed to be -0.00015, which represents a Normal Faulting regime, and we utilized the thermal expansion coefficient (α_T) for Berea sandstone from Somerton et al. (1981) as 0.00001 $°C^{-1}$. The overburden stress (S_v) was assumed to be 7,000 psi.

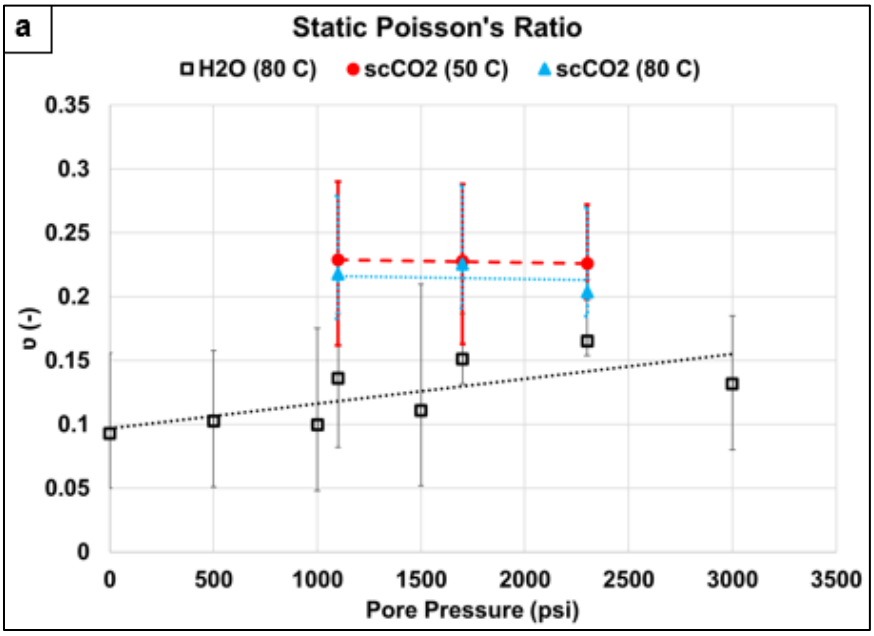

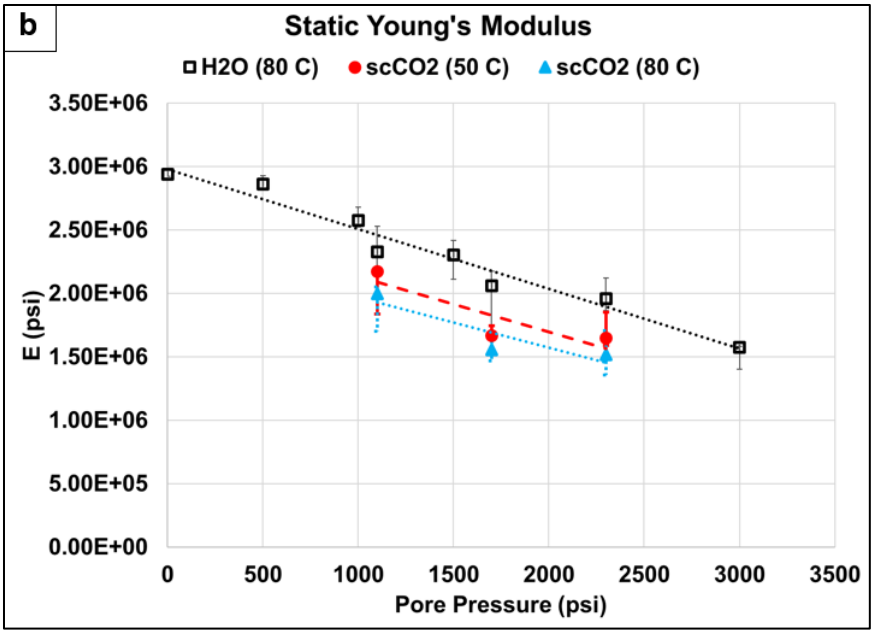

Figure 17: (a) Static Poisson's ratio. (b) Static Young's modulus.

The calculated S_{hmin} values were plotted against P_p for the three tested conditions (Figure 18) after calculating the slope, $\Delta S_{hmin}/\Delta P_p$, from Equation (17). The H_2O-saturated sample had the highest slope of 0.4501, while the $scCO_2$-saturated sample at 80 °C had a lower slope value of 0.2464 compared to the slope for the same sample at 50 °C of 0.3966. By assuming the sliding friction coefficient (μ) to be 0.6, the critical stress path term (A) is 0.67 based on (Zoback, 2007),

$$A = \frac{\Delta S_{hmin}}{\Delta P_p} = 1 - \frac{1}{\left(\sqrt{1+\mu^2}+\mu\right)^2} \quad (17)$$

Assuming a depleted reservoir at 7,000-ft depth with P_p and S_{hmin} of 1,100 psi and 4,000 psi, respectively, the slopes for three test conditions are plotted in Figure 18. The $scCO_2$-saturated sample at 80 °C, with the lowest slope, would reach the critical path first at approximately P_p of 3,500 psi. The 50 °C case would remain stable at P_p of 3,500 psi, suggesting that the near wellbore cooling effect could potentially enhance fault stability.

Thus, it is important to monitor reservoir integrity more carefully when the reservoir temperature recovers back to its initial condition.

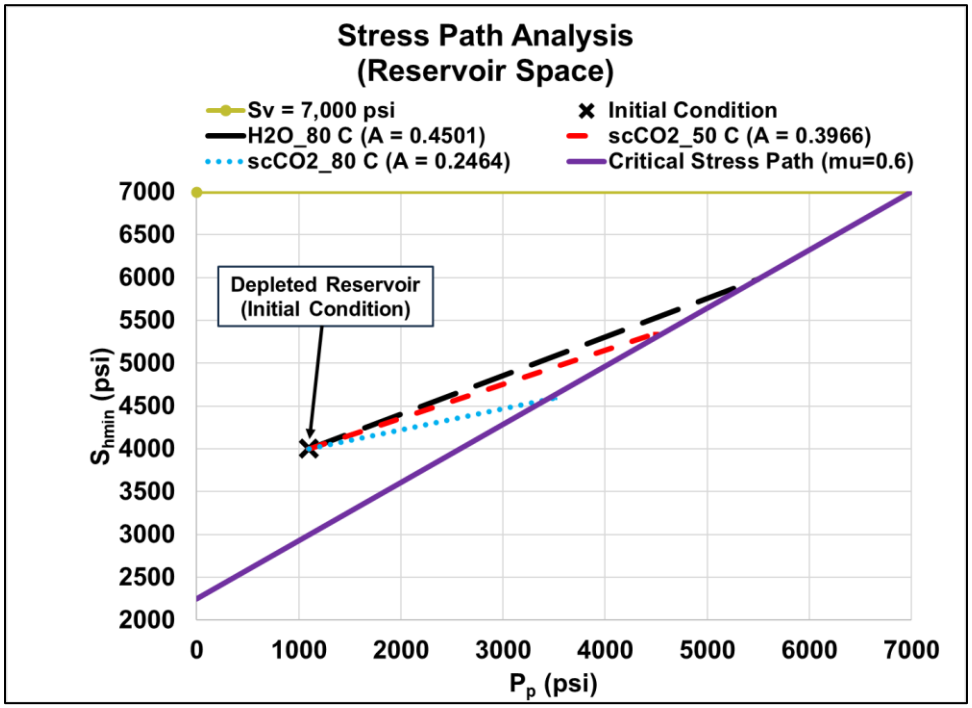

Figure 18: Stress path analysis for the three tested conditions.

2.5 Conclusions

In this study, we evaluated the impact of pore pressure on both the static and dynamic poroelastic properties, namely bulk modulus and Biot's coefficient, for Gray Berea sandstone due to the injection of CO_2 into a H_2O saturated sample. The measurements for the $scCO_2$-saturated sample were evaluated at 50 °C and 80 °C to mimic both the reservoir cooling during CO_2 injection in the vicinity of the wellbore and the reservoir temperature stabilization at 80 °C after long-term storage.

The experimental results showed that the pore pressure is positively correlated with Biot's coefficient, as the increase in pore pressure reduces the grain-to-grain contact area.

Temperature had a negative correlation with Biot's coefficient, possibly due to the thermal opening of microcracks, which lowers the grain modulus. The dynamic Biot's coefficient, estimated from the P-wave and S-wave measurements, was observed to be 40% higher than the corresponding static Biot's coefficient. The bulk modulus values for the $scCO_2$-saturated sample at 80 °C were lower than that of 50 °C, due to the increase in $scCO_2$ compressibility resulting from a decrease in $scCO_2$ density at higher temperatures.

The CO_2 storage capacity evaluation from the material balance equation showed that the $scCO_2$-saturated sample at 80 °C yielded higher capacity than the same sample at 50 °C, due to the reduction in bulk compressibility at a higher temperature. However, the stress path for the CO_2-saturated sample at 80 °C is expected to reach the critical stress path before the path of the 50 °C case. This suggests that the increase in reservoir temperature from 50 °C to 80 °C after long-term CO_2 storage reduces fault stability. The measurements and findings of this study can be utilized to assess reservoir storage capacity and reservoir integrity for geological CO_2 storage applications.

CHAPTER III

3 Integrating Experiments and Petrophysical Data to Predict Caney Shale Mechanical Properties with Unsupervised Machine Learning

Abstract

Caney shale is an emerging oil reservoir in southern Oklahoma. Understanding the impact of reservoir depletion and developing a reliable method to estimate its mechanical properties are critical for optimizing subsurface engineering applications. We utilized a triaxial cell to measure ultrasonic (P-wave and S-wave) velocities for ten downhole Caney shale samples extracted from a pilot well under various effective stresses to indirectly assess the impact of pore pressure change on dynamic Young's modulus and Poisson's ratio during oil production. To estimate dynamic-to-static correction factor (F_{ds})—ratio between static and dynamic Young's moduli—across the Caney shale interval in Oklahoma, we integrated triaxial test measurements and petrophysical data including well logs and X-ray fluorescence (XRF) using unsupervised machine learning. We employed a novel workflow that includes Principal Component Analysis (PCA) to reduce dataset dimensionality of well logs and XRF datasets—both separately and combined, creating three scenarios, then Inverse Distance Weighting (IDW) was applied later to derive F_{ds} profiles for these scenarios. Furthermore, K-means clustering was applied to each scenario

to predict depositional facies and a stiffness zonation profile was built using chemostratigraphic analysis of the terrigenous elements to validate the predicted F_{ds}. The findings revealed that the dynamic Young's modulus positively correlated with the effective stress for all ten samples. The predicted F_{ds} profile from each scenario using the PCA-IDW method was compared to the constant F_{ds} approach from our previous study by calculating the root mean square error (RMSE). The combined datasets scenario yielded the lowest RMSE value of 0.113, while the RMSE values for the well logs and XRF scenarios were 0.131 and 0.129, respectively. In addition, the predicted F_{ds} from the XRF scenario well-matched the stiffness zonation from the chemostratigraphic analysis that was built using the optimized K-means clustering of 9 clusters for that scenario. These methods and findings offer valuable insights into the effects of reservoir depletion on Caney shale's mechanical properties, refining lithological classification and improving F_{ds} profiling, potentially enhancing drilling and stimulation strategies in subsurface energy engineering.

3.1 Introduction

Rock mechanical properties, including Young's modulus and Poisson's ratio, are critical for estimating mechanical deformation in subsurface engineering applications. A thorough analysis of these properties is essential for optimizing drilling, well completion, and stimulation designs. Previous studies have extensively focused on how subsurface conditions, such as temperature, saturation, stress state, composition, bedding orientation, and depositional facies impact the mechanical properties of shale formations (Sone and

Zoback, 2013; Alqahtani et al., 2013; Rybacki et al., 2015; Dong et al., 2017; Tan et al., 2022; Guo et al., 2023; Xiong et al., 2023).

Guo et al. (2023) observed that Young's modulus values for Shizhu shale decreased by 37% when exposed to high temperatures (150 °C) compared to room temperature. Tan et al. (2022) showed that partially super-critical CO_2 saturated samples showed a 26% decrease in modulus compared to brine-saturated samples for Longmaxi shale. Alqahtani et al. (2013) demonstrated that the stiffness of Mancos and Eagle Ford shales was higher in cores with vertical bedding planes compared to those with horizontal bedding planes, consistent with the observations of Sone and Zoback (2013). Dong et al. (2017) showed that static Young's modulus values for several Horner River Group shale samples were strongly dependent on depositional facies, with authigenic quartz samples tended to have higher stiffness than bioturbated samples containing detrital carbonate or quartz set in a matrix of clay minerals.

However, direct measurement of rock mechanical properties is often challenging due to the difficulty of retrieving subsurface cores. As a result, indirect measurements, such as sonic logs, are used to interpret the mechanical properties in the subsurface. Previous studies have utilized ultrasonic velocities measurements of carbonate, sandstone, and shale formations to estimate dynamic mechanical properties, subsequently comparing these properties to static properties obtained from triaxial compression tests (Sone and Zoback, 2013; Słota-Valim, 2015; Yin and Xie, 2019).

For conventional reservoirs, Yale and Jamieson (1994) presented a direct correlation between porosity and the dynamic-to-static elastic moduli ratio for Chase and Council Grove carbonate sequences. Likewise, Yale et al. (1995) found a direct correlation with

porosity, but a negative correlation with quartz cementation and bulk density for Rottiegendes sandstone. Sone and Zoback (2013) demonstrated that both static and dynamic elastic moduli decrease monotonically with increasing clay and kerogen content in samples from several shale formations. Furthermore, Valim (2015) assessed the correction factor for Lower Paleozoic shale to infer static mechanical properties from seismic data. Yin and Xie (2019) showed that an increase in detrital anhydrite minerals in Paleogene formation enhanced both the compressional-to-shear velocity ratio and dynamic Young's modulus.

These studies highlighted how static mechanical properties can be derived from ultrasonic P-wave and S-wave velocities at the laboratory scale, or wellbore scale, from sonic logs assuming dynamic-to-static correction factor (F_{ds})—ratio between static-to-dynamic Young's moduli—remains constant. However, the impact of reservoir depletion and the development of realistic F_{ds} profiles for the emerging Caney shale reservoir have not been thoroughly explored. Thus, the objectives of this study are to experimentally evaluate the impact of effective stress on Caney shale mechanical properties and to estimate F_{ds} for the entire Caney shale interval of a pilot well in Oklahoma. The F_{ds} profiles were derived using a novel workflow that employs Principal Component Analysis (PCA) to reduce the high dimensionality of the petrophysical data, including conventional well logs and X-ray fluorescence (XRF) datasets, into a smaller number of optimum principal components. Then, the Inverse Distance Weighting (IDW) method was applied to the optimum components to predict F_{ds} at each depth, enabling the derivation of static Young's modulus (E_{stat}^{*}). The predicted F_{ds} profiles were verified by comparing them with stiffness zonation from chemostratigraphic analysis.

3.2 Materials and Methods

3.2.1 Caney Shale Data

Caney shale is an emerging reservoir located in south-central Oklahoma, which is still under evaluation for hydrocarbon production (Cardott, 2017; Radonjic et al., 2020; Awejori et al., 2021; Kolmer et al., 2021; Katende et al., 2022; Benge et al., 2023; Awejori et al., 2024.a; Awejori et al., 2024.b; Dje et al., 2024; Xiong et al., 2023, 2024). It is over-bounded by Springer shale and under-bounded by Sycamore limestone and Woodford shale (Wang et al., 2021). Caney shale is made of five main zones, which can be listed along the depth as Reservoir 1, Ductile 1, Reservoir 2, Ductile 2, and Reservoir 3, as illustrated in Figure 19 (Awejori et al., 2021; Benge et al., 2023). The following petrophysical data and downhole samples have been collected for Caney shale from a pilot well in south-central Oklahoma.

3.2.1.1 Conventional Well Logs

Figure 19 shows the conventional well logs along Caney shale, consisting of 1,110 observations with a vertical resolution of 0.5 ft. It includes gamma ray (GR), bulk density (RHOB), neutron porosity (PHIN), deep resistivity (RDEEP), wellbore caliper (CALI), photoelectric factor (PEF), compressional transit time (DTC), and shear transit time (DTS), all plotted against the true vertical depth (TVD).

3.2.1.2 X-Ray Fluorescence (XRF) Data

X-ray fluorescence (XRF) measurements were conducted on a downhole core for the entire Caney shale collected from the pilot well to determine the elemental composition in ppm at every 1.0-foot interval using a handheld Thermo Scientific Niton^{TM} XL 3t GOLDD device, with a sample time of 180 seconds. In this study, 16 elements were considered from the XRF measurements, including iron (Fe), aluminum (Al), silicon (Si),

sulfur (S), calcium (Ca), titanium (Ti), lead (Pb), vanadium (V), chromium (Cr), manganese (Mn), cobalt (Co), nickel (Ni), copper (Cu), zinc (Zn), zirconium (Zr), and potassium (K). Ni, Fe, S, and Zn indicate anoxic depositional conditions, while Cr and Mn indicate suboxic and oxic conditions, respectively. Figure 20 shows the terrigenous elements, which are indicative of grain type and lithology (Reese, 2013), such as quartz (Si), clay minerals (Al and K), zircon (Zr), and rutile (Ti). Additionally, Ca indicates carbonate layers.

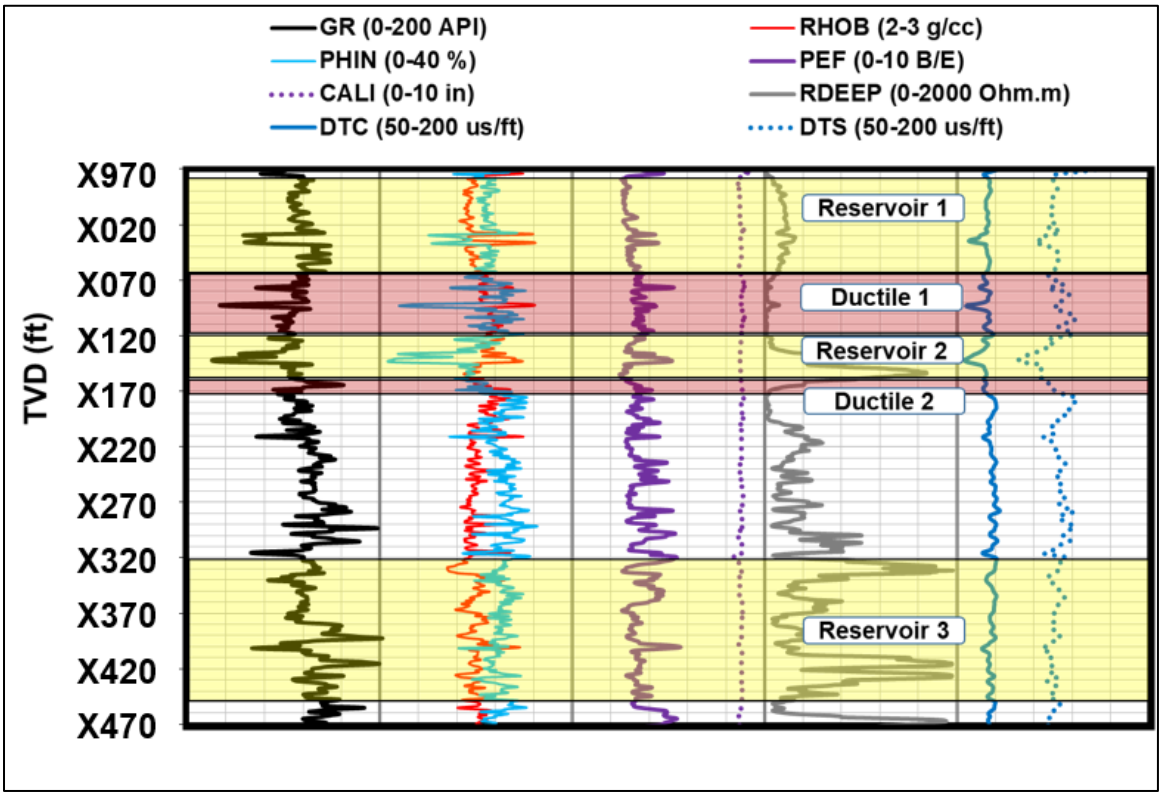

Figure 19: Conventional well logs through Caney shale for the pilot well.

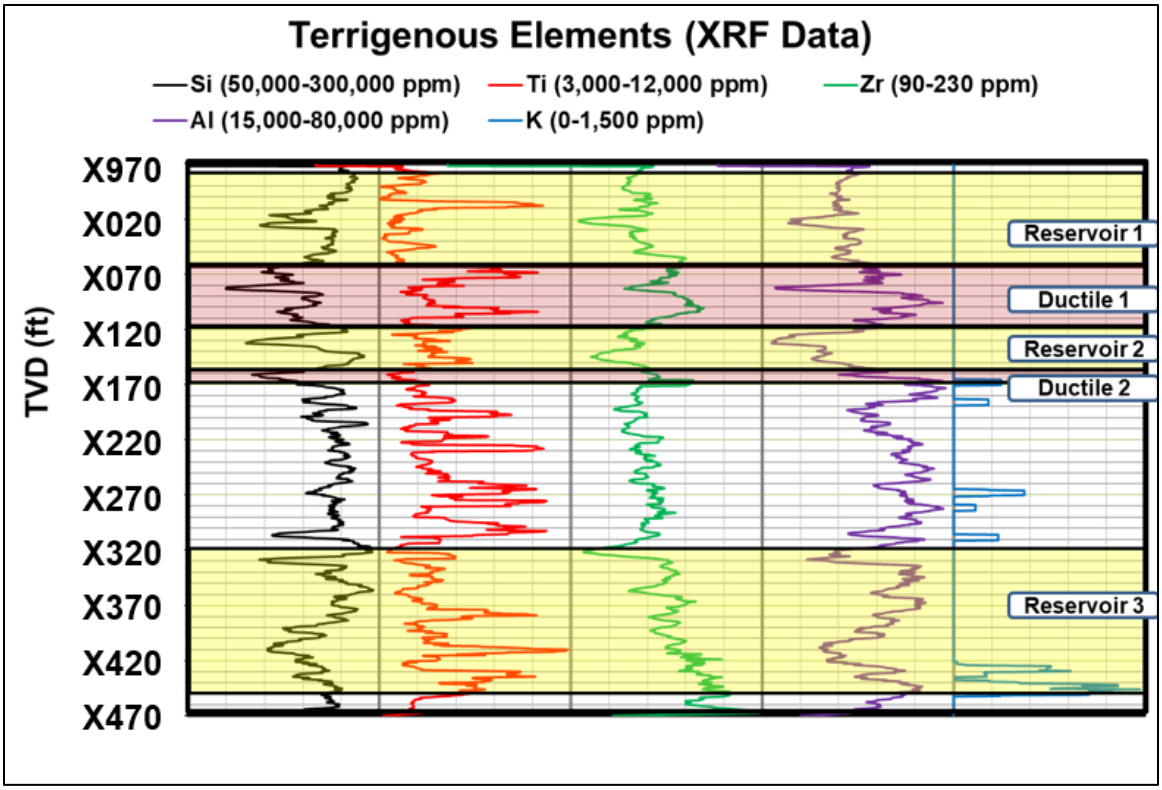

Figure 20: XRF terrigenous elements for Caney shale of the pilot well.

3.2.1.3 Depositional Facies Column

Reservoir 1 and 2 zones were characterized by relatively high resistivity as they are oil-bearing zones, and each is primarily composed of mudstone, bioturbated calcareous siltstone, packstone, grainstone, and rudstone carbonate facies, with occasional thin layers of dolomitic and banded facies (Radonjic et al., 2020; Benge et al., 2023). Ductile 1 and 2 zones had comparatively low resistivity, and each is composed of burrowed mudstone and bioturbated calcareous siltstone facies. The intermediate zone between Ductile 2 and Reservoir 3 had medium-to-high resistivity, and it was dominated by massive, bedded mudstone facies with scattered layers of dolomitic, burrowed mudstone, and bioturbated calcareous siltstone facies. Lastly, Reservoir 3 is composed of continuous burrowed mudstone, bioturbated calcareous siltstone facies, followed by packstone-grainstone

carbonate facies at the bottom.

3.2.1.4 Downhole Samples

A total of ten downhole cylindrical core samples were collected from a pilot well at various depths to represent the different layers of Caney shale. The dimensions and properties of each core are listed in Table 7. The computed tomography (CT) scans of these samples are summarized in Figure 21, which shows that microfractures were located along the bedding planes (indicated by green arrows). Also, pyrite was present in reservoir samples 1, 2, 4, and 5 (indicated by golden arrows), which had mineral content of > 65 wt%, including quartz, feldspar, pyrite, and apatite (Awejori et al., 2021; Benge et al., 2023). Subsequently, the ultrasonic P and S velocities were measured for each sample under various effective stress conditions to estimate dynamic mechanical properties, namely Young's modulus and Poisson's ratio, and to evaluate the impact of effective stress on these properties.

Table 7: Dimensions and properties of the collected Caney downhole samples.

Sample No.	Zone	TVD (ft)	Length (in)	Diameter (in)	Density (g/cc)
1	Reservoir #1	X030	3.14	1.47	2.47
2		X050	3.17	1.47	2.54
3	Ductile #1	X061	2.99	1.48	2.56
4	Reservoir #2	X145	3.18	1.47	2.51
5		X151	3.02	1.47	2.50
6	Ductile #2	X158	3.22	1.48	2.53
7	Intermediate Zone (between Ductile #2 and Reservoir #3)	X212	2.63	1.47	2.49
8		X259	2.99	1.47	2.45
9	Reservoir #3	X340	2.53	1.47	2.53
10		X450	2.99	1.48	2.61

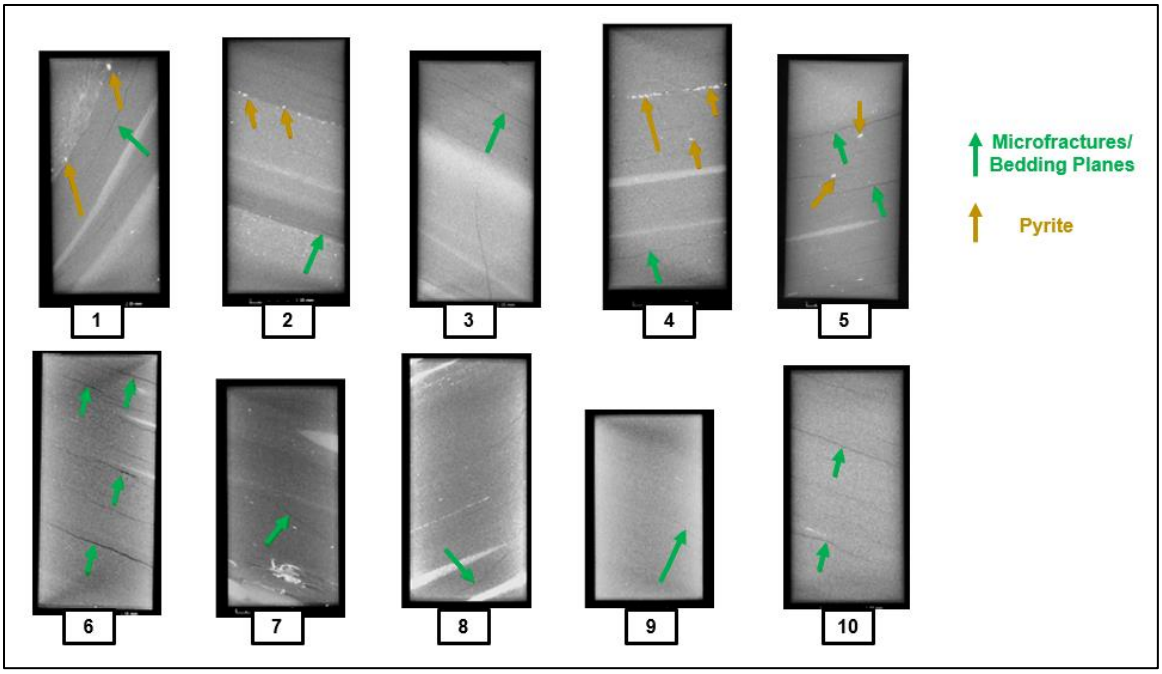

Figure 21: CT scan for the collected Caney downhole samples.

3.2.1.5 Triaxial Young's Modulus Measurements

The static Young's modulus (E_{stat}) measurements of five samples from Benge et al. (2021) were used to estimate the dynamic-to-static correction factor (F_{ds}). It should be noted that, in their study, the samples were cored perpendicular to the bedding planes, and Young's modulus was measured through triaxial testing at a confining pressure of 3,000 psi and a temperature of 194 °F. Table 8 summarizes the mineralogical composition and static Young's modulus measurements for the five samples. The dynamic Young's modulus (E_{dyn}) and F_{ds} were derived from conventional well logs based on the equations introduced by Nielsen and Kohlhaas (1979).

Table 8: Static (E_{stat}) and dynamic (E_{dyn}) Young's modulus and F_{ds} along with mineralogical composition from Benge et al. (2021) and Benge et al. (2023).

Zone	TVD (ft)	Mineralogical Composition			E_{stat} (Mpsi)	E_{dyn} (Mpsi)	F_{ds} (-)
		Quartz, Feldspar, Pyrite, Apatite (wt%)	Clay (wt%)	Carbonate (wt%)			
Reservoir #1	X998	68	18	14	5.02	5.31	0.95
Ductile #1	X100	51	39	10	4.00	5.17	0.77
Reservoir #2	X136	56	25	19	3.46	7.33	0.47
Ductile #2	X164	58	35	7	3.04	5.50	0.55
Reservoir #3	X433	61	13	26	4.40	5.32	0.83

3.2.2 Experimental Setup

The experimental setup of this study has four main components, as shown in Figure 22.a: a loading frame, a triaxial Hoek cell, an ISCO syringe pump, and a box controller (Kholy and Lee, 2023). The loading frame was utilized to apply vertical stress (σ_1) on the cylindrical sample, which was placed vertically inside the triaxial Hoek cell after wrapping it by a thermal duct tape to avoid any contamination from the confining fluid. The cell was connected to the ISCO syringe pump to control the confining pressure (σ_3) around the sample. The Hoek cell was equipped with one compressional wave transducer and two orthogonally positioned shear wave piezoelectric transducers (aligned N-S and E-W, with North direction corresponding to the front of the cell) at each end of the sample (Figure 22.b) to measure both the P-wave and S-wave velocities. The latter velocity represents the average of the two velocities from the two orthogonal shear transducers. Lastly, the box controller was utilized to control the cell temperature by heating the confining fluid. It also provided high voltage electrical pulses to energize the transmitting transducers and to capture both the transmitted and received waveforms.

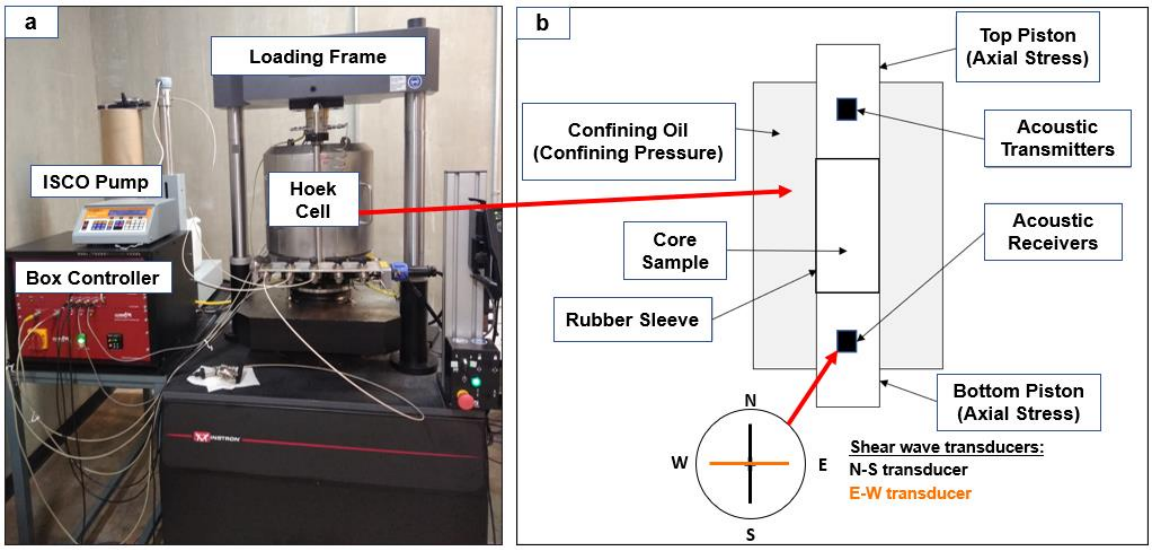

Figure 22: Acoustic measurement setup: (a) Main components and (b) Triaxial Hoek cell (after Kholy and Lee, 2023).

3.2.3 Testing Procedures

Ultrasonic acoustic velocities (P-wave and S-wave velocities) were measured under subsurface conditions for ten samples collected from various depths of the Caney shale formation (Table 7). The downhole effective stress conditions for the base case were determined based on the reported pore pressure gradient of 0.5-0.57 psi/ft, (Mayibeki, 2021). Although the downhole hole temperature was approximately 110 °C (240 °F), reported geothermal gradient of 21 °C/Km (Cheung 1978), two temperatures—room temperature (70 °F) and the maximum temperature (204 °F)—were tested due to equipment limitations. Test results at these temperatures were extrapolated to account for the actual reservoir temperature of 110 °C (240 °F). The increase in temperature resulted in a decrease in both P-wave and S-wave velocities by 0.00241 Km/sec/°C and 0.00156 Km/sec/°C, respectively. Three effective stresses were tested, including the actual downhole stress conditions (base case: σ_1 = 7000 psi & σ_3 = 3000 psi), to indirectly assess the impact of

pore pressure. Table 9 summarizes the testing conditions applied during the ultrasonic acoustic wave measurements.

Table 9: Testing conditions and measurements for the Caney samples.

Temperature (°C) (°F)	σ_1 (psi)	σ_3 (psi)	Measurements
21 & 95 (70 & 204)	5,000	1,000	P-wave and S-wave velocities (Dry Testing)
	7,000 (Base)	3,000 (Base)	
	9,000	5,000	

The Caney shale samples exhibit very low permeability at the nano-Darcy scale, which makes it impossible to fully saturate them. Consequently, the measurements were conducted on dry core samples. The impact of saturation on acoustic wave measurements was indirectly assessed using dry and fully saturated Gray Berea sandstone samples. Gray Berea sandstone was selected for this assessment due to its close clay content of 13 wt% and quartz content of 87 wt% (Shehata, 2016) to the reservoir layers of Caney shale (~15 wt% clay and ~70 wt% quartz) (Radonjic et al., 2020; Benge et al., 2021; Katende et al., 2021). The fully deionized (DI) water-saturated Gray Berea sandstone had an increase in P-wave velocity by 0.048 Km/sec and a decrease in S-wave velocity by 0.168 Km/sec compared to the dry sample at a temperature of 204 °F (Figure 23). These findings were later used to adjust the measurements for the Caney samples accordingly.

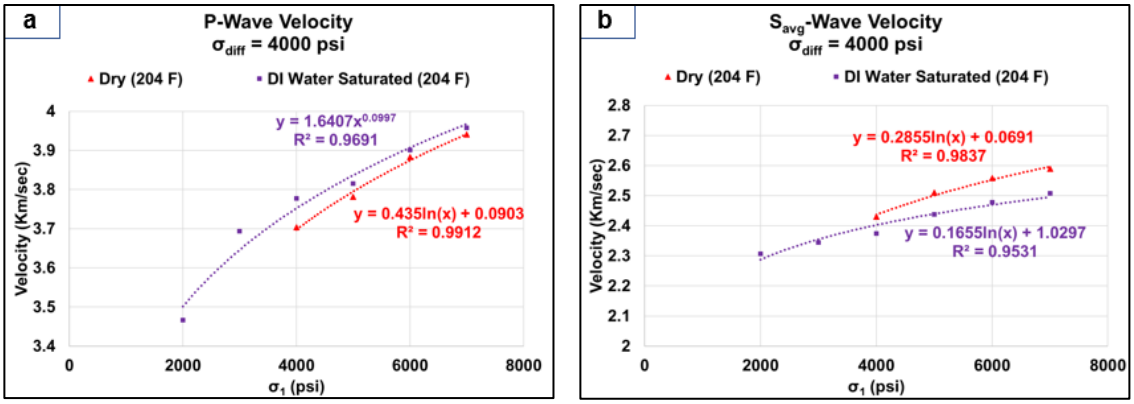

Figure 23: Impact of saturation on ultrasonic velocities for Gray Berea sandstone. (a) P-wave velocity. (b) S-wave velocity.

The dynamic Young's modulus (E_{dyn}) and Poisson's ratio (υ_{dyn}) were derived from the ultrasonic acoustic measurements (Nielsen and Kohlhaas, 1979) using Equations 7, 8, 9, and 10.

3.2.4 Unsupervised Machine Learning Models

3.2.4.1 Principal Component Analysis (PCA) and Inverse Distance Weighting (IDW) Workflow

Principal Component Analysis (PCA) is an unsupervised learning technique that reduces a dataset with multiple components or variables (i.e., high dimensionality) to a new dataset with fewer components, enabling better visualization and improving the computational speed of subsequent calculations (Bishop, 2006). In this study, PCA was applied to reduce the number of original components to an optimal number for three scenarios: (1) the conventional well log dataset, (2) the XRF dataset, and (3) the combined well log and XRF dataset, speeding up the Inverse Distance Weighting (IDW) calculations.

The optimal number of components should capture most of the data variability and can be estimated from the scree plot. In such a plot, the cumulative explained variance (ranging from 0 for the lowest accuracy to 1 for the highest) is plotted against the number of

principal components. The optimal number corresponds to a subjective cut-off value set for the cumulative explained variance based on the application's requirements (Bishop, 2006). In this study, the cut-off cumulative explained variance was set at 0.7. Afterward, IDW was applied to the transformed dataset to predict (F_{ds}) for the *n* observations based on the five known F_{ds} values from Benge et al. (2021). Details on PCA and IDW calculations are provided in Appendix A.

3.2.4.2 K-Means Clustering

K-means clustering, an unsupervised machine learning technique, has been utilized to identify the depths at which depositional facies change along the Caney shale interval for the same three scenarios. This was done to create a qualitative profile of stiffness changes, which can later be used to validate the predicted static Young's modulus. Details on the method and optimization of K-means clustering for each scenario are provided in Appendix A.

3.3 Results

3.3.1 Impact of effective stress on the dynamic mechanical properties

3.3.1.1 Mechanical Properties from Ultrasonic Acoustic Wave Measurements

The ultrasonic acoustic wave measurements were utilized to estimate the dynamic mechanical properties of Young's modulus ($E_{dyn}{}^{av}$) and Poisson's ratio ($\upsilon_{dyn}{}^{av}$) for the base case (σ_1 = 7000 psi and σ_3 = 3000 psi) using Equations (7)-(10). These measurements were then compared to the derived mechanical properties from the well logs (E_{dyn} and υ_{dyn}). Analysis of the measurements from the dry samples indicated a higher Young's modulus and lower Poisson's ratio than those estimated from the well logs, as illustrated in Figure 24.a.

By incorporating the saturation and the temperature effects, as described earlier, the E_{dyn}^{av} and υ_{dyn}^{av} shifted closer to the properties derived from the well log data, significantly improving the match, as shown in Figure 24.b. Table 10 summarizes the derived dynamic mechanical properties from the acoustic measurements before and after incorporating the effects of saturation and temperature.

3.3.1.2 Effective Stress Impact Evaluation

Figure 25.a shows that the estimated dynamic Young's modulus (E_{dyn}^{av}) increases with increasing effective stress for all samples, presumably due to the closure of microcracks. The Poisson's ratio has no clear correlation with the effective stress (Figure 25.b), consistent with the findings discussed by McPhee et al. (2015). For samples 4, 6, 7, 8, and 9, Poisson's ratio increases with the effective stress, while the opposite trend is observed for sample 3. For samples 1, 2, 5, and 10, Poisson's ratio does not show a clear trend with increasing effective stress. Table 11 summarizes the slopes between the effective stress and each of the dynamic Young's modulus and Poisson's ratio.

Table 10: Summary of derived mechanical properties from the acoustic measurements with adjustments for temperature and saturation.

Sample #	Zone	TVD (ft)	Before Correction		After Correction	
			E_{dyn}^{av} (Mpsi)	υ_{dyn}^{av}	E_{dyn}^{av} (Mpsi)	υ_{dyn}^{av}
1	Reservoir #1	X030	5.86	0.14	5.38	0.22
2		X050	5.59	0.14	5.13	0.23
3	Ductile #1	X061	5.87	0.17	5.36	0.24
4	Reservoir #2	X145	6.65	0.05	6.34	0.15
5		X151	6.16	0.10	5.78	0.19
6	Ductile #2	X158	6.14	0.17	5.59	0.24
7	Intermediate Zone	X212	5.62	0.14	5.15	0.23
8		X259	5.02	0.12	4.61	0.21
9	Reservoir #3	X340	5.82	0.13	5.34	0.22
10		X450	6.80	0.09	5.77	0.26

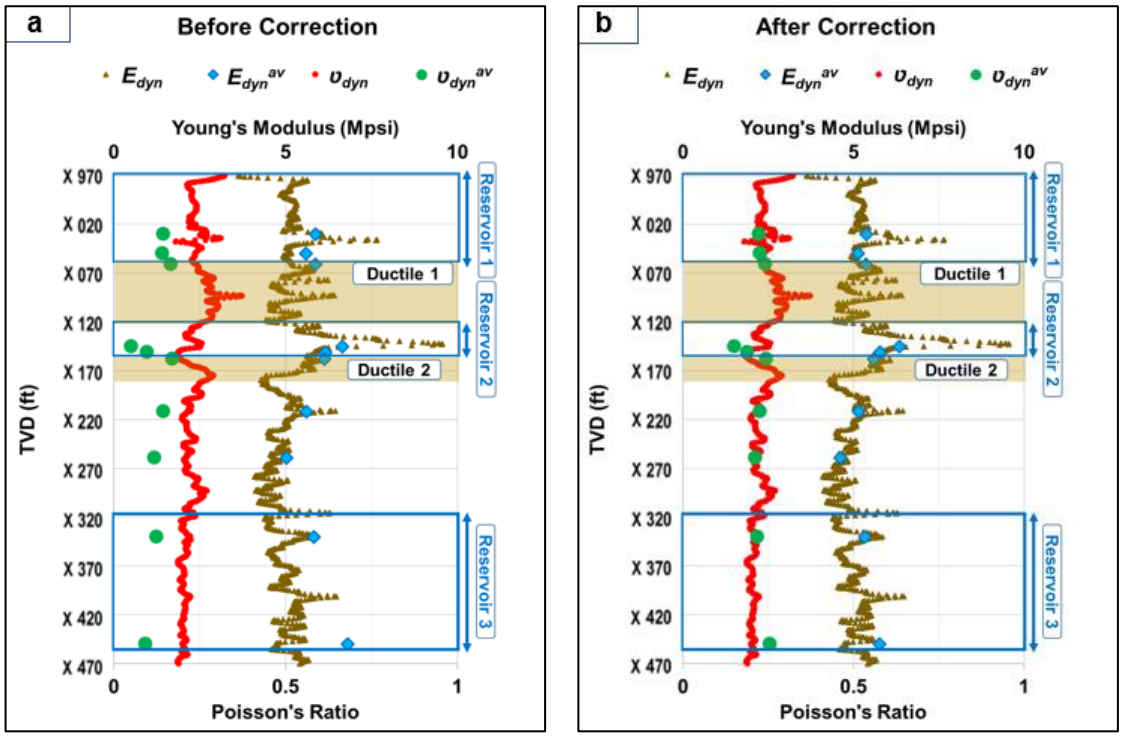

Figure 24: Derived mechanical properties from well logs and acoustic measurements of (a) dry samples without and (b) with corrections for the saturation and temperature effects.

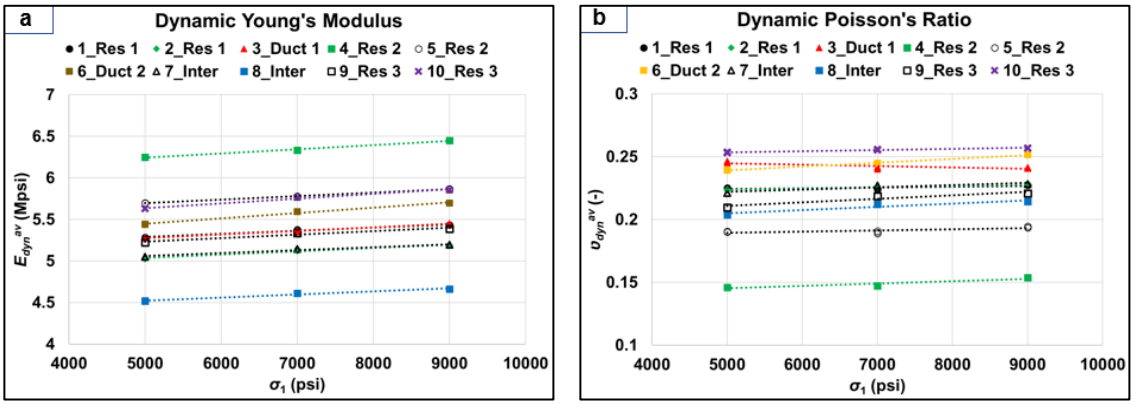

Figure 25: Estimated mechanical properties from laboratory ultrasonic measurements at constant differential stress (σ_{diff}): (a) $E_{dyn}{}^{av}$, and (b) $\upsilon_{dyn}{}^{av}$.

Table 11: Summary of slopes between effective stress and Young's modulus and Poisson's ratio.

Sample #	Zone	TVD (ft)	E_{dyn}^{av} Slope (psi/psi)	υ_{dyn}^{av} Slope (10^{-6} psi^{-1})
1	Reservoir #1	X030	37.34	0.560
2		X050	39.95	1.109
3	Ductile #1	X061	43.16	–1.042
4	Reservoir #2	X145	51.00	1.883
5		X151	41.34	0.936
6	Ductile #2	X158	64.65	3.106
7	Intermediate	X212	35.71	1.778
8	Zone	X259	36.38	2.590
9	Reservoir #3	X340	41.02	2.793
10		X450	56.44	0.890

3.3.2 Dynamic-to-Static Correction Factor (F_{ds})

3.3.2.1 Simplified Dynamic-to-Static Correction Factor (F_{ds})

Table 8 summarizes the derived F_{ds} values for the five available triaxial measurements from Benge et al. (2021). The F_{ds} values were 0.95 and 0.83 for Reservoirs 1 and 3, respectively, and were higher than those in Ductile layers 1 and 2, which had values of 0.77 and 0.55. These high F_{ds} values were found in zones of high neutron porosity (PHIN) of approximately 22% and low bulk density (RHOB) of approximately 2.48 g/cc, as illustrated in Figure 26.a, in contrast to other zones. Reservoir 2 showed a relatively low F_{ds} value of 0.47, which was closer to the values observed in the ductile layers. This is possibly due to the sample being retrieved near a depth where the well logs change dramatically, around X150 ft within Reservoir 2, which corresponds to the lowest PHIN in the entire interval. Due to the limited number of E_{stat} measurements along the depth, a simple assumption was made to use a constant F_{ds} for each lithological layer, as shown in Figure 26.b. Based on this assumption, the F_{ds} profile was constructed, and the static Young's modulus profile was derived (E_{stat}^{*}). The F_{ds} for the intermediate zone was

considered analogous to that of Reservoir 3, as both zones exhibit similar average PHIN and RHOB values. However, there are significant differences between the static-to-dynamic values in Ductile layers, presumably due to their relatively low porosity and high bulk density. Again, Reservoir 2 indicated the largest gap, potentially due to the sample selection bias as discussed above. It should be noted that using a constant F_{ds} approach results in slight jumps in E_{stat}^{*} values between layers, unlike the smooth E_{dyn} profile along the depth. Thus, we applied K-means clustering and PCA to derive more accurate F_{ds} values and E_{stat}^{*} profiles from well logs and XRF datasets, which account for the stratigraphic layers.

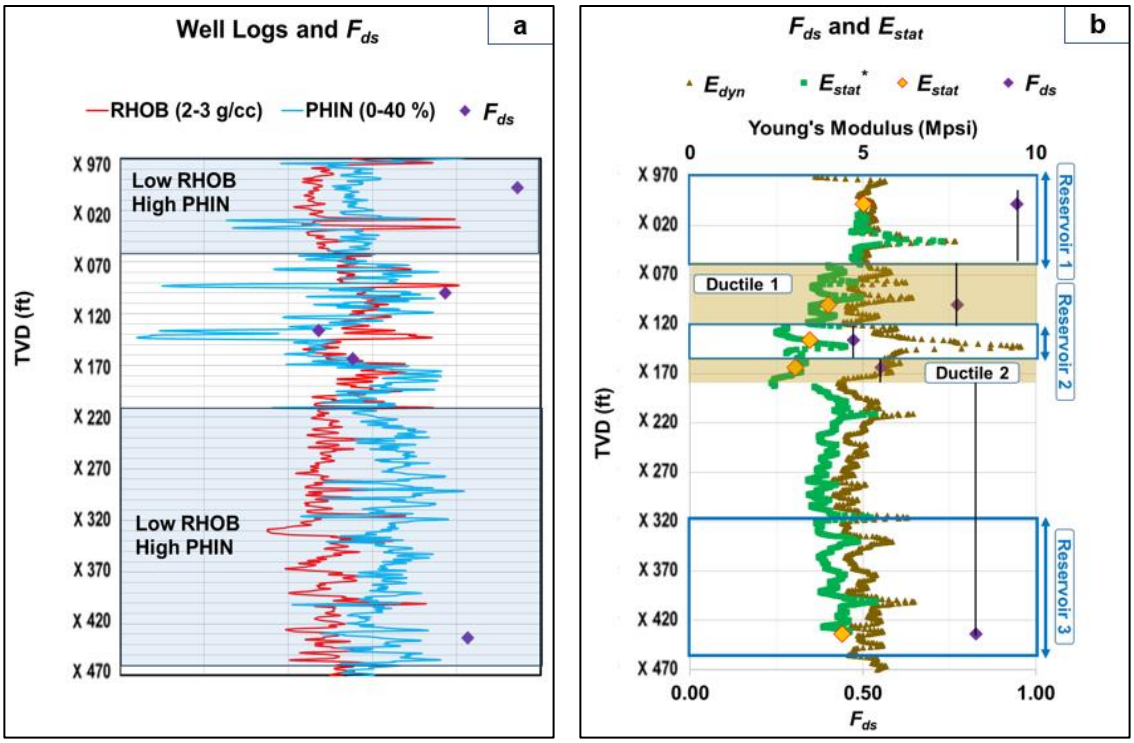

Figure 26: (a) The relationship between F_{ds}, neutron porosity (PHIN), and bulk density (RHOB). (b) Constant F_{ds} and E_{stat} profiles for Caney shale (Kholy et al., 2024).

3.3.2.2 F_{ds} Prediction using PCA-IDW Workflow

The dynamic-to-static correction factor (F_{ds}) was predicted using the previously described PCA-IDW workflow, and the static Young's modulus (E_{stat}^{*}) was then inferred from the predicted F_{ds}. This workflow was utilized to evaluate F_{ds} predictions using three datasets: the well logging dataset (Scenario 1), the XRF dataset (Scenario 2), and the combination of both datasets (Scenario 3). For each scenario, a scree plot was constructed to determine the optimal number of principal components (PC) based on a cumulative explained variance of greater than 0.7 (≥0.7). Figure 27 summarizes the scree plots, with black arrows indicating the optimal number of PCs: 3 for Scenario 1 (Figure 27.a), 5 for Scenario 2 (Figure 27.b), and 7 for Scenario 3 (Figure 27.c).

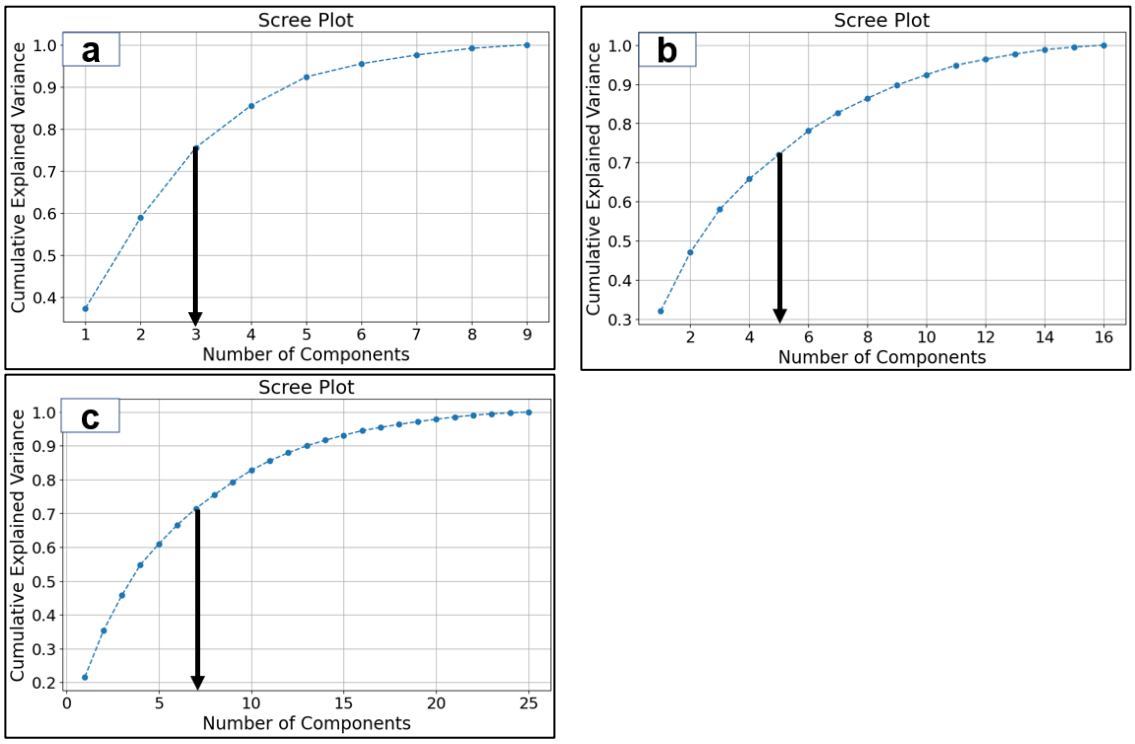

Figure 27: Principal component analysis optimization using scree plot, which shows the cumulative explained variance versus the number of components for: (a) Well logging data, (b) XRF data, and (c) Combined data. The black arrows point to the optimum number of components which corresponds to a cumulative explained variance of >0.7.

Based on the PC optimization, F_{ds} values were predicted for each scenario using the PCA-IDW workflow. Figure 28 illustrates the predicted F_{ds} values (black dots) along with the five F_{ds} values assumed for each layer from our previous study (Kholy et al., 2024) (green lines). Also, the root mean square error (RMSE) between the predicted and assumed F_{ds} was evaluated for each of the reservoir and ductile zones for the three scenarios.

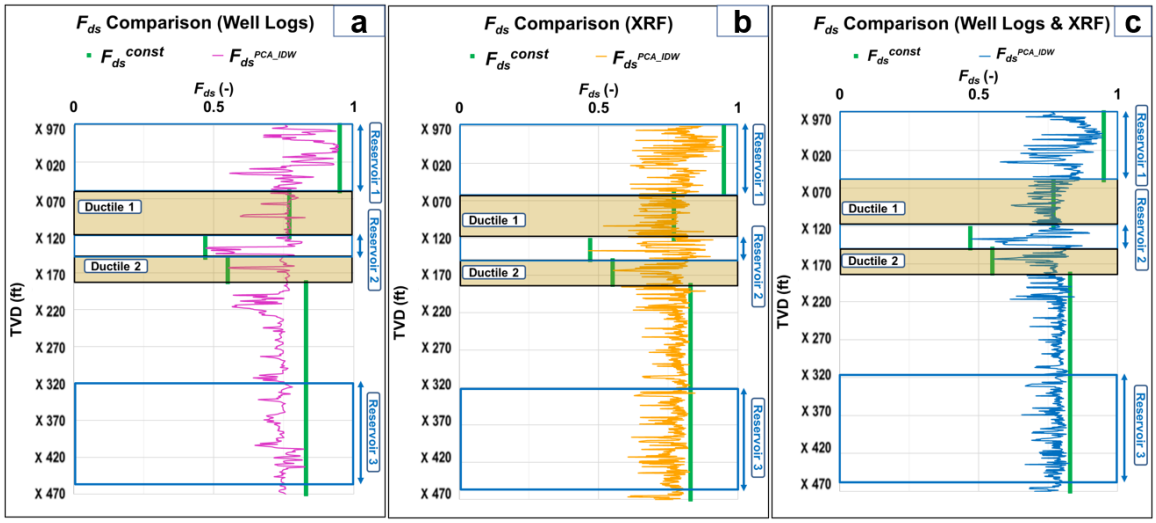

Figure 28: Predicted F_{ds} using PCA-IDW workflow from: (a) Well logging data (pink curve), (b) XRF data (orange curve), and (c) Combined data (blue curve). The five green vertical lines represent the available F_{ds} values.

For the Reservoir 1 zone, the predicted F_{ds} from Scenario 1 (Figure 28.a) matched the constant F_{ds} assumption of 0.95 only in the middle portion with an RMSE value of 0.17, while Scenario 2 (Figure 28.b) and Scenario 3 (Figure 28.c) predicted lower F_{ds} values ranging from 0.57 to 0.93 across almost the entire interval of Reservoir 1 with RMSE values of 0.17 and 0.15, respectively. This suggests that the core sample examined by Benge et al. (2021) was taken from a high-stiffness interval in Reservoir 1 and may not be fully representative of the entire zone, which, as explained earlier, is highly heterogeneous. For the Ductile 1 zone, the predicted F_{ds} values from all three scenarios closely matched the constant F_{ds} of 0.77, as this zone is predominantly siltstone-mudstone banded facies.

The RMSE values for Ductile 1 were 0.04, 0.07, and 0.05 for Scenarios 1, 2, and 3, respectively.

The Reservoir 2 zone showed the greatest offset, exceeding the assumed constant F_{ds} of 0.47 for all three scenarios, with values ranging between 0.5 and 0.85. The examined core sample was presumably retrieved from the detrital dolomitic thin layer (the second black thin layer of Figure 31) of the highly heterogeneous Reservoir 2. Consequently, it has a low F_{ds} value due to its high dynamic Young's modulus and low static Young's modulus, attributed to its detrital state (Yin and Xie, 2019). The RMSE values for Reservoir 2 zone were 0.25, 0.31, and 0.27 for the three scenarios in order, respectively. The Ductile 2 zone also indicated that the assumed F_{ds} of 0.55 is too low, representing the lower bound of the predictions for the entire interval in all three scenarios. The core sample for Ductile 2 was likely selected from the packstone-grainstone detrital carbonate thin layer, resulting in a low F_{ds} value. The RMSE values for the three scenarios were 0.2, 0.21, and 0.21, respectively.

For the intermediate and Reservoir 3 layers, the predicted F_{ds} profiles from Scenarios 2 and 3 were nearly constant and closely aligned with the assumed constant F_{ds} of 0.83. The values for these two scenarios were 0.08 and 0.07, respectively. Scenario 1 predicted a lower F_{ds} profile, with values ranging between 0.6 and 0.72, though it still exhibited relatively constant F_{ds}, and the RMSE value was 0.1. The static Young's modulus (E_{stat}^{*}) was then derived from the predicted F_{ds} for the three scenarios and compared to the dynamic Young's modulus (E_{dyn}) as shown in Figure 29.

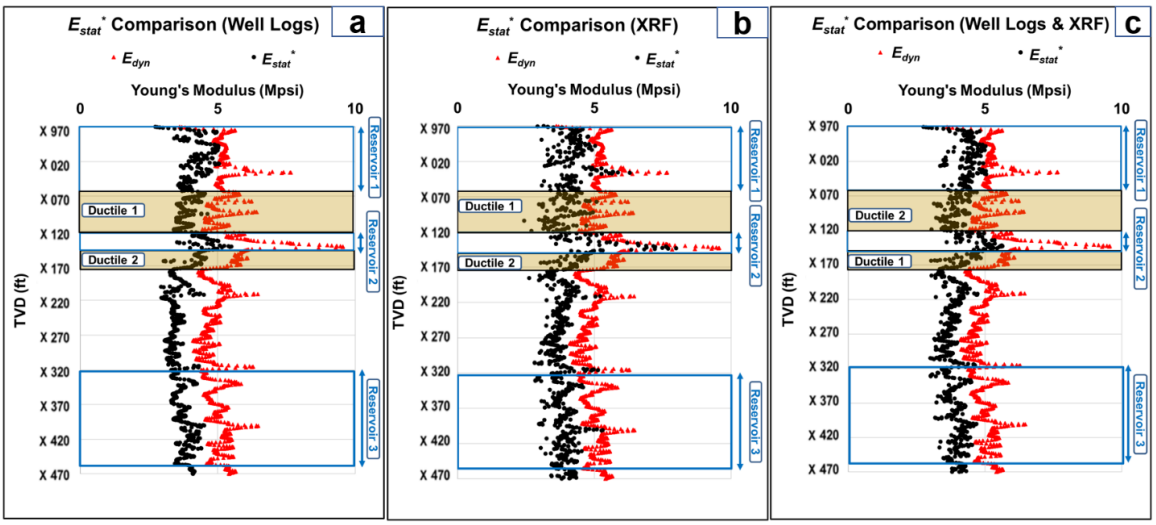

Figure 29: Derived E_{stat}^* from the predicted F_{ds} using PCA-IDW workflow from: (a) Well logging data, (b) XRF data, and (c) Combined data. The black dots are the predicted values from the PCA-IDW workflow, and the red dots represent the predicted E_{dyn} from well logs.

3.3.2.3 Depositional Facies Prediction using K-Means Clustering

To predict the depositional facies column from the K-means clustering, we evaluated the same three scenarios. The first step is to determine the optimum number of clusters for each of the three scenarios, which corresponds to the number of facies units. This optimization was performed using the Elbow and Silhouette methods (described in Appendix A), and the results show good agreement between the two methods.

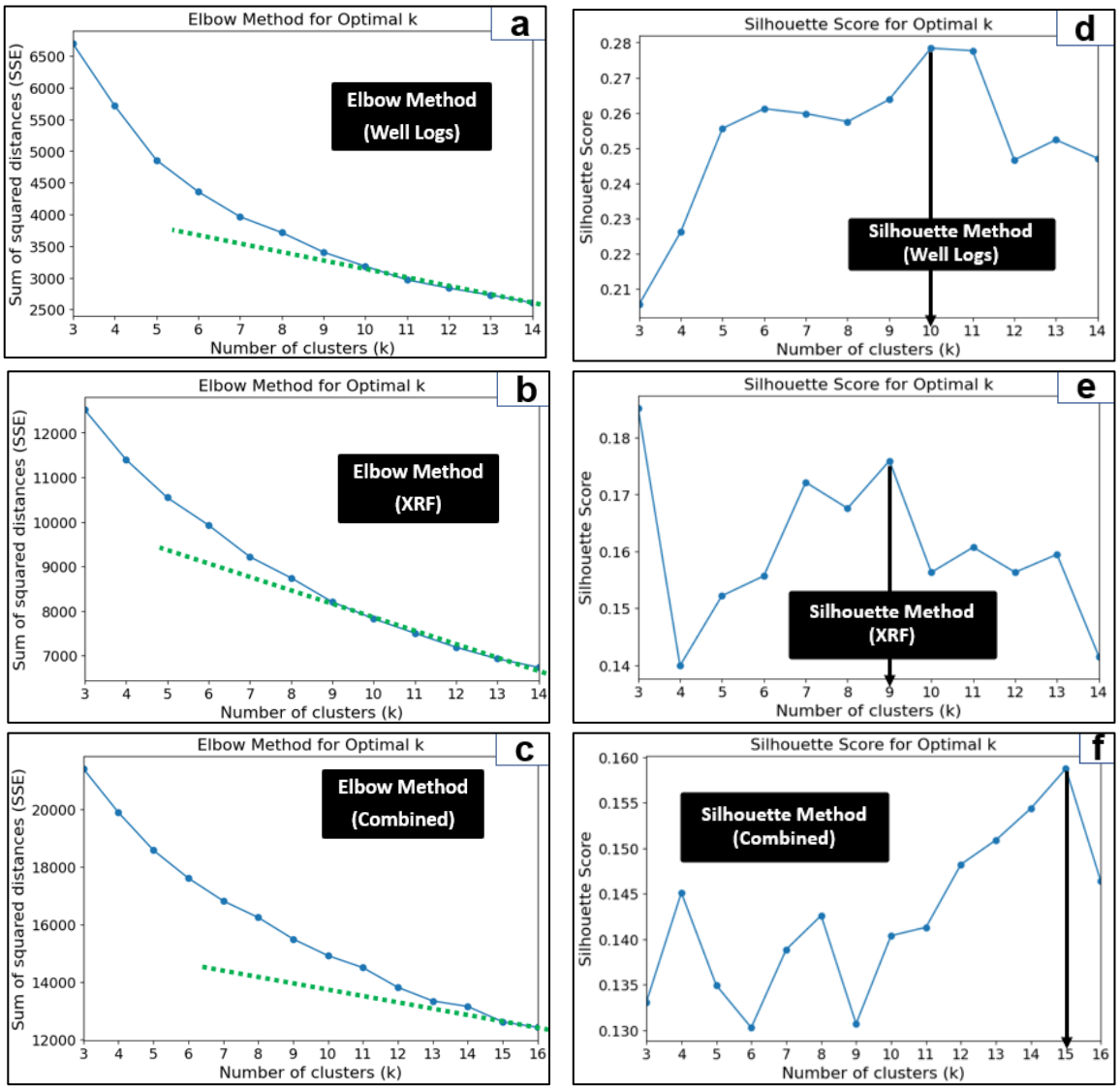

Figure 30: K-means optimization methods to find the optimum number of clusters. Elbow method plots the number of clusters (k) versus sum of squared distances error (SSE) for each of the three scenarios including (a) well logs data, (b) XRF data, and (c) combined data. Silhouette method plots the number of clusters (k) versus Silhouette score for the same three scenarios as in (d), (e), and (f) respectively. The black arrows point to the optimum k value.

The results indicate that Scenario 1, the well logging dataset, has an optimum number of clusters of 10. This scenario also shows the lowest with-in cluster sum of squares (WCSS) of 3,400 (Figure 30.a) and the highest Silhouette score of 0.278 (Figure 30.d) compared to the other two scenarios. For Scenario 2, the XRF dataset, the optimum number of clusters

is 9, which corresponds to a WCSS of 8,700 (Figure 30.b) and a Silhouette score of 0.175 (Figure 30.e). For Scenario 3, the combined dataset has an optimum number of clusters of 15, corresponding to WCSS of 12,600 (Figure 30.c) and a Silhouette score of 0.159 (Figure 30.f).

3.3.2.3.1 Prediction from Well Logging Data

Figure 31 shows the color-coded well logs from the K-means optimization. In the color-coded well logs, Reservoir 1 zone is predominantly composed of cluster 7 (orange), corresponding to rudstone carbonate facies, with relatively high DTC and DTS values of 72 µs/ft and 128 µs/ft, respectively. Also, cluster 4 (pink) and cluster 5 (yellow), represent packstone and grainstone carbonate facies, with lower DTC and DTS values of 72 µs/ft and 102 µs/ft, respectively.

Ductile 1 and 2 zones were accurately predicted and represented by cluster 0 (blue), which exhibits relatively low resistivity and high DTC and DTS with 10 ohm-m, 78 µs/ft, and 138 µs/ft, respectively. As expected, the Reservoir 2 zone contains clusters the same as Reservoir 1, with the addition of cluster 6 (black), which probably represents dolomitic facies, showing lower DTC and DTS values of 56 µs/ft and 98 µs/ft, respectively.

The intermediate and top half of Reservoir 3 zones are highly layered, with a pronounced presence of cluster 1 (green), likely representing alternating burrowed mudstone and bioturbated siltstone, with relatively high DTC and DTS values of 75 µs/ft and 132 µs/ft, respectively. Also, cluster 3 (cyan) appears as very high resistivity layers of 1,950 ohm-m, possibly indicating high hydrocarbon saturation. In addition, clusters 2 (red), cluster 7 (orange), and 9 (gray) are present but less prominent. Finally, the bottom half of Reservoir 3 is characterized by cluster 9 (gray), representing muddy carbonate facies, with medium

resistivity of 50 ohm-m, while DTC and DTS values were the same as those in Reservoir 1.

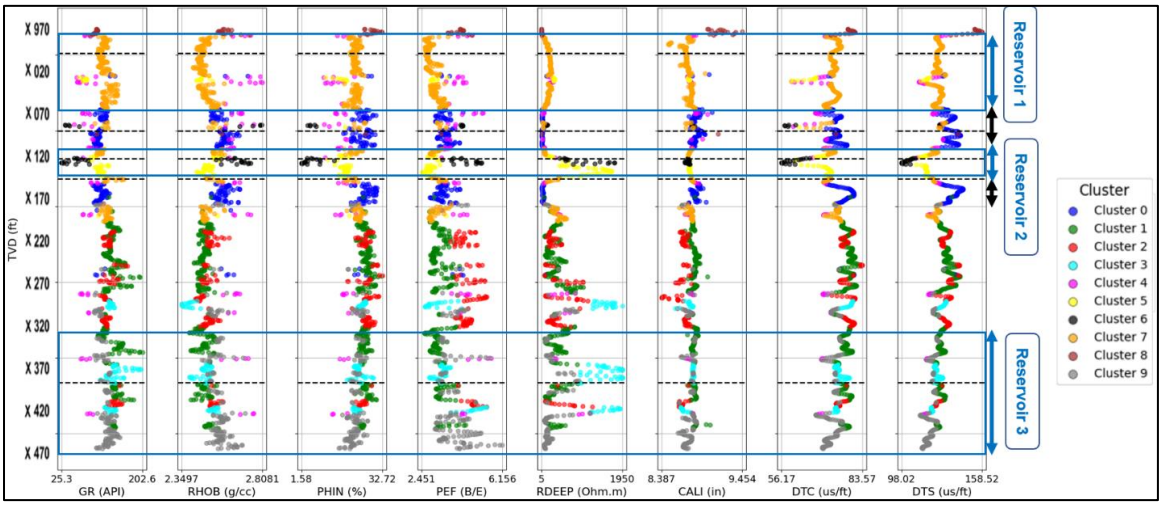

Figure 31: K-means clustering for the well log dataset (Scenario 1) based on the optimum 10 clusters. From left to right, the well logging data include GR, RHOB, PHIN, PEF, RDEEP, CALI, DTC, and DTS. The dashed lines represent the depths for the five samples from Benge et al. (2021). The blue boxes and vertical double-headed blue arrows highlight the reservoir zones, while the vertical double-headed black arrows indicate ductile zones.

3.3.2.3.2 Prediction from XRF Data

The color-coded XRF data from the K-means optimization showed a total of 9 clusters (Figure 32). Reservoir 1 and 2 zones were predominantly composed of cluster 4 (pink), which is made of relatively high Ca and low Al contents, confirming the domination of carbonate facies for the Reservoir zones. Ductile 1 zone was successfully distinguished by some presence of cluster 5 (yellow), characterized by a relatively higher Al content, indicating the presence of bioturbated siltstone. Ductile 2 zone was not clearly distinguishable from the intermediate zone, and both consisted of clusters 0 (blue) and 2 (red). The top half of Reservoir 3 was dominantly cluster 2 (red), which was characterized by relatively high Si and Al and low Ca, indicating the high presence of bioturbated

siltstone and burrowed mudstone. Lastly, the bottom half of Reservoir 3 was represented by interval 4, dominated by cluster 5 (yellow-colored) with relatively high Zr, Al, and Si contents and low Ca content.

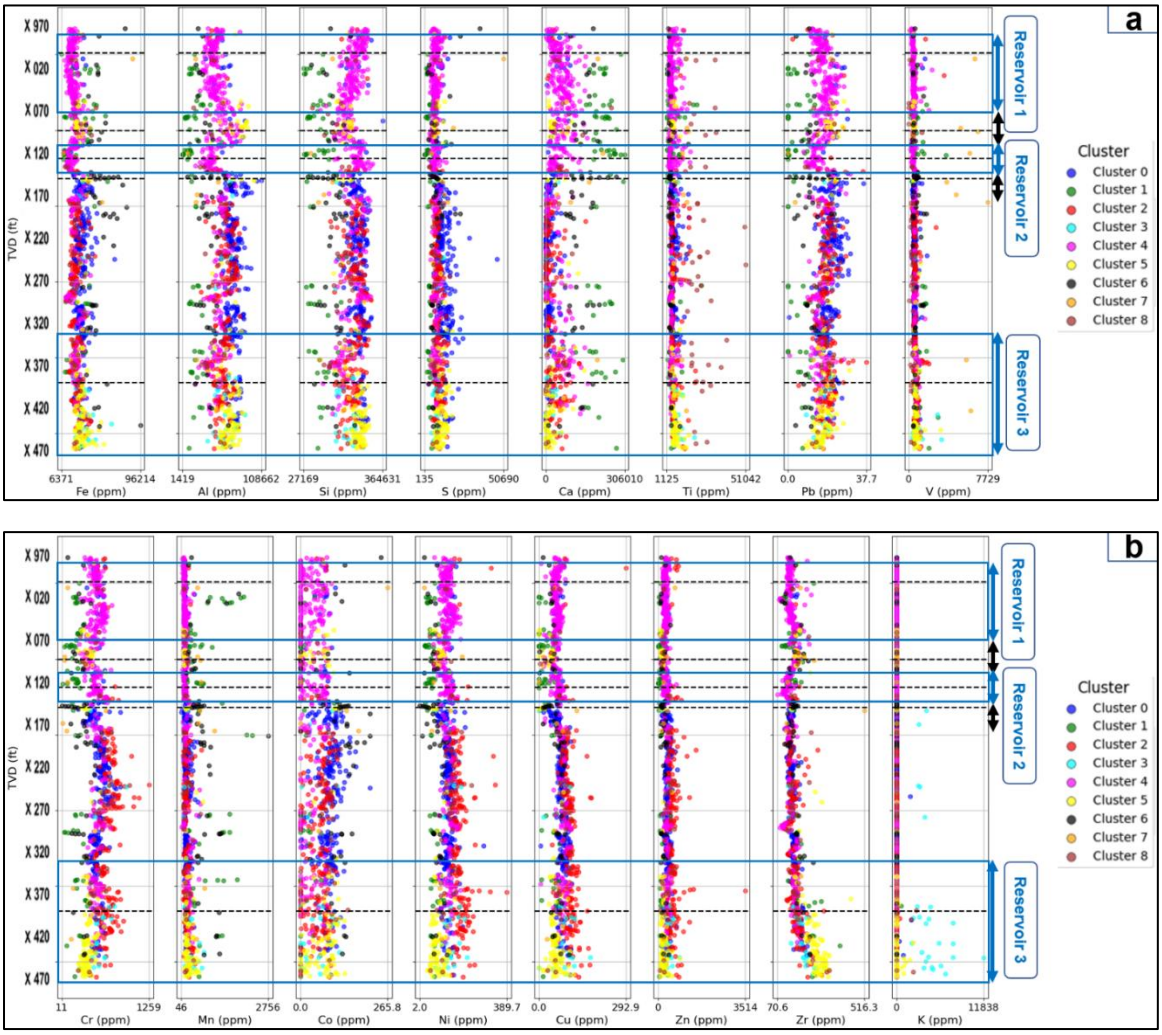

Figure 32: K-means clustering results for the XRF dataset (Scenario 2) based on the optimum 9 clusters: (a) First set including Fe, Al, Si, S, Ca, Ti, Pb, and V (b) Second set including Cr, Mn, Co, Ni, Cu, Zn, Zr, and K. The dashed lines represent the depths for the five samples from Benge et al. (2021). The blue boxes and vertical double-headed blue arrows highlight the reservoir zones, while the vertical double-headed black arrows indicate ductile zones.

3.3.2.3.3 Prediction from Combined (Well Log and XRF) Data

Figure 33 shows the optimized color-coded combined datasets for Scenario 3. This scenario yielded 15 clusters, with predicted finer layers compared to the other two scenarios. Reservoir 1 zone was clearly identified; it was made of cluster 2 (red-colored) with a thin layer of cluster 6 (black-colored) that corresponds to the dolomitic facies. Ductile 1 and Ductile 2 zones were dominated by cluster 0 (blue-colored) and cluster 1 (green-colored), while Reservoir 2 was dominated by clusters 2 and 6 as Reservoir 1 since it is dominated by the same carbonate facies. The intermediate zone was made of several fine clusters, especially Cluster 2 (red-colored) and cluster 5 (yellow-colored). The top half of Reservoir 3 was highly layered with alternation between clusters 5 (yellow) and 13 (light green), while the bottom half of Reservoir 3 was dominated by cluster 13 (light green).

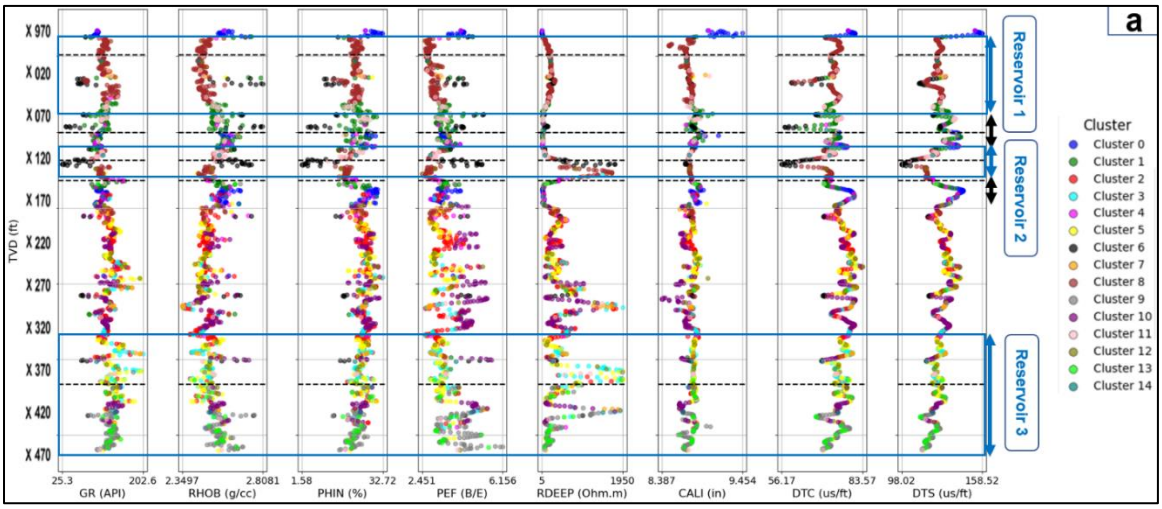

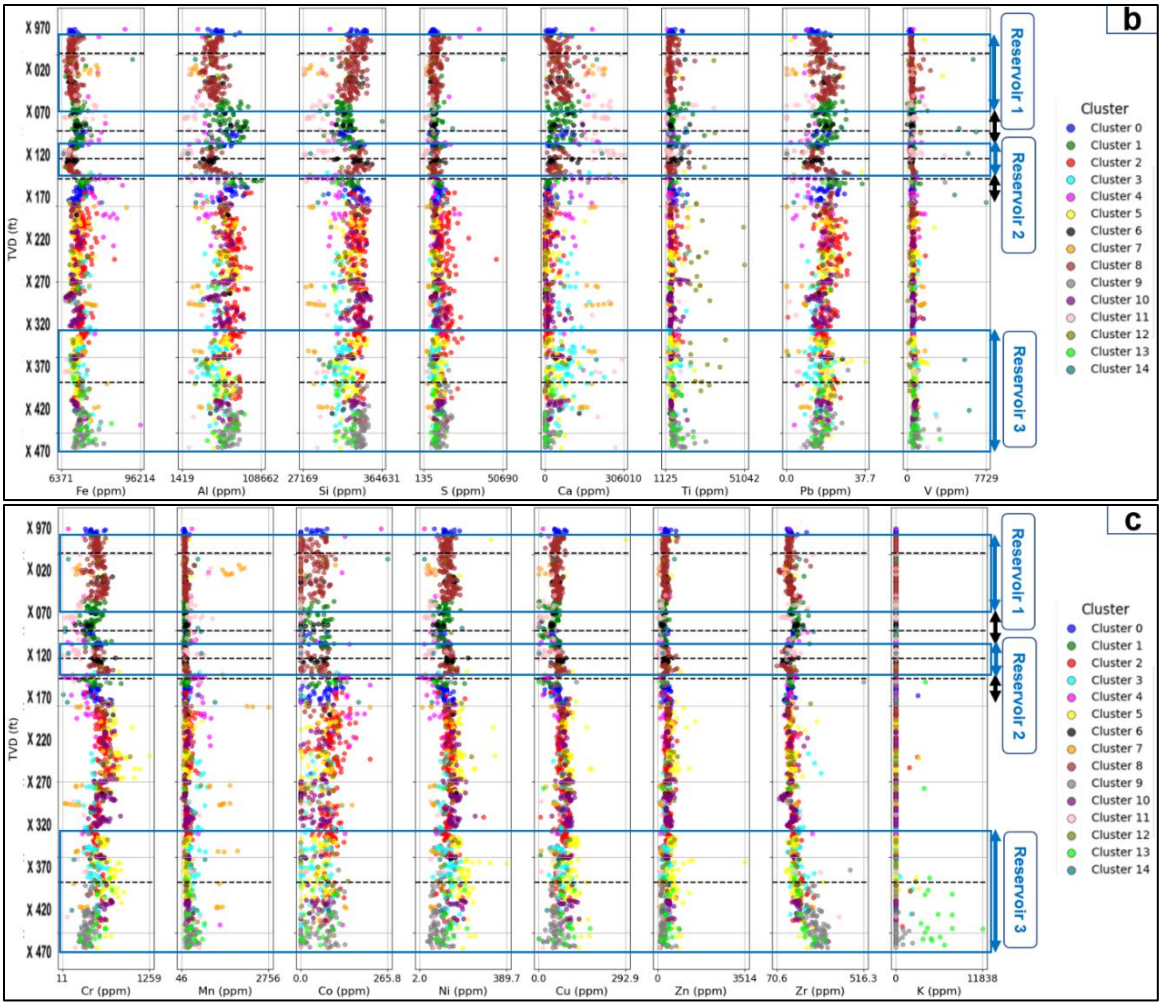

Figure 33: K-means clustering results for the combined well log and XRF dataset (Scenario 3) based on the optimum 15 clusters 15: (a) well log data, (b) first set of XRF data, and (c) second set of XRF data. The dashed lines represent the depths for the five samples from Benge et al. (2021). The blue boxes and vertical double-headed blue arrows highlight the reservoir zones, while the vertical double-headed black arrows indicate ductile zones.

3.4 Discussion

3.4.1 Stiffness Zonation using Chemostratigraphy

Optimized K-means clustering combined with chemostratigraphy was employed to validate the F_{ds} predictions and identify the lithological variations along the Caney interval, which indicate changes in stiffness. Reese (2013) demonstrated the use of XRF data for

the Woodford shale in southern Oklahoma to differentiate ductile, detrital carbonate, authigenic quartz, and detrital quartz layers through chemostratigraphic evaluation. Of these, authigenic quartz exhibits high stiffness, while detrital quartz shows lower stiffness (Dong et al., 2017). The study utilized four terrigenous XRF elements: Si, Ti, Zr, and Al. Si indicates silt-to-sand sized quartz (SiO_2) grains, Ti corresponds to rutile (TiO_2) grains, Zr to zircon ($ZrSiO_4$) grains, and Al reflects alumina-silicate clay minerals, such as illite, smectite, and chlorite. Authigenic quartz is distinguished by high Si content and low levels of Ti, Zr, and Al, whereas detrital quartz is marked by high Si, Ti and Zr contents but low Al. Detrital carbonates are characterized by low contents of all four elements, while ductile zones are identified by low Si content but high Ti, Zr, and Al levels.

Using this approach, the stiffness zonation for the Caney shale interval was determined through optimized K-means clustering applied to the XRF dataset (Figure 34). The average elemental composition for Si, Al, Ti, and Zr was calculated for each of the nine clusters, followed by a chemostratigraphic analysis to classify the layer type for each cluster (Table 12). The study revealed that Clusters #1 and #6 corresponded to detrital carbonate, characterized by relatively low Si, Al, Ti, and Zr contents. Clusters #2 and #4 exhibited relatively high Si values (247,799 ppm) and low Al, Ti, and Zr values, consistent with the characteristics of authigenic quartz. Cluster #3 displayed characteristics of detrital quartz with relatively high Ti (7,193 ppm) and Zr (193 ppm) values, along with lower Si and higher Al compared to the authigenic quartz. Clusters #5 and #7 were identified as ductile layers, featuring higher Al, Ti, and Zr contents and lower Si compared to quartz layers. Finally, Clusters #0 and #8 showed high levels of Si (249,252 ppm), Al (66,463 ppm), Ti (7,824 ppm), and Zr (153 ppm), suggesting the presence of clay-rich layers.

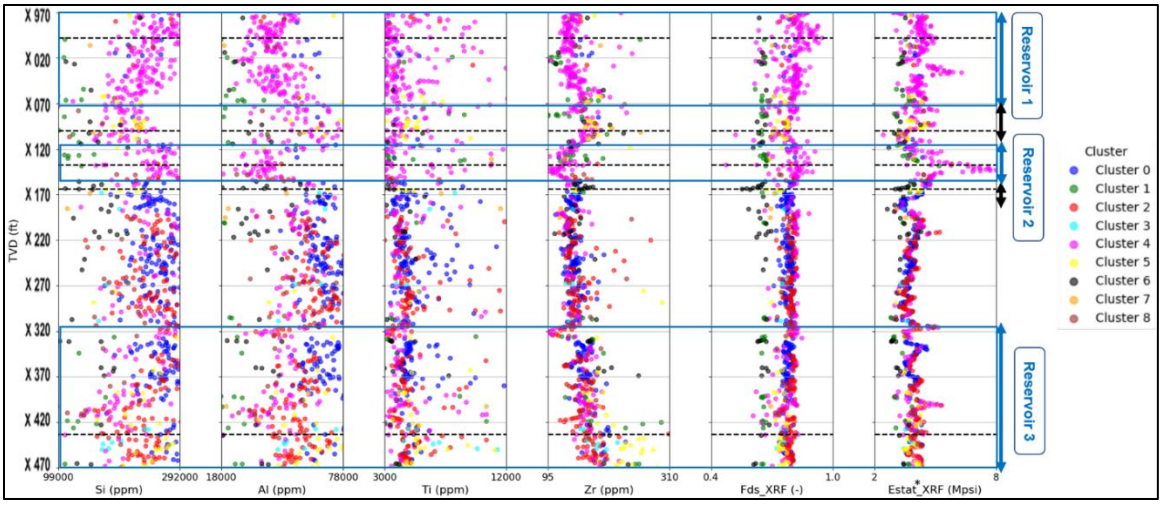

Figure 34: K-means clustering results for the XRF dataset (Scenario 2) highlighting the four terrigenous elements including Si, Al, Ti, and Zr along with the predicted F_{ds} and E_{stat}^{*} using PCA-IDW workflow from Scenario 2. The authigenic quartz (pink and red), the detrital quartz (cyan), the detrital carbonate (green and black), and the ductile (orange and yellow) zones were identified from the chemostratigraphic analysis following Reese (2013). The dashed lines represent the depths for the five samples from Benge et al. (2021). The blue boxes and vertical double-headed blue arrows highlight the reservoir zones, while the vertical double-headed black arrows indicate ductile zones.

Figure 34 shows the predicted F_{ds} and E_{stat}^{*} profiles from Scenario 2 along with the four terrigenous elements, and Table 12 summarizes the average values for these predictions for the identified five layers from chemostratigraphic analysis. The authigenic quartz exhibited the highest average static Young's modulus at 4.17 Mpsi, while the detrital quartz and detrital carbonate layers had lower values of 3.97 Mpsi and 3.39 Mpsi, respectively, consistent with Dong et al. (2017). The clay-rich and ductile layers had intermediate stiffness values of 4.06 Mpsi and 3.87 Mpsi, respectively. The consistency between the stiffness zonation and chemostratigraphic analysis validates the reliability of the predicted F_{ds} profile derived from the XRF data (Scenario 2) for the Caney shale interval.

Table 12: Summary of the predicted F_{ds} and E_{stat}^{*} from XRF dataset along with the average composition of the four terrigenous elements (Si, Al, Ti, and Zr) for the five identified layer types from the chemostratigraphic analysis following Reese (2013).

Layer Type	Cluster #	Colors	Si (ppm)	Al (ppm)	Ti (ppm)	Zr (ppm)	F_{ds_XRF} (-)	$E_{stat}^{*}{}_{\_XRF}$ (Mpsi)
Carbonate (Detrital)	1, 6	green, black	112,247	24,671	4,152	161	0.65	3.39
Ductile	5, 7	yellow, orange	239,675	64,536	6,504	244	0.74	4.06
Quartz (Authigenic)	2, 4	red, pink	247,799	50,721	5,015	147	0.79	4.17
Quartz (Detrital)	3	cyan	204,413	60,058	7,193	193	0.73	3.97
Clay-Rich	0, 8	blue, brown	249,252	66,463	7,824	153	0.77	3.87

3.5 Conclusions

In this study, we experimentally evaluated the impact of reservoir depletion on the derived dynamic mechanical properties from the measured acoustic velocities for Caney shale using a triaxial Hoek cell. Increasing effective stress resulted in an increase in dynamic Young's modulus for all ten samples. However, there was no clear correlation between effective stress and Poisson's ratio. In general, the results showed a direct correlation for samples from reservoir layers, whereas inverse or no correlation for samples from ductile layers.

In addition, we introduced a new workflow to predict the dynamic-to-static correction factor (F_{ds}) —ratio between static-to-dynamic Young's modulus—along the emerging Caney shale reservoir in south-central Oklahoma. First, the workflow incorporated optimized principal component analysis (PCA) and inverse distance weighting (IDW) to predict F_{ds} profiles from five available static Young's modulus triaxial measurements, and petrophysical data for three scenarios including (1) conventional well logging data, (2)

XRF data, and (3) a combination of both datasets. Second, the approach involved optimizing K-means clustering for the same three scenarios to identify the main Reservoir and Ductile zones along the Caney shale interval. All three scenarios successfully identified the three primary reservoir zones, where Reservoirs 1 and 2 were characterized by homogeneous carbonate facies. In contrast, Reservoir 3 exhibited a highly layered composition, with burrowed mudstone and bioturbated siltstone at the top and muddy carbonate facies at the bottom. Additionally, all scenarios recognized Ductile 1 zone, while only Scenarios 1 and 2 identified Ductile 2 zone. The stiffness zonation was inferred from the XRF dataset (Scenario 2) using chemostratigraphic analysis, and it showed good consistency with the predicted F_{ds} and E_{stat}^{*} profiles for the same scenario from PCA-IDW workflow with high E_{stat}^{*} values corresponding to authigenic quartz zones and low E_{stat}^{*} values associated with detrital quartz and carbonate zones. The results also indicated that the samples selected for triaxial testing were representative of Ductile 1 and Reservoir 3 zones, while the remaining three samples were likely not representative. This workflow can be extended to other unconventional shale reservoirs, providing a valuable tool for accurately predicting mechanical properties, which are essential for enhancing production strategies and optimizing drilling and stimulation programs.

3.6 Acknowledgment

The authors would like to thank the US Department of Energy under Grant # DE-FE0031776 for their great support and for their permission to provide the core samples, the well logging data, and the X-ray flouresence (XRF) data that were utilized in this study.

CHAPTER IV

4 Inferring Natural Fracture Characteristics in Shale Rocks from Acoustic Waveforms using Supervised Machine Learning

Abstract

Characterizing natural fractures is critical for optimizing drilling programs and production strategies in shale reservoirs. This study combines measured acoustic P, S1, and S2 waveforms with supervised machine learning to predict fracture characteristics in shale rocks. Five Caney and Eagle Ford shale samples were analyzed using a triaxial Hoek cell to assess the effects of fracture strike, dip, and volume on acoustic properties, including velocity, shear wave splitting (SWS), amplitude, and wavelength. The recorded waveforms trained K-nearest neighbors (KNN) and extreme gradient boosting (XGBoost) models to predict P, S1, and S2 waveforms based on travel time, fracture features, shale type, and testing conditions.

The results indicated that SWS was most pronounced in fractured samples, averaging 3%, compared to less than 1% in intact samples. Fracture strike and dip negatively correlated with SWS, while fracture volume and density showed a positive correlation. The KNN model produced smoother, more continuous waveforms, aiding arrival time estimation, whereas XGBoost demonstrated higher R-squared values for predicting all three waveforms. These findings contribute to estimating natural fracture characteristics in shale,

providing valuable insights for optimizing well drilling and stimulation strategies in subsurface engineering.

4.1 Introduction

Natural fractures are common mechanical discontinuities in most rock formations, particularly in carbonates and shales (Gale et al., 2007; Moore and Wade, 2013). These pre-existing discontinuities can pose significant challenges during drilling, such as mud loss (Razavi et al., 2017) and drilling breaks (Narr et al., 2006). From a production engineering perspective, natural fractures may enhance local permeability, potentially increasing the production rate (Luffel et al., 1993; Sakhaee-Pour and Bryant, 2011; Ben et al., 2012; Al-Rubaye et al., 2020). However, they can also lead to negative outcomes, such as elevated gas-oil ratios and higher water cuts, reducing hydrocarbon recovery efficiency (Aguilera, 1980; Wennberg et al., 2016). Additionally, in hydraulic fracturing operations, the presence of natural fractures can significantly alter the path of hydraulic fractures and affect the Stimulated Reservoir Volume (SRV), depending on their alignment with the propagation direction of hydraulic fractures (Gale et al., 2007; Zhou et al., 2008; Bahorich et al., 2012; Lee et al., 2015; Lee et al., 2018).

The orientation of these fractures is often controlled by the paleo-stress fields from the region's most active tectonic period (Maerten and Maerten, 2006; Zhang et al., 2022). However, this alignment may not always coincide with the present-day stress field (Abul Khair et al., 2013; Abul Khair et al., 2015; Likrama et al., 2019; Lee and Olson, 2017), making fracture orientation a key factor in the design and execution of subsurface engineering projects. Additionally, fracture density is another critical characteristic that influences subsurface operations, especially drilling, as it governs the mud loss to the

formation (Razavi et al., 2017).

Natural fracture characteristics can be determined using various field-based techniques (Narr et al., 2006). Aguilera (1980) noted that fracture orientation could be detected through several geophysical tools, such as borehole imaging, caliper logs, dipmeter logs, and sonic amplitude logs. For example, vertical fractures attenuate compressional wave amplitudes, while horizontal fractures attenuate shear wave amplitudes (Pan et al., 2022). However, the reliability of this method can be compromised because acoustic amplitude is influenced by the frequency of the transmitted pulses (Tillotson et al., 2012). Dipmeter logs, often used in combination with resistivity logs, can provide insights into fracture orientation near the wellbore (Delhomme et al., 1988). In high-resistivity zones, however, dipmeter logs may need to be supplemented with borehole imagers to verify fracture orientations (Georgi, 1986), increasing costs and reducing economic efficiency. Advanced imaging techniques like computerized tomography (CT) and nuclear magnetic resonance (NMR) have also been employed to visualize fractures near the wellbore and determine their aperture, dip, and strike (Yang et al., 1998; Elsayed et al., 2021). Furthermore, mapping the locations of microseismic events has been used to infer the presence of natural fractures when they interact with stimulated fractures (Fisher et al., 2002; Warpinski, 2009; AlQassab et al., 2020). However, this method only provides information about natural fractures after stimulation has occurred.

One promising method for identifying fracture characteristics on a field scale is through the analysis of shear wave seismic profiles. This approach can also detect other subsurface anisotropies, such as layering and stress variations (Crampin, 1985; Schoenberg and Sayers, 1995). Shear wave splitting (SWS) is recorded using two orthogonal components of

seismograms, rotated incrementally from 0° to 180° in 1° steps (Martin and Davis 1987; Gholami et al. 2016; Maulana et al. 2019). Martin and Davis (1987) further demonstrated that when the incident shear wave is not aligned with the fracture plane, the split shear waves reorient to travel along and perpendicular to the fracture plane, resulting in a lower SWS value compared to cases where the waves are aligned with the fractures. Dande et al. (2019) found that intact Eagle Ford shale cores drilled parallel to bedding planes exhibited higher SWS values compared to those drilled perpendicular to the bedding planes. In another study, Ding et al. (2021) measured polarized shear wave velocities (fast wave S1 and slow wave S2) for intact, acidized, and fractured Marcellus shale, with S1 and S2 transducers aligned parallel and perpendicular to artificial fractures.

In wellbore applications, full waveform sonic logging has been used to detect natural fractures near the wellbore by observing an offset between the slowness of fast and slow shear waves (Chen, 1989; Donald et al., 2018). This technique is particularly useful for identifying fractures that are otherwise difficult to observe using conventional logging methods. However, a full characterization of these natural fractures from the acoustic waveforms is still challenging. Thus, the objective of this study is to develop supervised machine learning models to predict fracture properties of shale rocks under subsurface conditions from the acoustic P, S1, and S2 waveforms. This is achieved by experimentally evaluating the impact of natural fracture characteristics (fracture strike, dip, and volume) for five Caney and Eagle Ford shale samples on the acoustic properties of P, S1, and S2 waveforms, including acoustic velocities, amplitude, and wavelength using a Hoek cell. These measurements will then be utilized to train K-nearest neighbors (KNN) and extreme gradient boosting (XGBoost) models to predict P, S1, and S2 waveforms from travel time,

sample dimensions, shale type, and natural fracture characteristics. The findings of this study will be useful in better optimizing well drilling and stimulation programs for wells that are landed in unconventional shale formations.

4.2 Materials and Methods

4.2.1 Experimental Setup and Theoretical Background

The previously described acoustic measurement setup (Figure 23) was utilized to capture P, S1, and S2 waveforms under controlled axial stress (S_a), confining pressure (P_c), and temperature (T). The acoustic velocity (V) in Km/s was derived from the arrival time (t) in ms for each of the three waveforms, and SWS was derived from S1-wave and S2-wave velocities (V_{S1} and V_{S2}, respectively) using Equations 18 and 19 (Tillotson et al., 2012).

$$V = 0.0254\frac{L}{t} \tag{18}$$

$$\text{SWS}\ (\%) = \frac{V_{S1}-V_{S2}}{V_{S1}} \times 100 \tag{19}$$

where L is the sample length in inches.

4.2.2 Sample Description

Acoustic measurements were conducted on five cylindrical Caney and Eagle Ford shale samples to assess the effects of temperature, triaxial stresses, and various fracture characteristics— including fracture strike, dip, and volume on the P, S1, and S2 waveforms.

4.2.2.1 Caney Shale Samples

Two cylindrical downhole samples were collected from the same pilot well in southern Oklahoma, mentioned in the previous chapter, across the Caney shale interval. Samples #1 and #2 (Table 13) were cored perpendicular to the bedding planes from the Reservoir 3 and Intermediate zones (Samples #10 and #8, respectively, in Table 10). Both samples were

assumed to have the same mineralogical composition as Reservoir 3 of 61 wt% quartz, 26 wt% carbonate, and 13 wt% clay (Benge et al., 2023), since both of them belong to cluster 1 of the optimized K-means clustering (Figure 31).

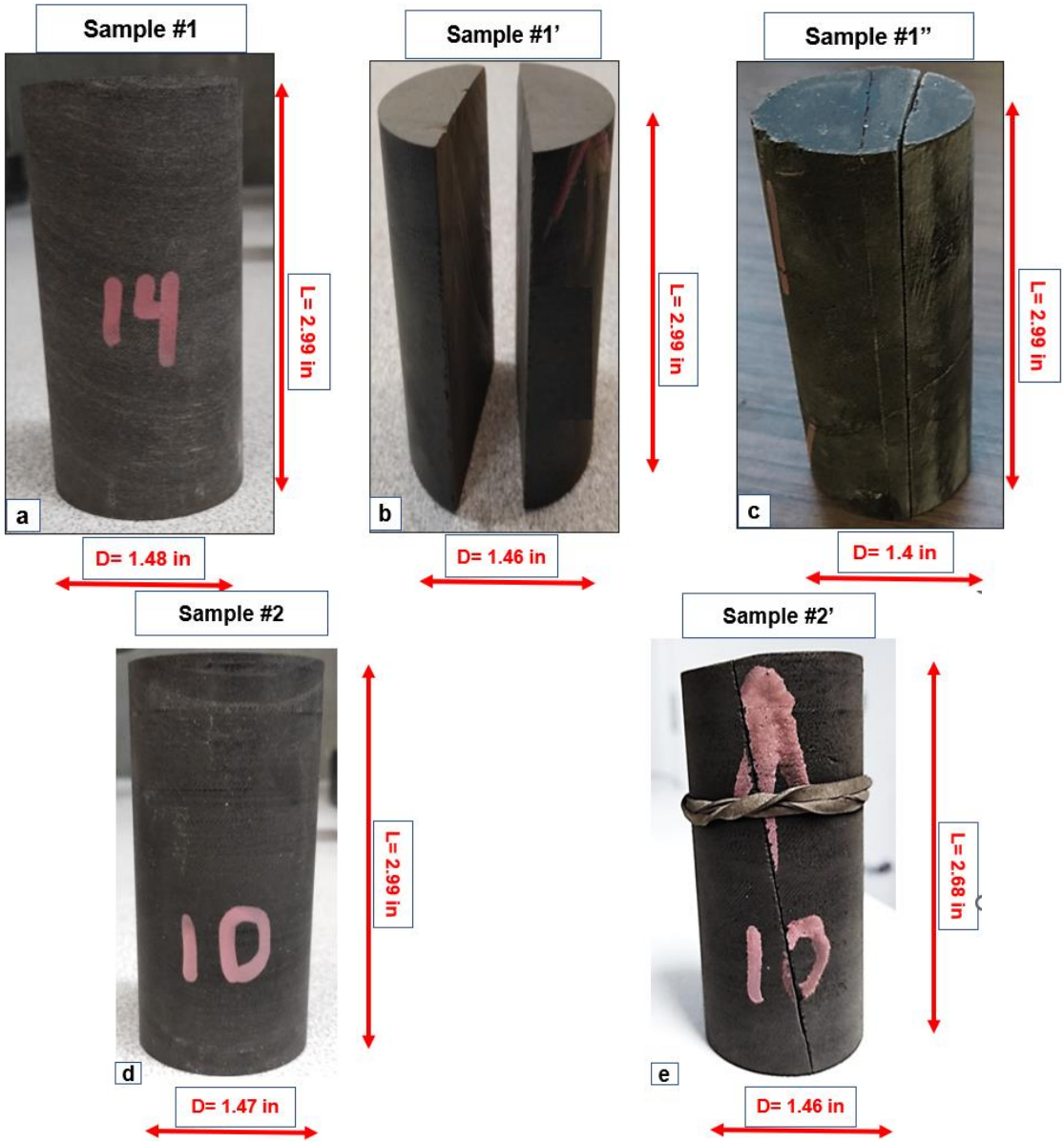

Figure 35: Caney shale samples: (a) intact sample (Sample #1), (b) a fractured sample with one vertical smooth fracture (Sample #1'), (c) a fracture sample with two vertical smooth fractures (Sample #1"), (d) intact sample (Sample #2), and (e) a fractured sample with one smooth fracture with dip of 80° (Sample #2').

For the first sample, the acoustic measurements were initially conducted on the intact

sample, referred to as Sample #1 (Figure 35.a), to compare with the fractured sample measurements. The intact sample was then sliced down the middle using a power-saw to create a vertical smooth fracture, referred to as Sample #1' (Figure 35.b), to assess the impact of the fracture strike. The additional smooth vertical fracture was then created in the same sample using a power saw (Sample #1") to evaluate the impact of fracture density (Figure 35.c). For the second Caney shale core, the acoustic measurements were evaluated first on the intact sample (Sample #2), and then the sample was sliced with a dip angle of 80° from the horizontal using a power saw to assess the impact of fracture dip (Sample #2') as shown in Figures (35.d) and (35.e), respectively.

4.2.2.2 Eagle Ford Shale Samples

In addition, three Eagle Ford cylindrical samples, cored perpendicular to the bedding planes from an outcrop in south Texas, were prepared for acoustic measurements. These samples were made of marine shale and marl with interbedded limestone, where the later represents more than 70 wt% of its mineralogical composition (Denney, 2012). A smooth vertical fracture was generated down the middle for the first sample (Sample #3') using a power saw, and then its acoustic measurements were conducted at a fracture strike of 0° and room temperature (21 °C) to serve as a base case (Figure 36.a). The second sample (Sample #4') was cored around a natural fracture in the outcrop to obtain a vertical rough fracture down the middle (Figure 36.b). To create additional fracture volume for the next sample (Sample #4"), a flat-head screwdriver was utilized to scratch both sides of the fracture wall. The acoustic waveforms have been measured for Samples #3', 4', and 4" to evaluate the impact of the fracture volume. The third sample (Sample #5') was sliced at a fracture dip of 75° to evaluate the fracture dip impact on the acoustic waveforms of the

Eagle Ford shale (Figure 36.c).

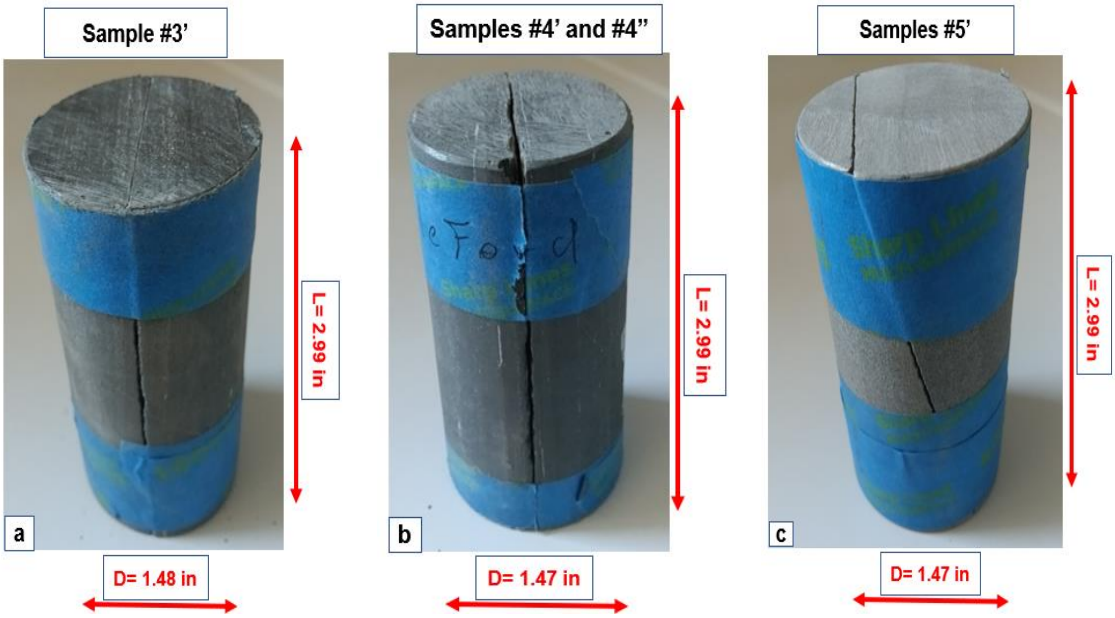

Figure 36: Eagle Ford shale samples: (a) a fractured sample with one vertical smooth fracture (Sample #3'), (b) fractured sample with one vertical rough fracture (Sample #4') and large volume (Sample #4"), and (c) a fractured sample with one smooth fracture (Sample #5') with dip of 75°.

4.2.2.3 Fracture Volume and Aperture Quantification

A Computed Tomography (CT) scan was conducted on the vertically fractured Eagle Ford samples along their lengths to quantify both the unconfined fracture aperture and volume for each of the smooth fracture (Sample #3'), rough fracture (Sample #4'), and rough fracture with larger volume (Sample #4") as summarized in Appendix B. A sensitivity analysis was conducted for each sample to determine the minimum spacing for fracture volume estimation by using 5, 10, 15, 20, and 25 equally spaced CT sections along the sample length. The total fracture volume was estimated by multiplying the sum of fracture areas estimated at each CT section by the spacing between sections. Figure 37.a summarizes the sensitivity analysis for the Eagle Ford samples, showing that the fracture volume converges above 10 CT sections for all the samples with values of 0.01, 0.09, and

0.13 in^3 for Samples #3', #4', and #4", respectively.

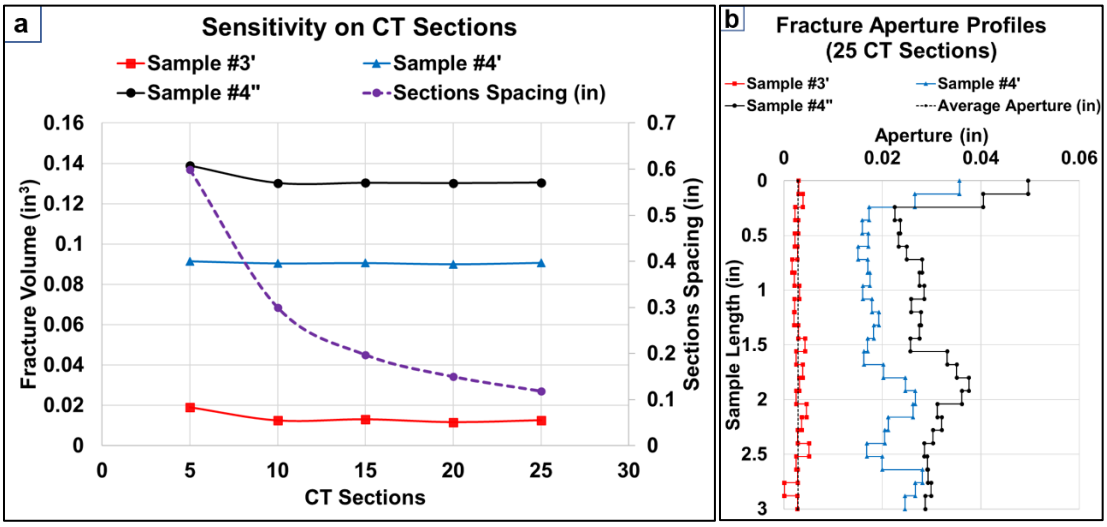

Figure 37: (a) Fracture volume with respect to the number of CT sections for Eagle Ford samples: Sample #3' (red), #4' (blue), and #4" (black). The spacing between the CT sections is in dashed purple curve. (b) Fracture aperture profiles along the sample length for Eagle Ford samples: Sample #3' (red), #4' (blue), and #4" (black). The dotted black line represents the average aperture for the smooth fracture at 2.83×10^{-3} in.

The fracture aperture is calculated by dividing the fracture area at each section by the sample diameter. The three fracture aperture profiles along the sample length are illustrated in Figure 37.b. As expected, the aperture showed minimal variation along the sample length for the smooth fracture (Sample #3') with an average value of 2.83×10^{-3} in and a range of 0 to 0.005 in. The aperture variation was larger for the rough fracture (Sample 4') with a range of 0.015 to 0.036 in, and it was the largest for the rough fracture with a large aperture (Sample 4") with a range of 0.023 to 0.05 in.

The fracture apertures for the vertically fractured samples (Samples #1' and #1"), the 75° dip fracture (Sample #5'), and the 80° dip fracture (Sample #2') were assumed to be 2.83×10^{-3} in, consistent with Sample #3', as all these fractures are smooth. The fracture volumes for these samples were calculated by multiplying the aperture by the fracture face area, which is rectangular for Samples #1' and #1" and truncated ellipsoidal for Samples

#2’ and #5’. The fracture volumes were then normalized against the volume of a typical intact sample of length (*L*), diameter (*D*), and volume values of 3 in, 1.5 in, and 5.3 in^3, respectively. Table 13 provides a summary of the samples dimensions, bulk density (*RHOB*), and fracture properties for each sample included in this study.

Table 13: Dimensions and fracture properties for Caney and Eagle Ford shale samples.

Rock Type	Rock Condition	Sample #	# of Frac.	Dip (°)	*L* (in)	*D* (in)	*RHOB* (g/cc)	Fracture Volume	
								Actual (in^3)	Normalized (in^3/in^3)
Caney	Fractured	1’	1	90	2.99	1.46	2.58	0.0124	0.0023
	Fractured	1”	2	90	2.99	1.40	2.58	0.0247	0.0047
	Intact	1	0	0	2.99	1.48	2.60	0.0000	0.0000
	Fractured	2’	1	80	2.68	1.46	2.33	0.0088	0.0017
	Intact	2	0	0	2.99	1.47	2.45	0.0000	0.0000
Eagle Ford	Fractured	3’	1	90	2.99	1.48	2.20	0.0125	0.0024
	Fractured	4’	1	90	2.99	1.47	2.45	0.0900	0.0170
	Fractured	4”	1	90	2.99	1.46	2.41	0.1300	0.0245
	Fractured	5’	1	75	2.99	1.47	2.57	0.0101	0.0019

4.2.3 Testing Procedures

A total of 41 acoustic waveforms were recorded for each of the P, S1, and S2 waves using the Triaxial Hoek to assess the effects of temperature, fracture characteristics, and stress conditions on both Caney and Eagle Ford shale samples, as shown in Table 14. The impact of stress anisotropy was tested on all fractured samples under low and high anisotropy, with S_a and P_c differing by 50 psi and 4000 psi, respectively. For high stress anisotropy, S_a values of 5000 psi and 7000 psi were used to examine the changes in effective stress during production or injection in the subsurface (Kholy et al., 2024). The temperature effect was tested on Sample #1 at 21, 50, and 95 °C, with the fracture strike set at 0° (baseline) by

aligning the vertical fracture in the N-S direction of the Hoek cell. The fracture strike was also tested at 0°, 30°, and 45° on Sample #1', while the fracture dip was evaluated at 75° on Sample #5' and 80° on Sample #2', both with a fracture strike of 0°. Fracture volume was evaluated using Samples #1' and #1" for Caney shale and Samples #3', #4', and #4" for Eagle Ford shale. Additionally, acoustic waveforms for intact Samples #1 and #2 were measured at 21 °C and 95 °C under high anisotropic stress to compare with the fractured samples.

The effects of fracture characteristics, stress, and temperature were assessed by determining the arrival time in ms, amplitude in mV, and wavelength in ms of each measured waveform (Figure 38). The acoustic velocities and SWS were then derived from the picked arrival times. For the P-wave, the compressional wave travel time was identified just before the first waveform, as illustrated in Figure 38.a, following the method outlined by Xiwei et al. (2015). For the S-waves, the shear wave arrival times were selected by pinpointing the peak of the first waveform with high amplitude and short wavelength, as shown in Figures 38.b and 38.c, using the standard procedure described by Crampin (1981).

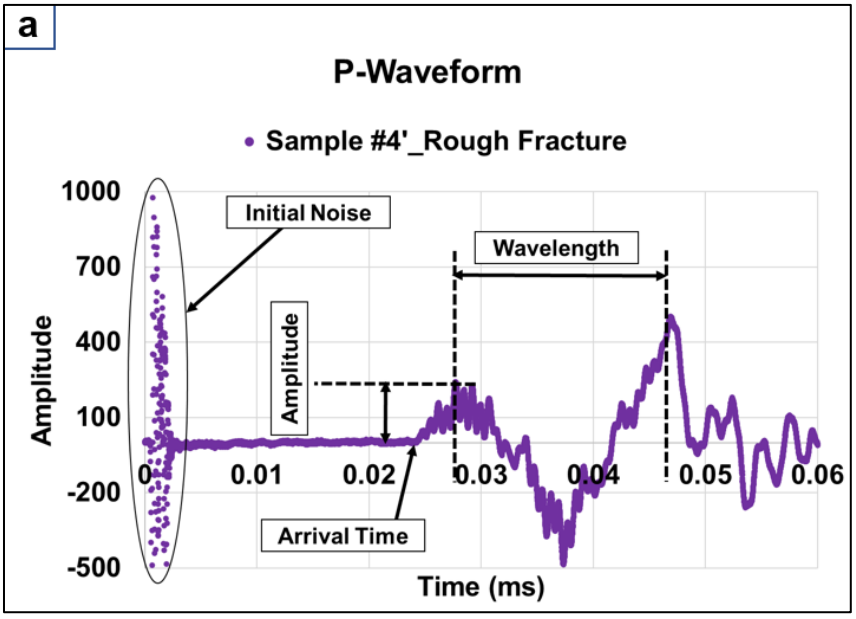

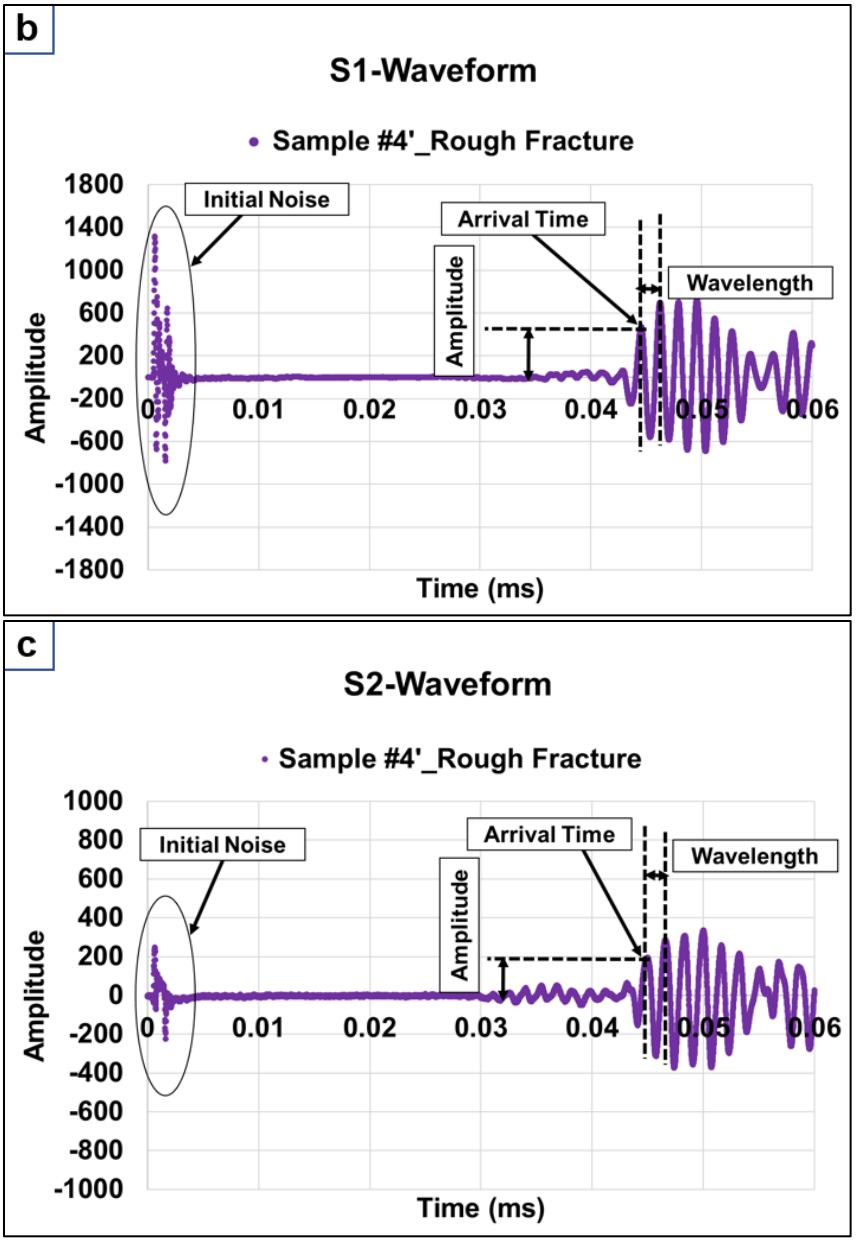

Figure 38: Identification of arrival time, amplitude, and wavelength for each of: (a) P-waveform, (b) S1-waveform, and (c) S2-waveform for Sample #4' at S_a, P_c, and T values of 7000 psi, 3000 psi, and 21 °C, respectively.

Table 14: Testing conditions for Caney and Eagle Ford shale samples.

Sample #	Rock Type	Rock Condition	Characteristic	T (°C)	S_a (psi)	P_c (psi)
1’	Caney	Fractured	Strike_0°	21	3000	2950
				21	5000	1000
				21	7000	3000
				50	3000	2950
				50	5000	1000
				50	7000	3000
				95	3000	2950
				95	5000	1000
				95	7000	3000
			Strike_30°	21	3000	2950
				21	5000	1000
				21	7000	3000
			Strike_45°	21	3000	2950
				21	5000	1000
				21	7000	3000
1”	Caney	Fractured	Density_2 Fractures	21	3000	2950
				21	5000	1000
				21	7000	3000
1	Caney	Intact	-	21	5000	1000
				21	7000	3000
				95	5000	1000
				95	7000	3000
2’	Caney	Fractured	Dip 80°	21	3000	2950
				21	5000	1000
				21	7000	3000
2	Caney	Intact	-	21	5000	1000
				21	7000	3000
				95	5000	1000
				95	7000	3000
3’	Eagle Ford	Fractured	Smooth	21	3000	2950
				21	5000	1000
				21	7000	3000
4’	Eagle Ford	Fractured	Rough	21	3000	2950
				21	5000	1000
				21	7000	3000
4”	Eagle Ford	Fractured	Rough w. Larger Volume	21	3000	2950
				21	5000	1000
				21	7000	3000
5’	Eagle Ford	Fractured	Dip 75°	21	3000	2950
				21	5000	1000
				21	7000	3000

4.2.4 Supervised Machine Learning Models

Two supervised machine learning models, extreme gradient boosting (XGBoost) and K-Nearest Neighbors (KNN), were developed to predict P, S1, and S2 waveforms based on travel time (ms), *L* (in), *D* (in), *RHOB* (g/cc), fracture volume (in³), S_a (psi), P_c (psi), *T* (°C), fracture strike (°), fracture dip (°), number of fractures, rock type (Caney shale or Eagle Ford shale), and rock condition (intact or fractured). The portion of the waveform corresponding to the travel time from 0 ms to 0.01 ms was excluded from the training to eliminate initial noise (Figure 39), focusing only on the 0.01 ms to 0.06 ms interval with a total of 6,251 timesteps for each waveform. The dataset was split, with 80% used for training and 20% for testing. A 10-fold cross-validation was performed on the training set to fine-tune the hyperparameters, selecting those that minimized the cross-validation error (Bishop, 2006). Finally, the models were trained using the optimal hyperparameters, and their performance was assessed using the coefficient of determination (R^2). Appendix C includes a detailed description of each of the two models.

4.3 Results

4.3.1 Acoustic Measurements for Caney Shale

Acoustic measurements were conducted on two Caney shale samples under various stress and temperature conditions, with different fracture characteristics (Table 14), to assess their impact on the estimated P, S1, and S2 velocities, along with SWS, amplitude, and wavelength, as previously described (Figure 38). First, measurements on the intact samples (#1 and #2) were conducted at temperatures of 21 °C and 95 °C. Then, fractured Sample #1’ was tested at temperatures 21 °C, 50 °C, and 95 °C with a fracture strike angle ranging from 0° to 45°. Samples #1’ and 2’ were further evaluated on the impact of dip angle, 90°

versus 80°. Lastly, fracture volume was assessed using Samples #1' and #1" (representing single and two fractures).

4.3.1.1 Intact Sample Measurements

Intact Sample #1 (with a bulk density of 2.6 g/cc) generally exhibited higher V_p, V_{S1}, and V_{S2} velocities than intact Sample #2 (bulk density of 2.45 g/cc) under similar conditions, indicating that higher bulk density contributes to faster wave propagation. This trend was consistent across all tested conditions, with Sample #1 maintaining higher wave velocities even at elevated temperatures and stress levels (Figure 39.a). The reduction in SWS values was minimal in both samples at 21°C. However, a significant drop was observed at 95 °C, with SWS decreasing from 0.712% to 0.501% in Samples #1 and from 1.01% to 0.917% in Sample #2 as S_a increased from 5,000 psi to 7,000 psi. This trend highlights the significant effect of temperature on wave behavior (Figure 39.a).

The amplitude from Sample #1 measurements was generally higher than Sample #2, especially for the P-wave. The increase in S_a from 5,000 to 7,000 psi yielded an increase in P-wave amplitude from 324 to 369 mV and from 303 to 347 mV for Samples #1 and #2, respectively, at 21 °C (Figure 39.b). The increase in temperature to 95 °C yielded a decrease in amplitudes for P, S1, and S2 waves for both samples. The wavelength measurements showed minor changes across the different conditions, as shown in Figure 39.c.

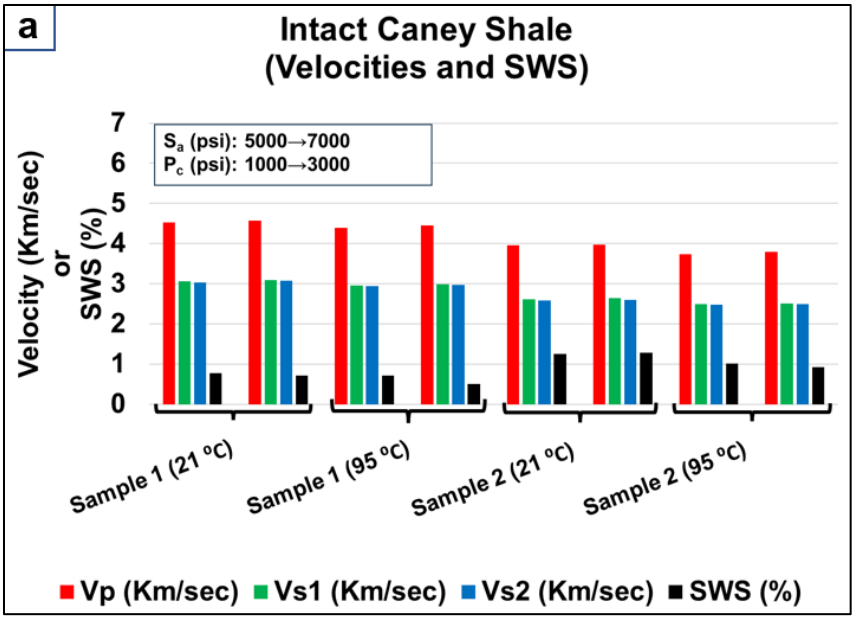
a
Intact Caney Shale
(Velocities and SWS)
Velocity (Km/sec)
or
SWS (%)
S_a (psi): 5000→7000
P_c (psi): 1000→3000
0
1
2
3
4
5
6
7
Sample 1 (21 °C)
Sample 1 (95 °C)
Sample 2 (21 °C)
Sample 2 (95 °C)
Vp (Km/sec)
Vs1 (Km/sec)
Vs2 (Km/sec)
SWS (%)

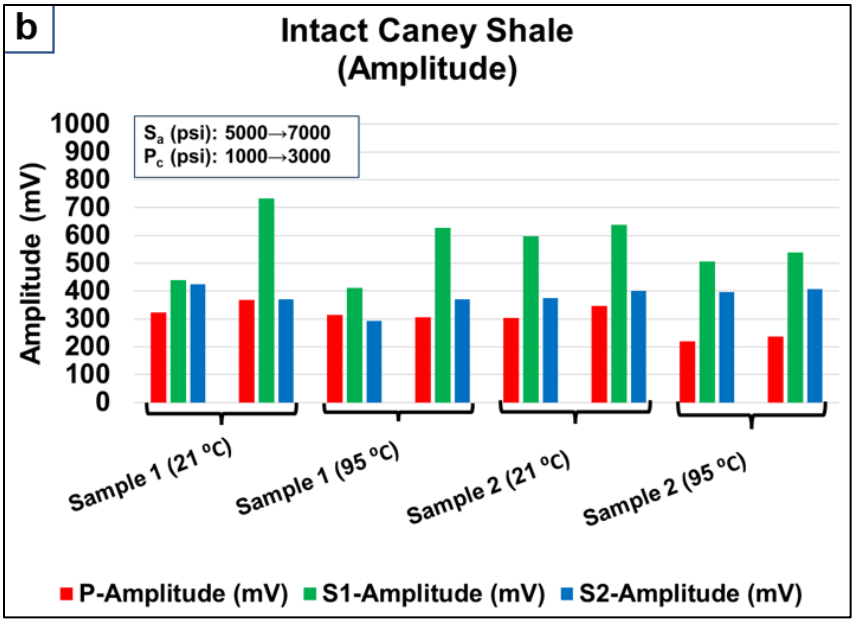
b
Intact Caney Shale
(Amplitude)
Amplitude (mV)
S_a (psi): 5000→7000
P_c (psi): 1000→3000
0
100
200
300
400
500
600
700
800
900
1000
Sample 1 (21 °C)
Sample 1 (95 °C)
Sample 2 (21 °C)
Sample 2 (95 °C)
P-Amplitude (mV)
S1-Amplitude (mV)
S2-Amplitude (mV)

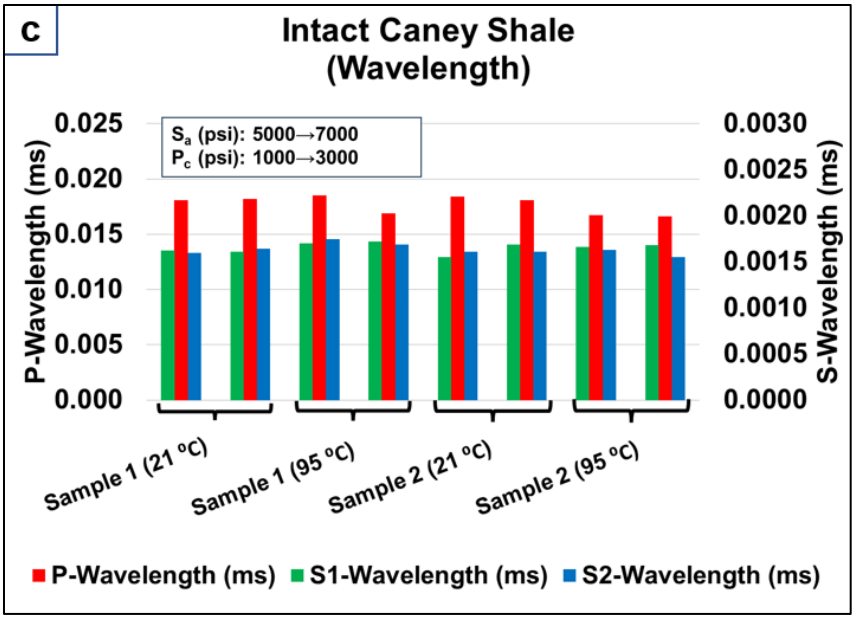

Figure 39: Acoustic measurements for the intact Caney shale samples (samples 1 and 2) at temperature values of 21 °C and 95 °C: (a) P, S1, and S2 velocities and shear wave splitting (SWS), (b) P, S1, S2 wave amplitude, and (c) P, S1, S2 wavelength. Each bracketed group contains sets of columns that correspond to the highlighted stress conditions (S_a and P_c), with arrows indicating the respective conditions for each set.

4.3.1.2 Effect of Temperature

The effect of temperature on the acoustic properties of the fractured Caney shale Sample 1' was examined at 21 °C, 50 °C, and 95 °C under one nearly isotropic stress condition (S_a 3000 psi, P_c 2950 psi) and two high anisotropic stress conditions (first condition: S_a of 5000 psi, P_c of 1000 psi; second condition: S_a of 7000 psi, P_c of 3000 psi). As the temperature increased from 21 °C to 95 °C, V_P, V_{S1}, and V_{S2} generally decreased across all stress conditions. For example, at high anisotropy, V_P dropped from 4.59 to 4.45 Km/sec, V_{S1} from 3.13 to 3.02 Km/sec, and V_{S2} from 3.04 to 2.93 Km/sec (Figure 40.a). This reduction in wave velocities with increasing temperature suggests a softening effect on the rock, potentially due to thermal expansion and microfracture development (Guo et al., 2023). SWS exhibited a similar trend of inverse correlation with temperature as SWS dropped from 3.04% at 21 °C to 2.81% at 95 °C at high anisotropic conditions (Figure

40.a).

Amplitude increased with temperature, especially under high anisotropic conditions, where S1 amplitude showed more significant growth, reaching 879 mV at 95 °C from 684 mV at 21 °C (Figure 40.b). On the other hand, temperature change showed no clear impact on wavelengths (Figure 40.c).

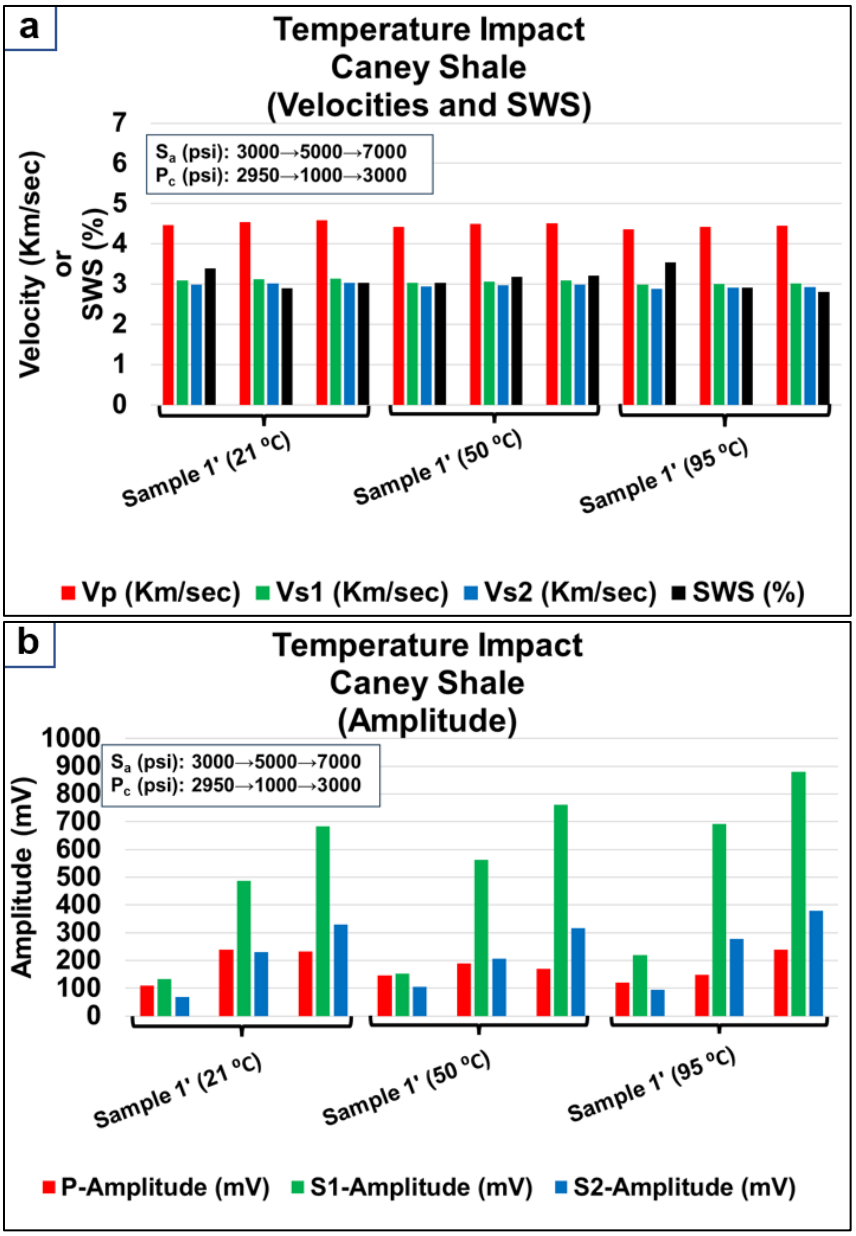

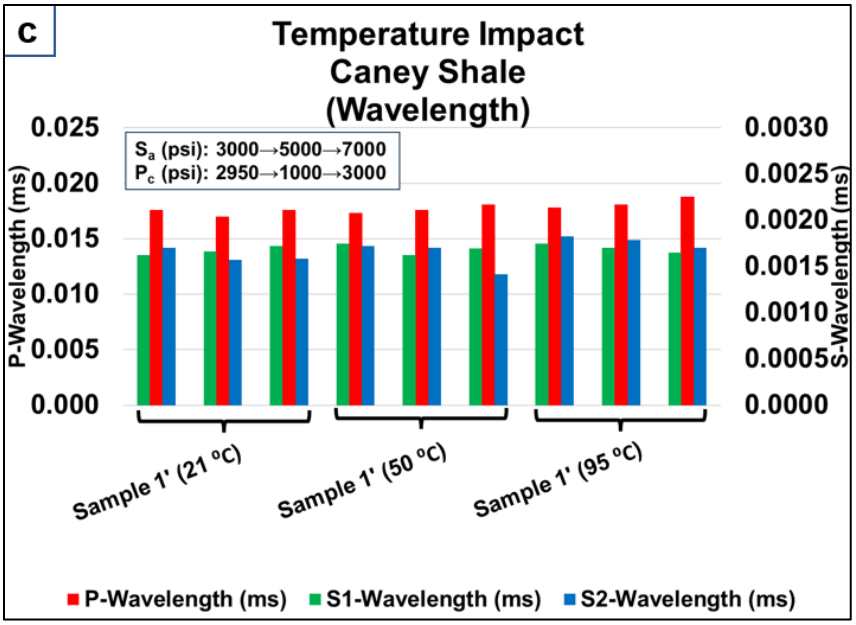

Figure 40: Acoustic measurements for the fractured Caney shale sample (Sample #1') at temperature values of 21 °C, 50 °C, and 95 °C: (a) P, S1, and S2 velocities and shear wave splitting (SWS), (b) P, S1, S2 wave amplitude, and (c) P, S1, S2 wavelength. Each bracketed group contains sets of columns that correspond to the highlighted stress conditions (S_a and P_c), with arrows indicating the respective conditions for each set.

4.3.1.3 Effect of Strike Angle

Caney Sample #1' was utilized to assess the impact of fracture strike on the acoustic properties at 21 °C. Under low stress anisotropy, V_P and V_S values showed minimal change with strike, remaining around 4.47–4.48 Km/s for V_P and 2.98–3.01 Km/s for V_S. However, SWS was significantly affected, decreasing from 3.39% at 0° to 1.80% at 45° (Figure 41.a). These observations align with our previous experimental findings (Kholy and Lee, 2023) on Hydrostone and Eagle Ford samples, which confirmed that the highest and the lowest SWS values occurred at strike angles of 0° and 45°, respectively. This effect likely results from the reorientation of the two transmitted shear waves, causing the fast and slow waves to polarize along and perpendicular to the fracture plane, leading to increased wave attenuation, as discussed by Martin and Davis (1987). This trend persisted under high stress anisotropy, with SWS values decreasing from 2.89% at 0° to as low as 1.54% at 45° (Figure

41.a).

Amplitude variations were notable across different fracture strikes, particularly for S1. Under low stress anisotropy, S1 amplitude increased from 134 mV at 0° to 549 mV at 45°. For the high stress anisotropy case, S1 amplitude rose from 492 mV at 0° to 1365 mV at 45° (Figure 41.b). In addition, increased axial stress led to higher P, S1, and S2 amplitudes, presumably due to the gradual closure of microcracks (Figure 41.b). On the other hand, the strike impact on wavelengths values for P, S1, and S2 waves was negligible (Figure 41.c).

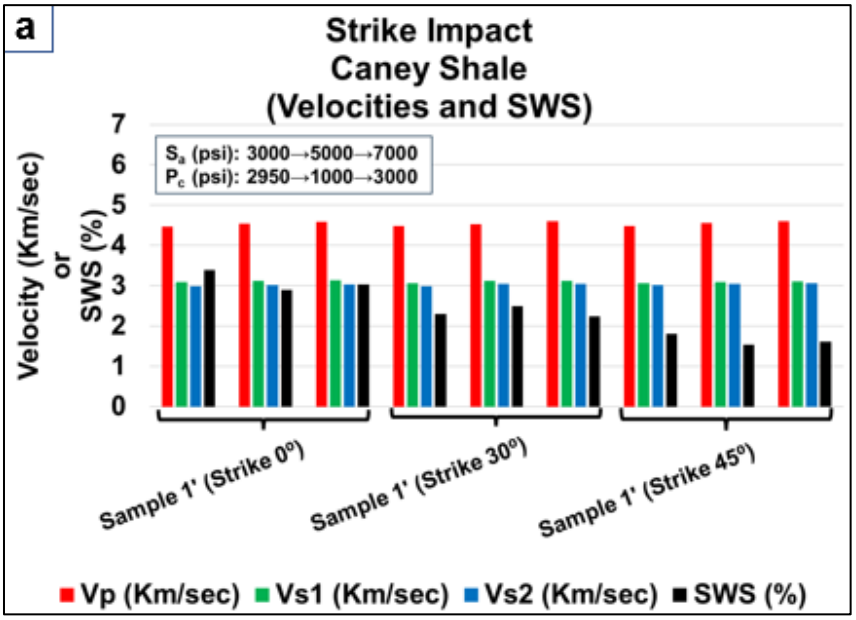

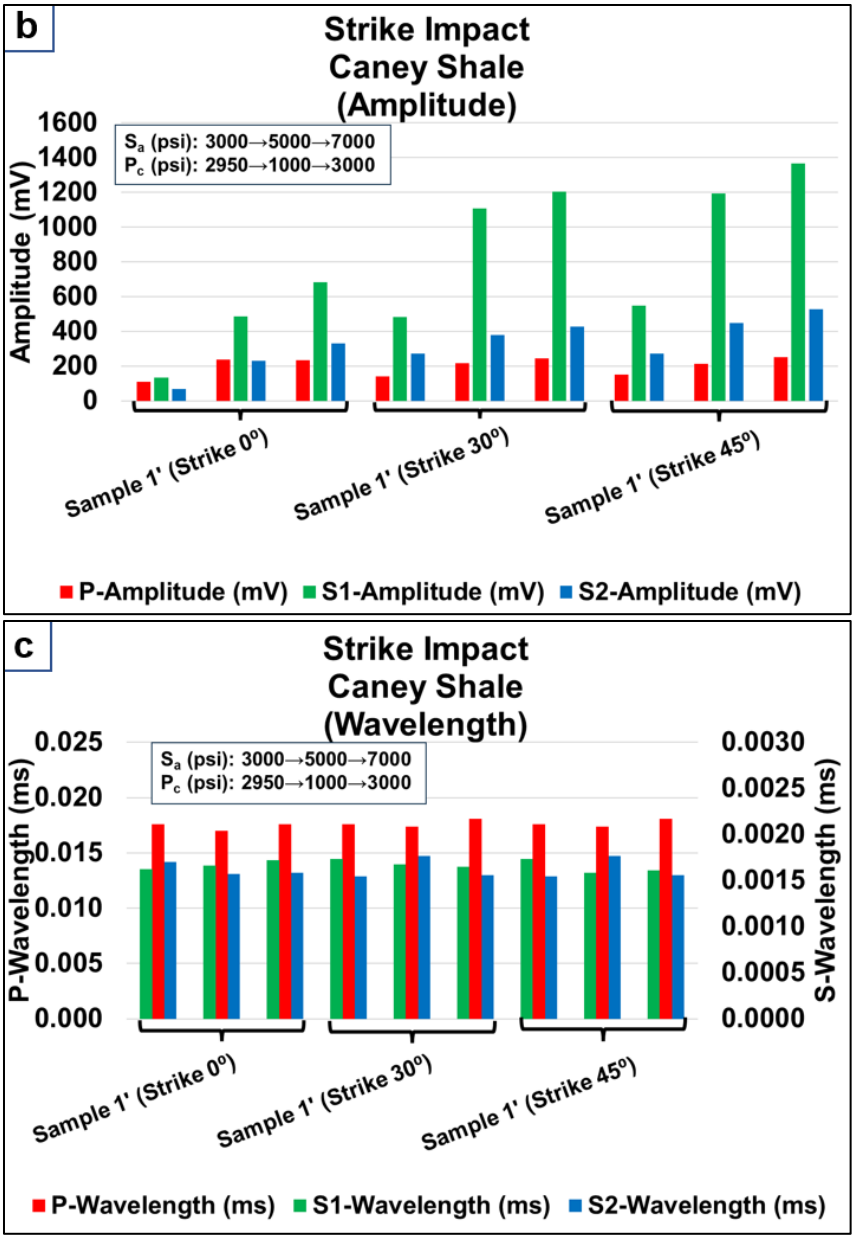

Figure 41: Acoustic measurements for the fractured Caney shale sample (Sample #1') to evaluate strike impact at temperature of 21 °C: (a) P, S1, and S2 velocities and shear wave splitting (SWS), (b) P, S1, S2 wave amplitude, and (c) P, S1, S2 wavelength. Each bracketed group contains sets of columns that correspond to the highlighted stress conditions (S_a and P_c), with arrows indicating the respective conditions for each set.

4.3.1.4 Effect of Dip Angle

Comparing the 90° dip for Caney Sample #1' and the 80° dip for Caney Sample #2' at

21 °C reveals distinct differences in SWS. The SWS for Caney Sample #1' was lower than

for Sample #2', possibly due to the higher shear tendency in the two halves of Sample #2' with an 80° dip under high anisotropic stress condition, likely widening fracture apertures and elevating SWS (Li and Peng, 2017). Under high stress anisotropy, SWS was 4.24% for the 80° dip compared to 3% for the 90° dip (Figure 42.a). At a 90° dip and low stress anisotropy, values were higher (4.47, 3.09, and 2.98 Km/s, respectively) compared to the 80° dip, where V_P dropped to 3.80 Km/s, and V_{S1} and V_{S2} were around 2.41 and 2.31 Km/s. The velocities were significantly lower for all three waveforms of Sample #2'; however, further investigation is needed to understand if it is due to the dip angle since Sample #2' has a lower bulk density than Sample #1'. Similarly, the higher P-wave amplitude values for Sample #1' are possibly due to its higher density (Figure 42.b). In contrast, wavelength variations between the two samples were unclear (Figure 42.c).

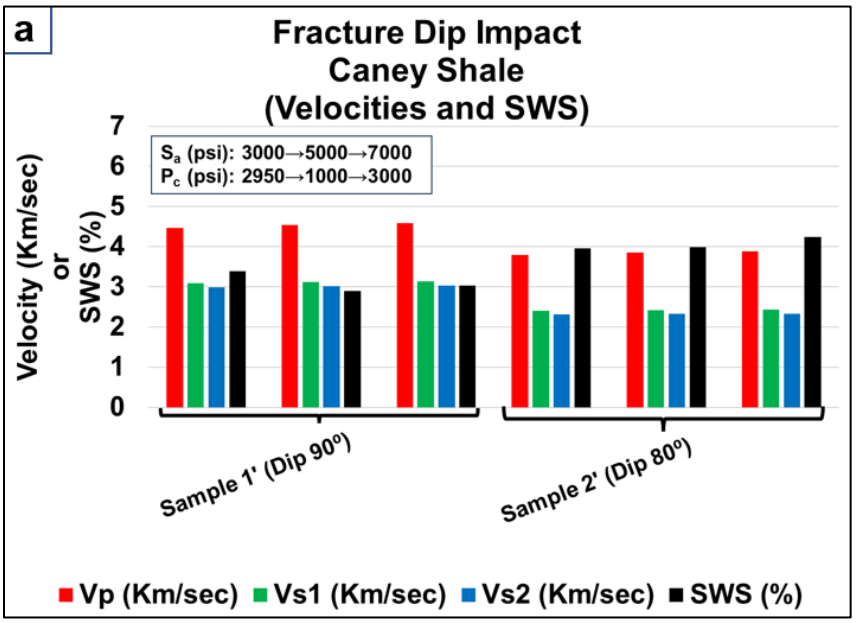

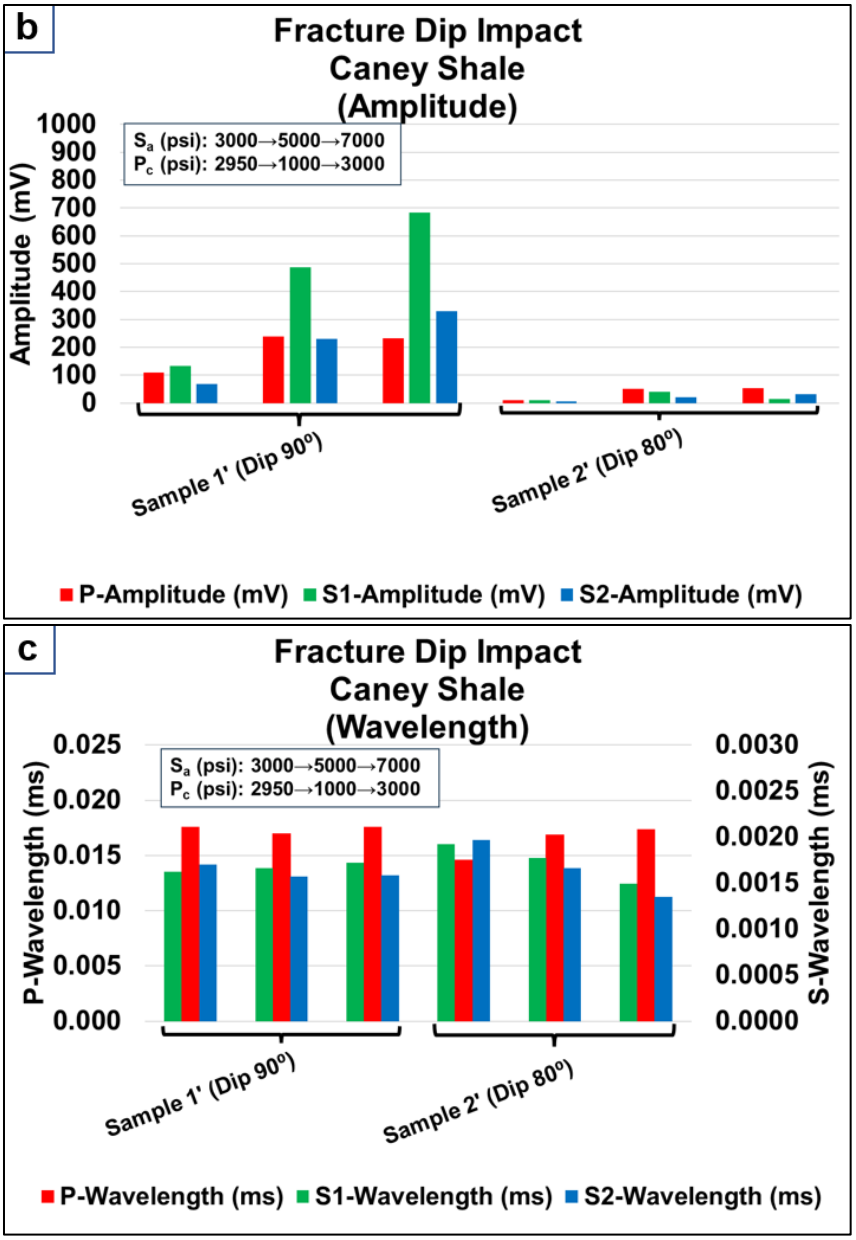

Figure 42: Acoustic measurements for the fractured Caney shale samples (samples 1' and 2') to evaluate dip impact at temperature of 21 °C: (a) P, S1, and S2 velocities and shear wave splitting (SWS), (b) P, S1, S2 wave amplitude, and (c) P, S1, S2 wavelength. Each bracketed group contains sets of columns that correspond to the highlighted stress conditions (S_a and P_c), with arrows indicating the respective conditions for each set.

4.3.1.5 Effect of Fracture Volume

For the single-fractured Caney Sample #1' compared to the double-fractured Caney Sample #1" at 21°C, an increase in fracture volume led to higher SWS values, especially

under high stress anisotropy conditions (Figure 43.a). While V_P, V_{S1}, and V_{S2} showed relatively minor changes with increased fracture volume, SWS rose significantly from 3.39% (single-fractured, low stress anisotropy) to 4.57% (double-fractured, high stress anisotropy). This suggests that additional fractures and increased fracture volume enhance shear wave splitting (Hudson, 1981).

Amplitude values were generally lower for the double-fractured sample, especially under low stress anisotropy conditions, where P, S1, and S2 amplitudes were as low as 59, 21, and 32 mV, respectively, compared to 109, 134, and 69 mV for the single-fractured sample. As stress anisotropy increased, amplitude values for double-fractured scenarios rose but remained lower than the corresponding single-fractured cases (Figure 43.b). On the other hand, the fracture volume impact on wavelengths was inclusive for P, S1, and S2 (Figure 43.c).

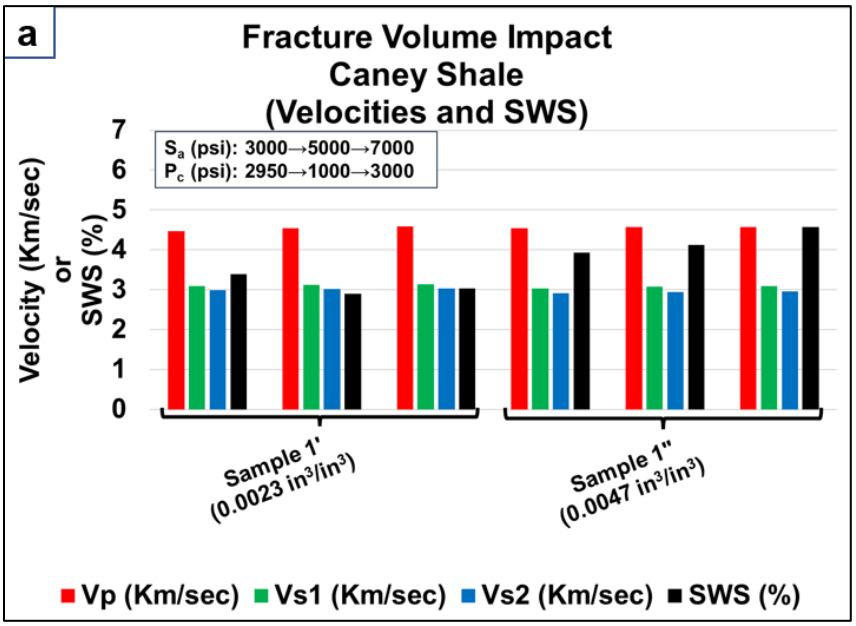

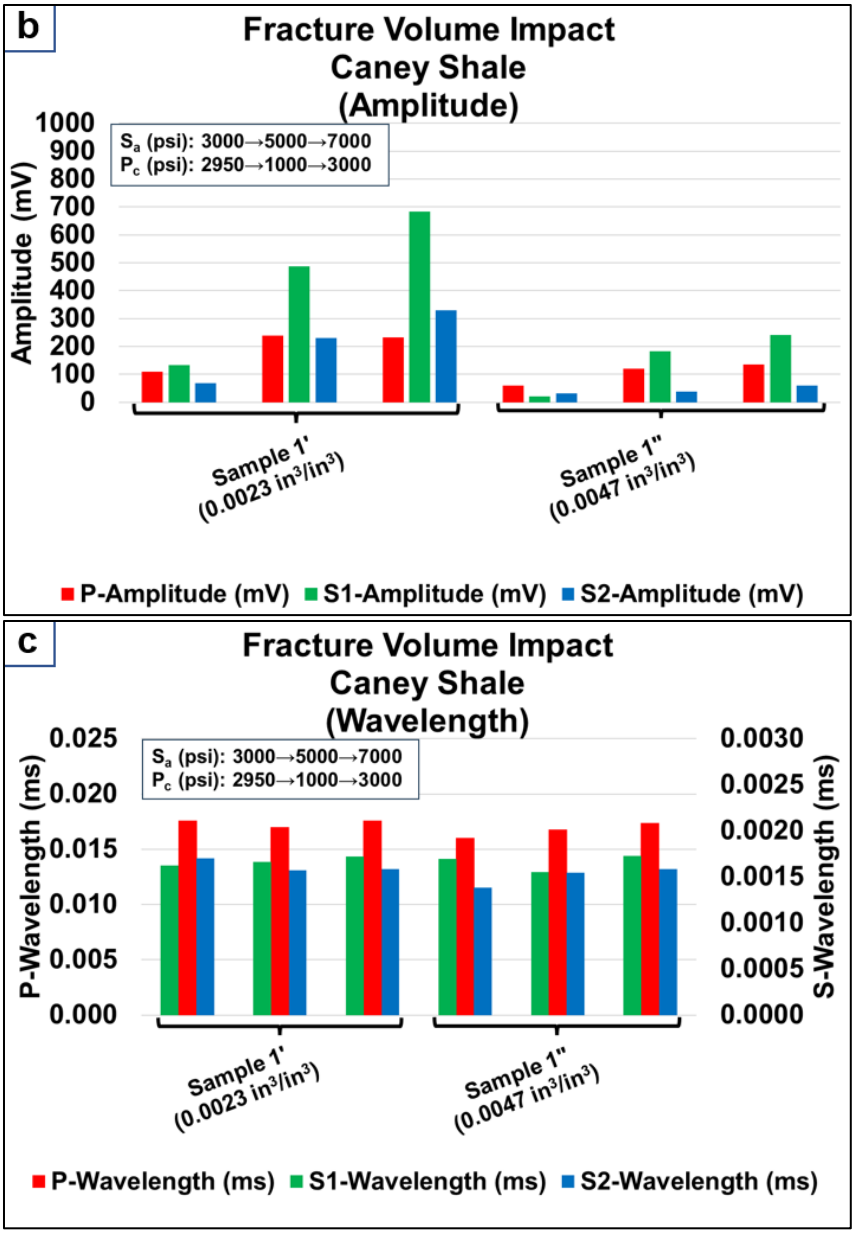

Figure 43: Acoustic measurements for the fractured Caney shale to evaluate fracture volume impact using single-fractured (Sample #1') and double-fractured (Sample 1") at temperature of 21 °C: (a) P, S1, and S2 velocities and shear wave splitting (SWS), (b) P, S1, S2 wave amplitude, and (c) P, S1, S2 wavelength. Each bracketed group contains sets of columns that correspond to the highlighted stress conditions (S_a and P_c), with arrows indicating the respective conditions for each set.

4.3.2 Acoustic Measurements for Eagle Ford Shale

Three Eagle Ford shale samples (#3', #4', and #4") were utilized to evaluate additional fracture characteristics, including fracture volume and dip of 75° at 21 °C, as well as the

impact of shale type on acoustic wave characteristics under same stress conditions applied to the Caney shale samples.

4.3.2.1 Effect of Dip Angle

Varying the fracture dip from 90° (Sample #3') to 75° (Sample #5') at 21 °C under both low and high stress anisotropic conditions revealed that SWS increased significantly with decreasing dip angle, similar to observations for Caney shale samples (Figure 44.a). At a 90° dip and low stress anisotropy, SWS was only 0.51%, while at a 75° dip under the same conditions, it rose to 1.99%, confirming that shallower fracture dips promote greater shear wave splitting. The dip angle impact on individual velocities (Figure 44.a) and amplitude values (Figure 44.b) for P, S1, and S2 was unclear, and the higher values for Sample #5' are likely due to its higher bulk density of 2.57 g/cc compared to Sample #3' value of 2.2 g/cc. Wavelengths of P, S1, and S2 waves were generally similar between the 75° and 90° dips (Figure 44.c).

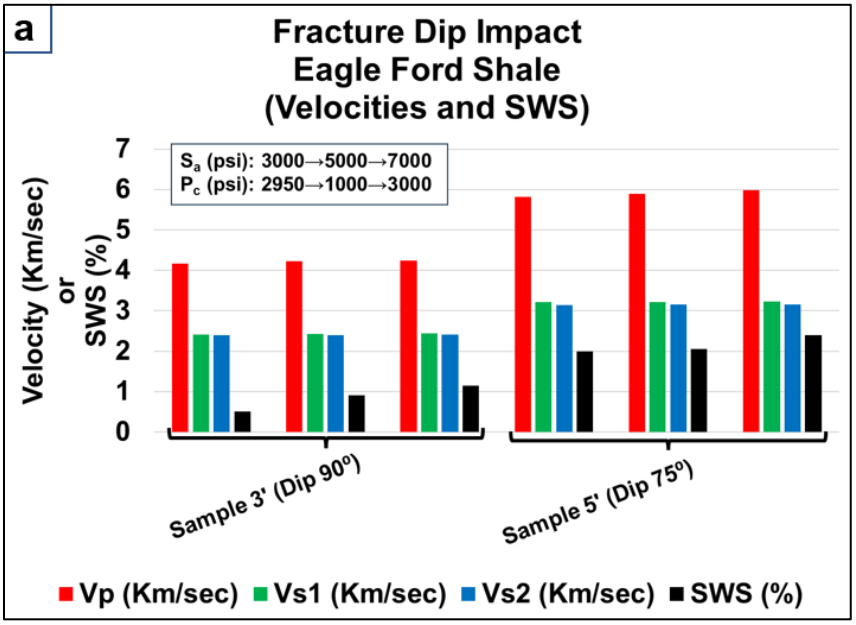

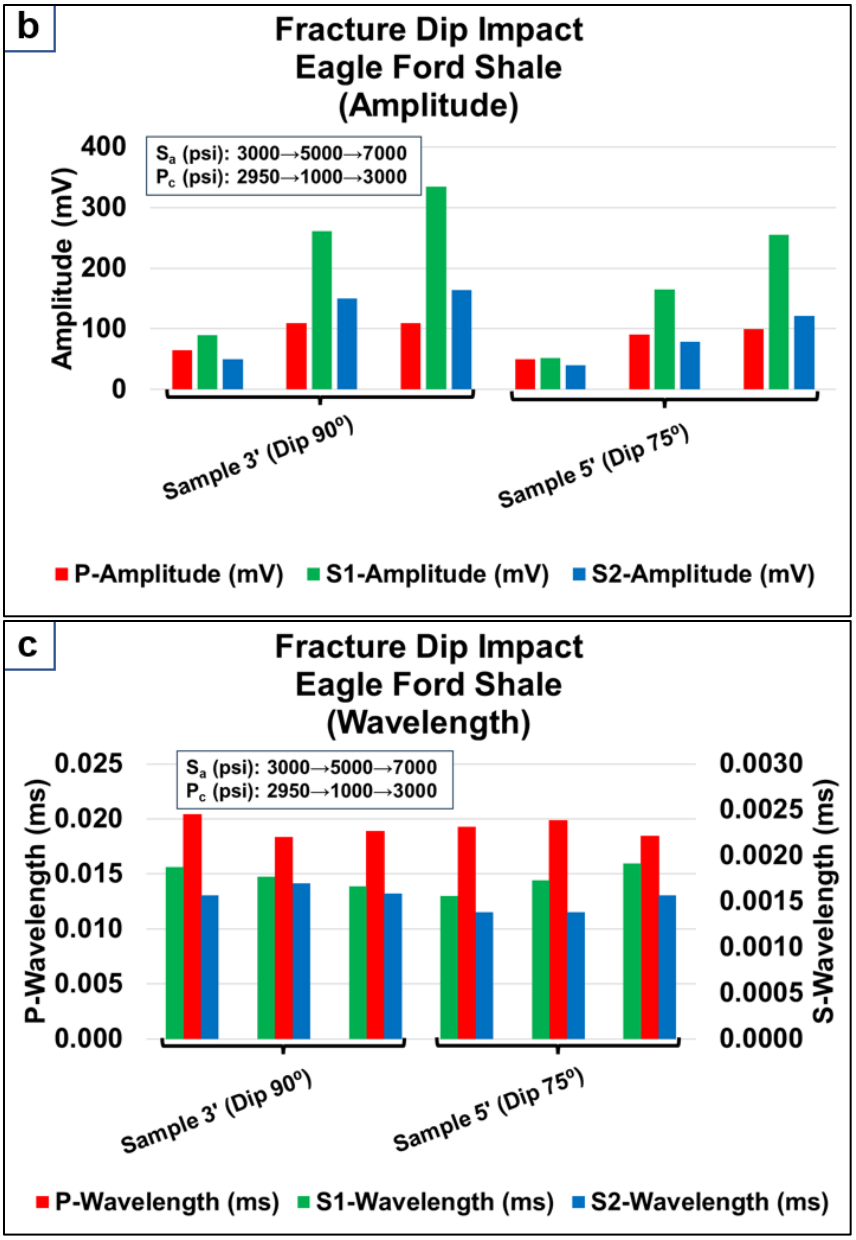

Figure 44: Acoustic measurements for the fractured Eagle Ford shale samples (samples #3' and #5') to evaluate dip impact at temperature of 21 °C: (a) P, S1, and S2 velocities and shear wave splitting (SWS), (b) P, S1, S2 wave amplitude, and (c) P, S1, S2 wavelength. Each bracketed group contains sets of columns that correspond to the highlighted stress conditions (S_a and P_c), with arrows indicating the respective conditions for each set.

4.3.2.2 Effect of Fracture Volume

The results indicate that fracture volume significantly impacts the acoustic wave velocities and shear wave splitting (SWS) in Eagle Ford shale. For the smooth fracture (Sample #3'),

V_P, V_{S1}, V_{S2}, and SWS values were generally lower compared to the rough fracture (Sample #4') and the rough fracture with larger volume (Sample #4"). For example, SWS was 0.51% for the smooth fracture under low stress anisotropy, while it increased to 1.25% for the rough fracture and 1.53% for the rough fracture with a larger volume under the same stress conditions (Figure 45.a).

Amplitude results indicated that larger fracture volumes corresponded to lower amplitudes in P, S1, and S2 waveforms. For example, Sample #4' with a P-wave amplitude of 175 mV showed a higher amplitude than Sample #4" (118 mV), which had a larger fracture volume. The notably lower P-wave amplitude of Sample #3' (65 mV) likely reflects its lower bulk density compared to Samples #4' and 4" (Figure 45.b). On the other hand, the impact of fracture volume on wavelength was negligible (Figure 45.c).

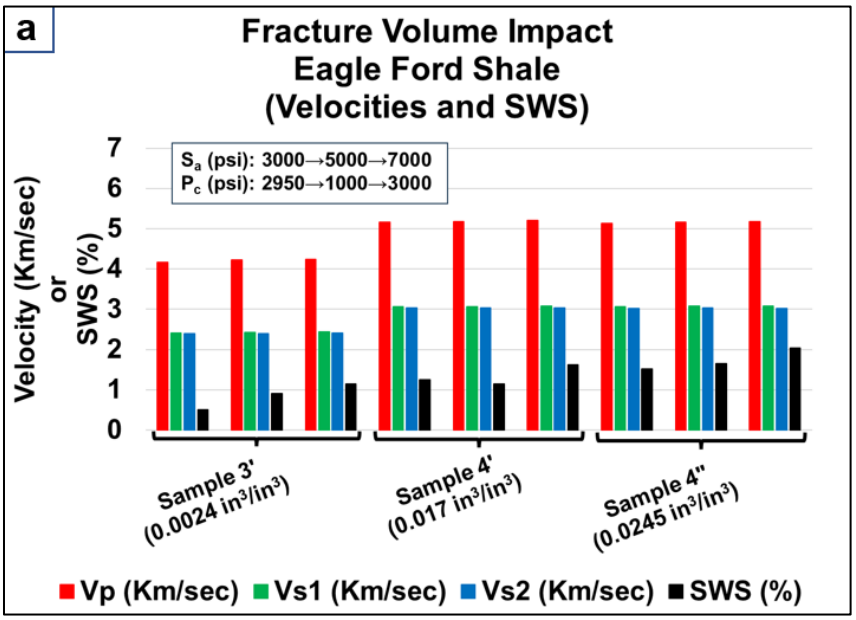

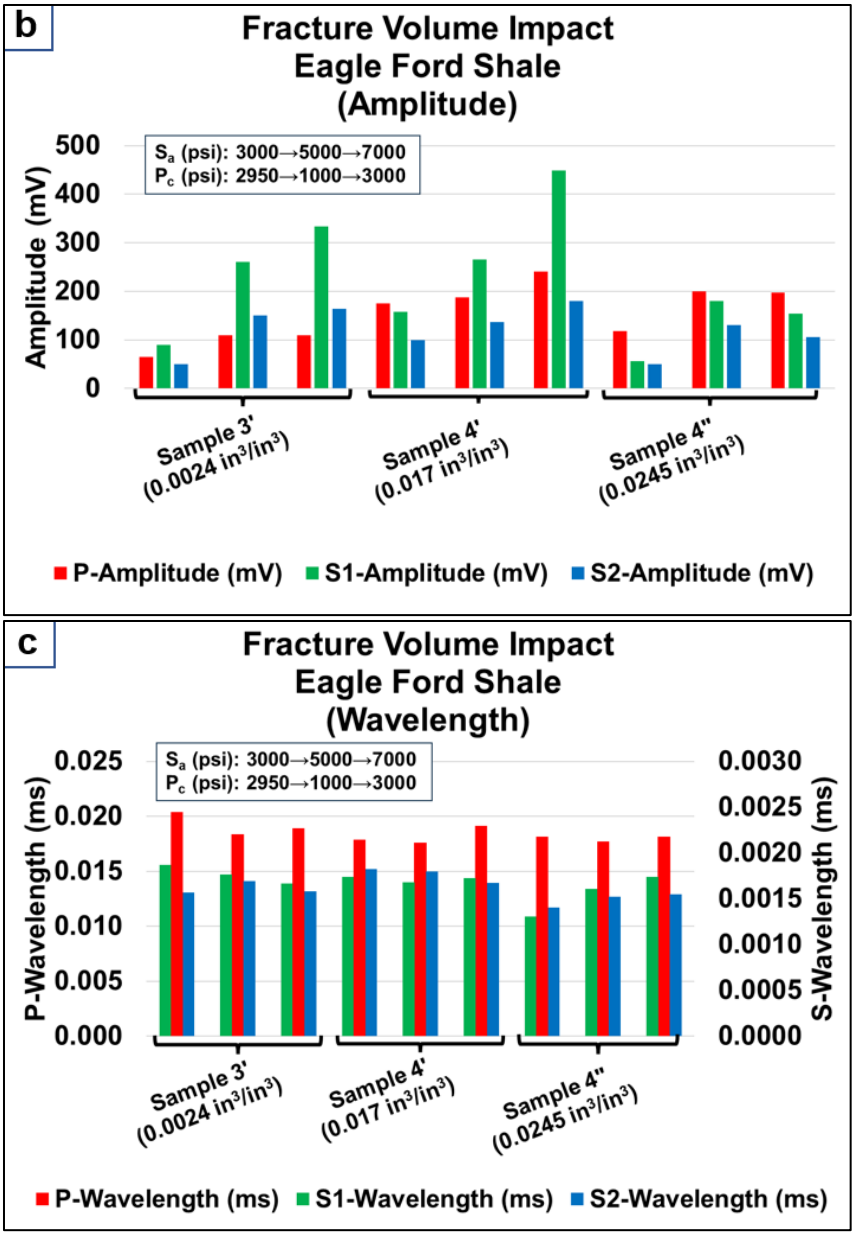

Figure 45: Acoustic measurements for the fractured Eagle Ford shale samples 3' (smooth fracture), 4' (rough fracture) and 4" (rough fracture with large aperture) to evaluate fracture volume at temperature of 21 °C: (a) P, S1, and S2 velocities and shear wave splitting (SWS), (b) P, S1, S2 wave amplitude, and (c) P, S1, S2 wavelength. Each bracketed group contains sets of columns that correspond to the highlighted stress conditions (S_a and P_c), with arrows indicating the respective conditions for each set.

Figure 46 provides a summary of the measurements discussed in this section, illustrating the effects of temperature, bulk density, and fracture characteristics on the acoustic

properties, including acoustic velocities, SWS, amplitude, and wavelength for Caney and Eagle Ford shale samples.

Evaluated Property	Velocities				Amplitude			Wavelength		
	P	S1	S2	SWS	P	S1	S2	P	S1	S2
Temperature	↓	↓	↓	↓	↓	↑	↑	-	-	-
Bulk Density	↑	↑	↑	-	↑	-	-	↓	-	↓
Fracture Strike	-	↓	-	↓	-	↑	↑	-	-	-
Fracture Dip	-	-	-	↓	-	-	-	-	-	-
Fracture Volume	↓	-	↓	↑	↓	↓	↓	-	-	-

Figure 46: Summary diagram of temperature, bulk density, fracture characteristics (strike, dip, and volume) impacts on each of acoustic properties including V_P, V_{S1}, V_{S2}, SWS, wavelength, and amplitude. The upward arrow (↑) indicates a positive correlation between the fracture characteristic and the acoustic property, while the downward arrow (↓) indicates a negative correlation, and horizontal dash (-) indicates negligible or unclear correlation. The highlighted green and red cells indicate significant positive and negative correlations, respectively.

4.3.3 Acoustic Waveforms Prediction using Supervised Machine Learning

The acoustic waveforms of P, S1, and S2 waves were recorded for 41 cases with varying fracture characteristics and temperature and stress conditions. Two supervised machine learning models—extreme gradient boosting (XGBoost) and K-Nearest Neighbors (KNN)—were trained on 38 of these cases to predict P, S1, and S2 waveforms based on travel time, sample dimensions, fracture properties, temperature, and stress conditions as described earlier. The remaining 3 cases were used later for models' validation. Although the intact samples contain no induced fractures, the fracture strike and dip angles were set to 45° and 0° to accommodate the model limitation on input parameters requirements in the current setting. These angles correspond to the lowest SWS, as intact samples exhibited

minimal SWS values (Figure 39.a) (Rial et al., 2005; Cai et al., 2022).

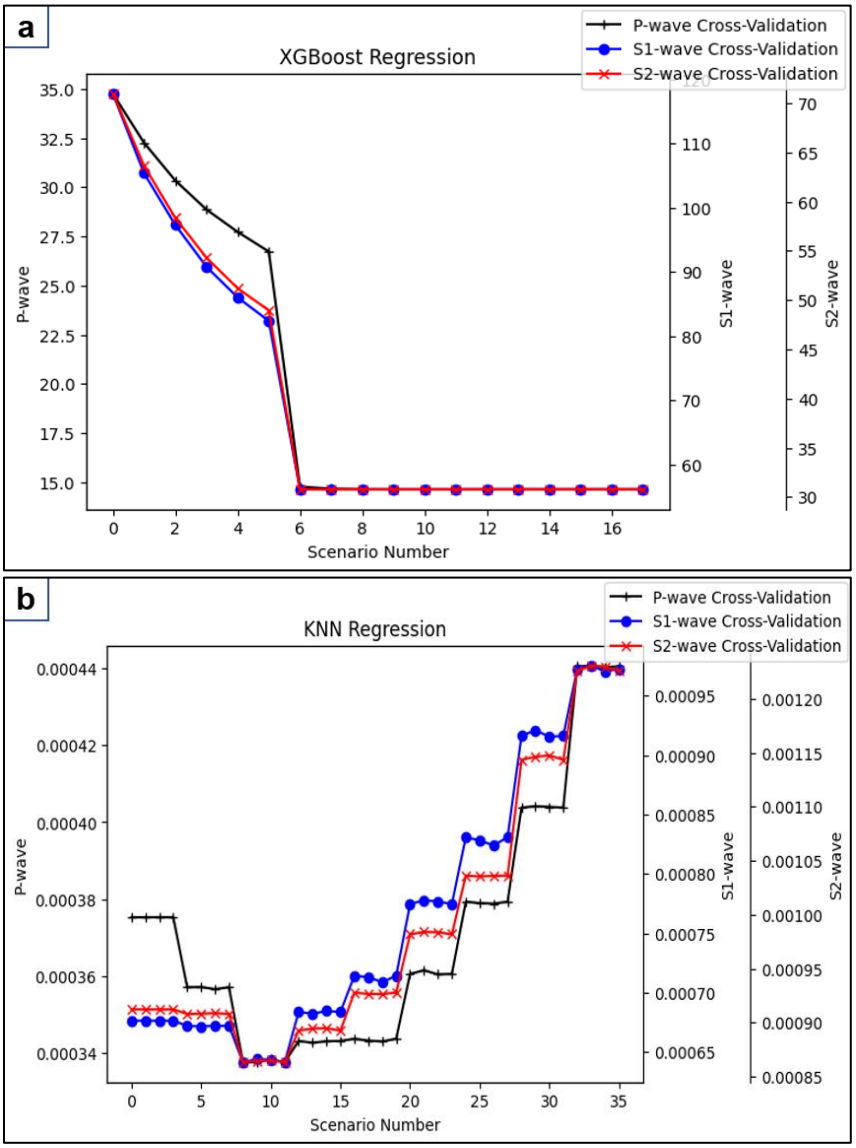

Figure 47: Cross validation results summary to select the hyperparameters that correspond to the lowest cross-validation error for P, S1, and S2 waveforms prediction using: (a) XGBoost model, and (b) KNN model.

The optimum hyperparameters for each model were selected using k-folds cross-validation, as described in Appendix C. Figure 47 presents the cross-validation results for the XGBoost (Figure 47.a) and KNN (Figure 47.b) models, with the optimum hyperparameters summarized in Table 15.

Table 15: The optimum hyperparameters for each of XGBoost and KNN models.

Wave Type	XGBoost Model	KNN Model
	max depth, # of trees, Scenario #	K-neighbors, Distance Metric, Scenario #
P	10, 800, Scenario #11	4, Euclidean, Scenario #9
S1	10, 400, Scenario #7	4, Euclidean, Scenario #9
S2	10, 500, Scenario #8	4, Euclidean, Scenario #9

Using the optimum hyperparameters (Table 15), two models were trained and tested, with error evaluated on the training and testing datasets for each of the P, S1, and S2 waveforms, as shown in the parity charts (Figure 48). The KNN model showed slightly better prediction accuracy for the training dataset (Figure 48.c) than the XGBoost model (Figure 48.a) across all P, S1, and S2 waveforms, with R-squared values exceeding 0.99. For the testing dataset, the XGBoost model demonstrated better prediction accuracy for P, S1, and S2 waveforms, with R-squared values of 0.9887, 0.9503, and 0.9462, respectively (Figure 48.b), compared to 0.9838, 0.8857, and 0.8719 for the same waveforms, respectively, from the KNN model (Figure 48.d).

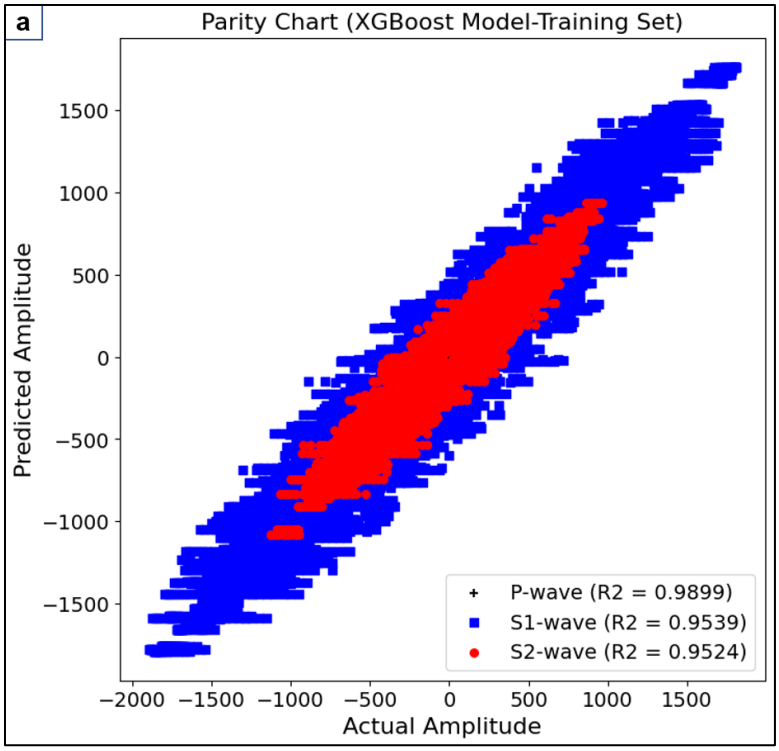
a
Parity Chart (XGBoost Model-Training Set)
Predicted Amplitude
Actual Amplitude
1500
1000
500
0
−500
−1000
−1500
−2000 −1500 −1000 −500 0 500 1000 1500
P-wave (R2 = 0.9899)
S1-wave (R2 = 0.9539)
S2-wave (R2 = 0.9524)

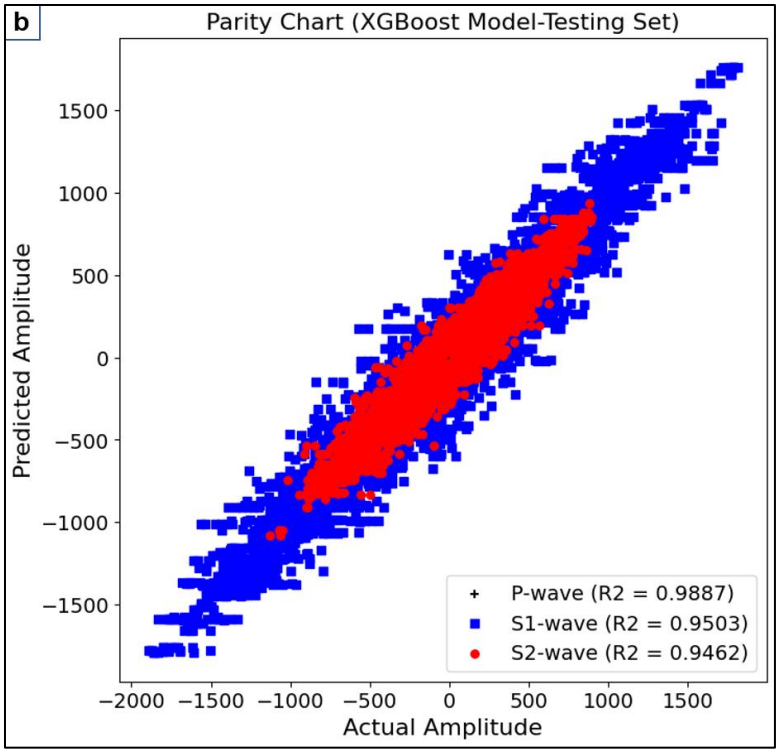
b
Parity Chart (XGBoost Model-Testing Set)
Predicted Amplitude
Actual Amplitude
1500
1000
500
0
−500
−1000
−1500
−2000 −1500 −1000 −500 0 500 1000 1500
P-wave (R2 = 0.9887)
S1-wave (R2 = 0.9503)
S2-wave (R2 = 0.9462)

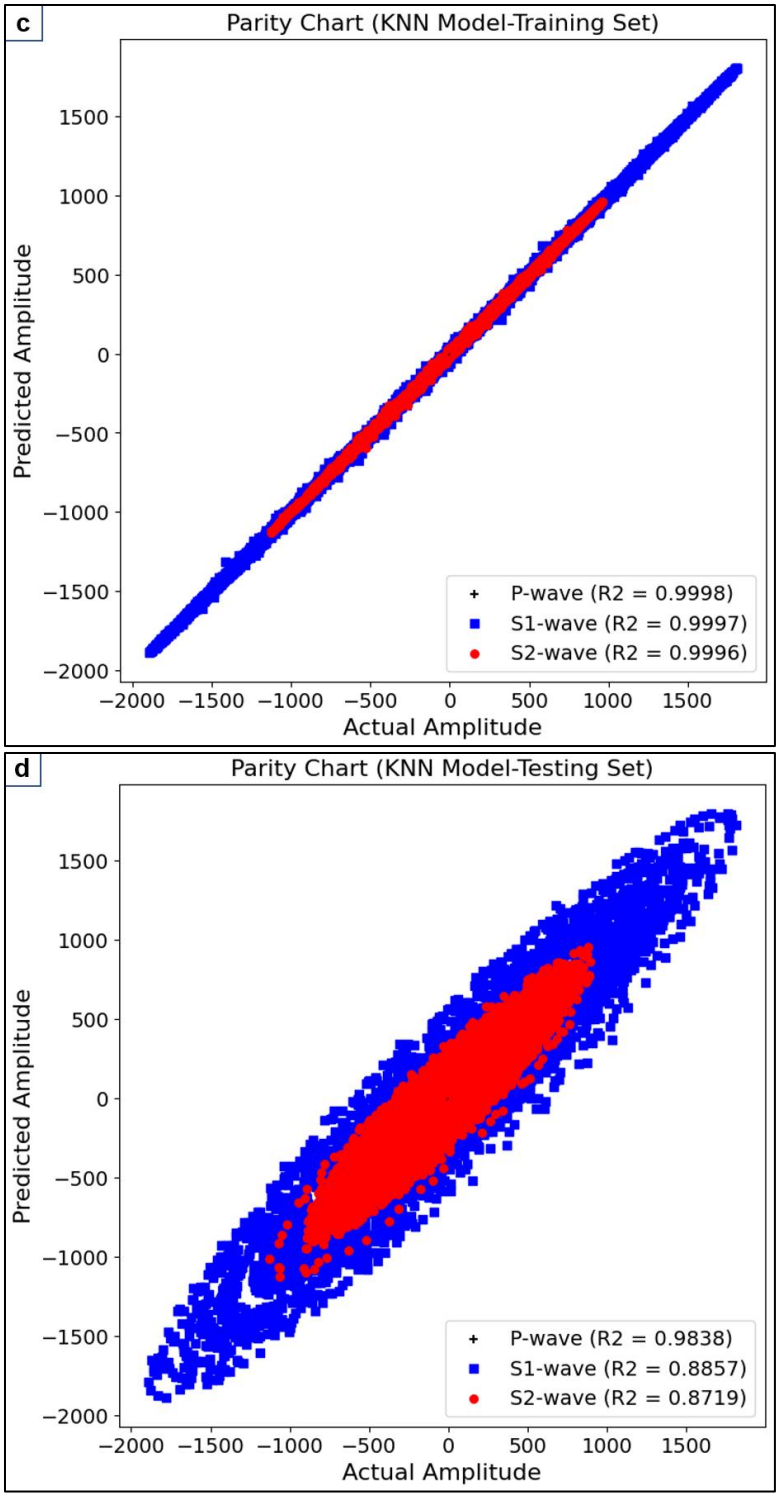

Figure 48: Parity charts to evaluate the prediction error for P-wave (black dots), S1-wave (blue dots), and S2-wave (red dots): (a) XGBoost training dataset, (b) XGBoost testing dataset, (c) KNN training dataset, and (d) KNN testing dataset.

4.3.3.1 Validation Cases

Three validation cases were utilized to evaluate the prediction accuracy of the trained models, with the testing conditions (temperature and stress) and fracture properties for each case summarized in Table 16.

Table 16: Fracture properties and testing conditions for the three validation cases.

Validation #	Sample #	T (°C)	S_a (psi)	P_c (psi)	Strike (°)	Dip (°)	# of fractures	Fracture Volume (in^3)	Normalized Volume (in^3/in^3)
1	1’	21	5000	1000	30	90	1	0.0124	0.0023
2	1’	50	7000	3000	0	90	1	0.0124	0.0023
3	4'	21	5000	1000	0	90	1	0.09	0.017

In case 1, the sample had a fracture strike of 30° and a dip of 90° at 21 °C. This validation case yielded the highest overall prediction accuracy for both models (Figure 49). The prediction accuracy was high for the P-wave (Figure 49.a), S1-wave (Figure 49.b), and S2-wave (Figure 49.c) with R-squared values close to or above 0.9 for both the XGBoost and KNN models, demonstrating that this fracture configuration allowed the models to effectively capture wave behavior, with slightly better predictions from the latter model.

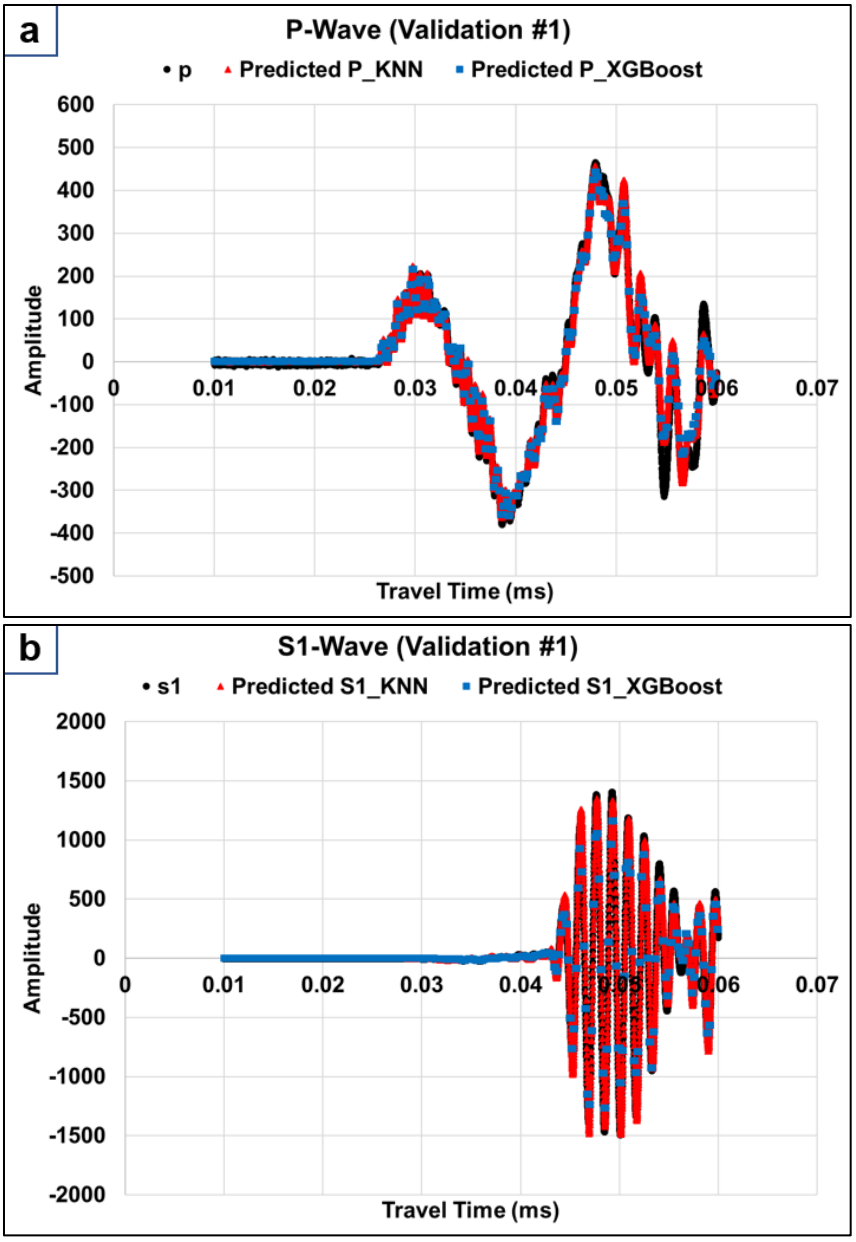
a
P-Wave (Validation #1)
• p
Predicted P_KNN
Predicted P_XGBoost
600
500
400
300
200
100
0
-100
-200
-300
-400
-500
Amplitude
0
0.01
0.02
0.03
0.04
0.05
0.06
0.07
Travel Time (ms)
b
S1-Wave (Validation #1)
• s1
Predicted S1_KNN
Predicted S1_XGBoost
2000
1500
1000
500
0
-500
-1000
-1500
-2000
Amplitude
0
0.01
0.02
0.03
0.04
0.05
0.06
0.07
Travel Time (ms)

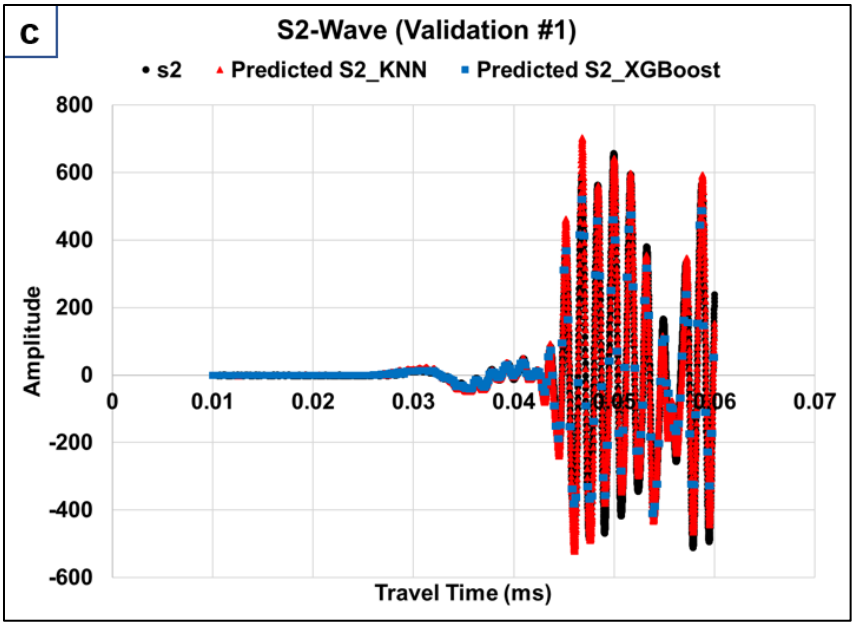

Figure 49: Prediction results comparison of validation case 1 with the actual waveforms (black dots) using XGBoost (blue dots) and KNN (red dots) for: (a) P-waveform, (b) S1-waveform, and (c) S2-waveform.

In case 2, testing conditions included a higher temperature of 50 °C, with the fracture strike and dip set to 0° and 90°, respectively. Model performance in predicting P-wave values was slightly lower compared to case 1, with R-squared values of 0.8849 for XGBoost and 0.7258 for KNN (Figure 50.a). In addition, while the predicted waveforms appeared similar to the actual waveforms (Figures 50.b and 50.c), the accuracy for S1 and S2 predictions was notably low, with R-squared values of 0.0093 and 0.1065 for XGBoost and 0.264 and 0.2974 for KNN, presumably due to a slight shift in travel time.

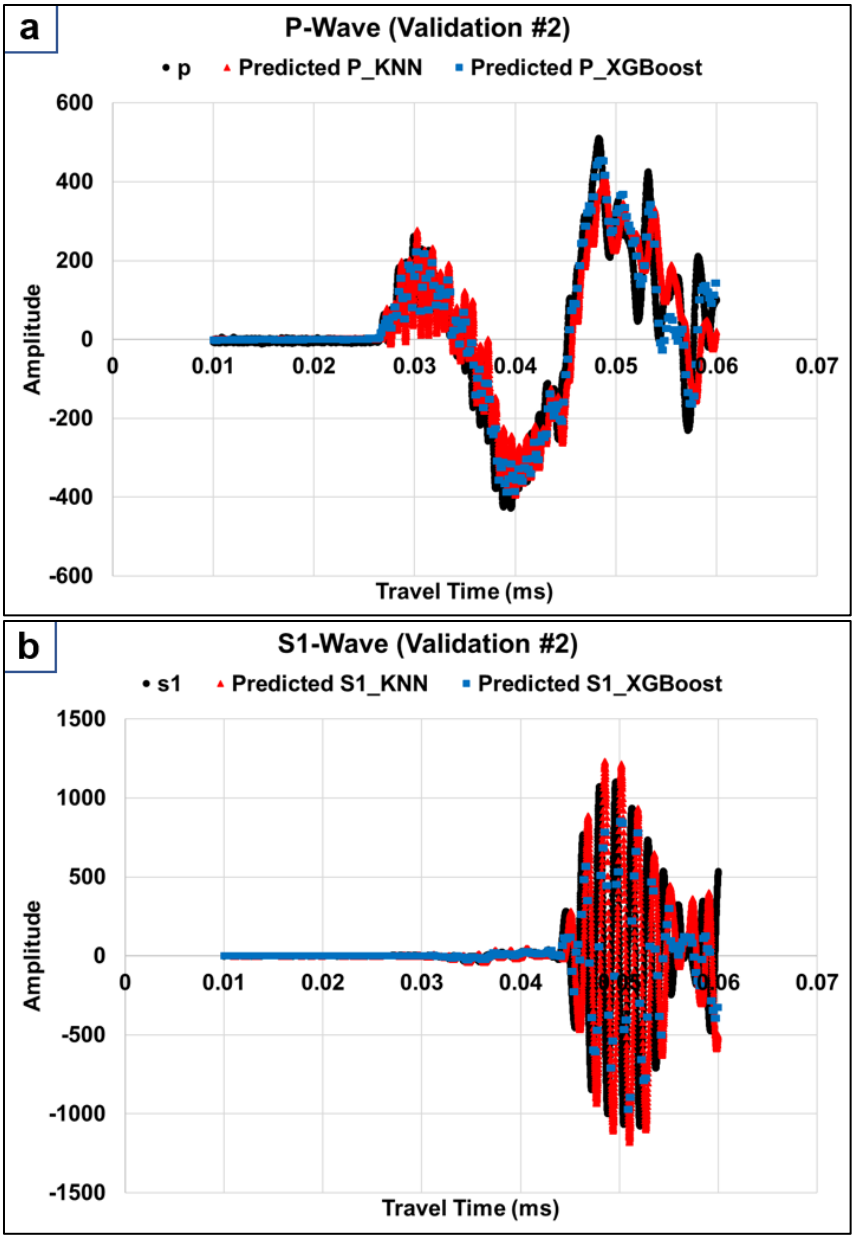
a
P-Wave (Validation #2)
• p
Predicted P_KNN
Predicted P_XGBoost
600
400
200
0
-200
-400
-600
Amplitude
0
0.01
0.02
0.03
0.04
0.05
0.06
0.07
Travel Time (ms)
b
S1-Wave (Validation #2)
• s1
Predicted S1_KNN
Predicted S1_XGBoost
1500
1000
500
0
-500
-1000
-1500
Amplitude
0
0.01
0.02
0.03
0.04
0.05
0.06
0.07
Travel Time (ms)

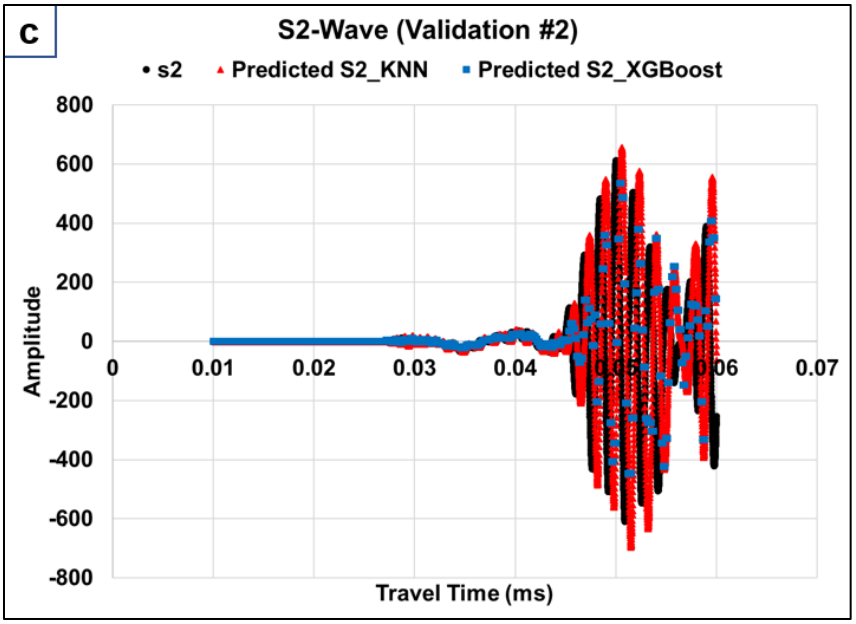

Figure 50: Prediction results comparison of validation case 2 with the actual waveforms (black dots) using XGBoost (blue dots) and KNN (red dots) for: (a) P-waveform, (b) S1-waveform, and (c) S2-waveform.

Case 3 involved a single rough-fractured Eagle Ford sample at 21 °C, with a fracture orientation characterized by a dip of 90° and strike of 0°. In this scenario, the models showed good prediction accuracy for the P-wave, with R-squared values of 0.9426 for XGBoost and 0.9452 for KNN (Figure 51.a). The S1-wave predictions exhibited moderate accuracy for the XGBoost model (R-squared of 0.6423) and high accuracy for the KNN model (R-squared of 0.9078) (Figure 51.b). For the S2-wave, the accuracy was also moderate, with XGBoost achieving an R-squared of 0.6342 and KNN reaching 0.8384 (Figure 51.c).

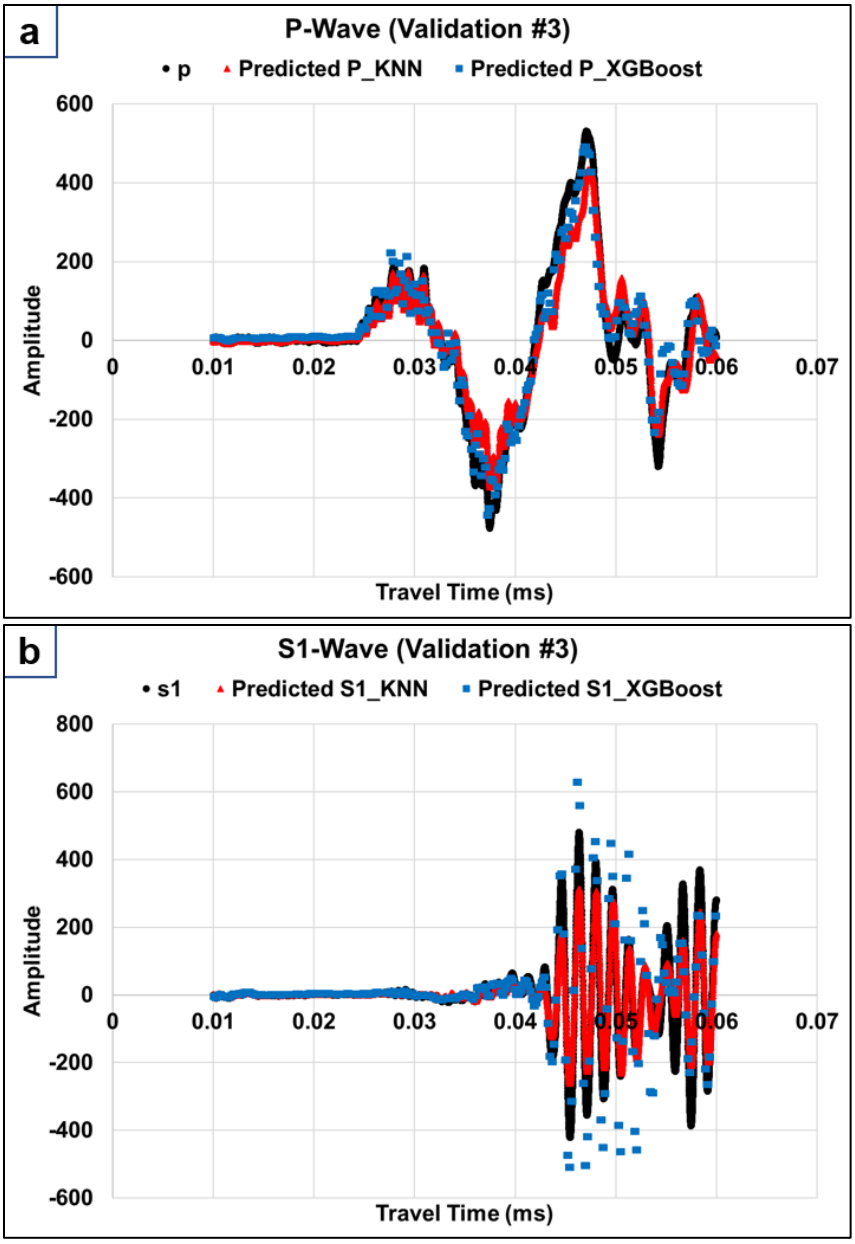
a
P-Wave (Validation #3)
• p
Predicted P_KNN
Predicted P_XGBoost
600
400
200
0
-200
-400
-600
Amplitude
0
0.01
0.02
0.03
0.04
0.05
0.06
0.07
Travel Time (ms)
b
S1-Wave (Validation #3)
• s1
Predicted S1_KNN
Predicted S1_XGBoost
800
600
400
200
0
-200
-400
-600
Amplitude
0
0.01
0.02
0.03
0.04
0.05
0.06
0.07
Travel Time (ms)

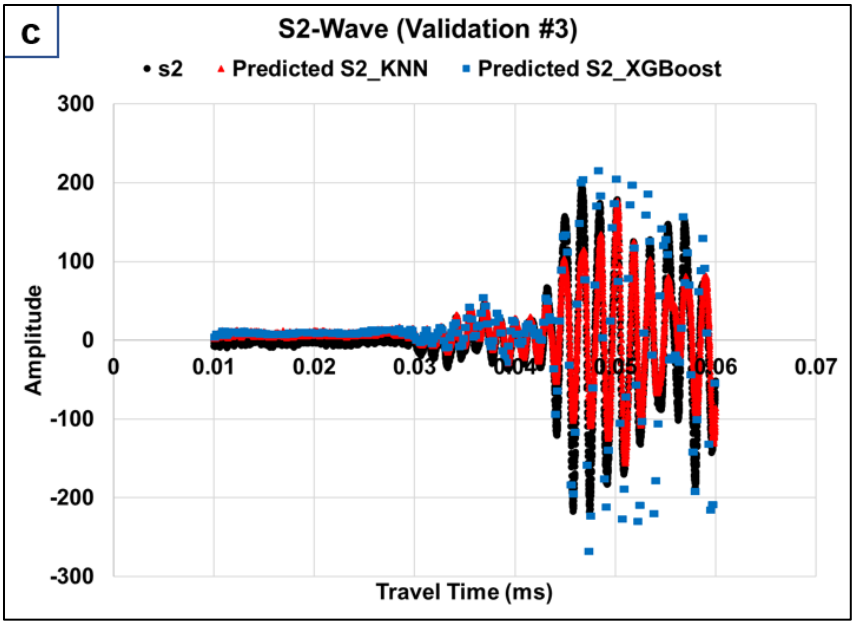

Figure 51: Prediction results comparison of validation case 3 with the actual waveforms (black dots) using XGBoost (blue dots) and KNN (red dots) for: (a) P-waveform, (b) S1-waveform, and (c) S2-waveform.

Table 17 summarizes the R-squared values for the P, S1, and S2 waveform predictions from both XGBoost and KNN models for all the validation cases. Generally, KNN allows continuous waveform predictions that closely follow the trends of the actual waveforms, making it effective at capturing the general behavior and P, S1, S2 arrival times, even when the R-squared values are low. This is due to its ability to average the outputs from the nearest neighbors in the feature space (Bishop, 2006). On the other hand, XGBoost uses an ensemble of decision trees for predictions. Each tree approximates the input-output relationship in piecewise steps, leading to step-like predictions with discrete jumps rather than smooth variations (Bishop, 2006). Consequently, KNN tends to achieve higher R-squared values for the predicted P, S1, and S2 waveforms compared to the XGBoost model.

Table 17: Error evaluation comparison between XGBoost and KNN models for the prediction of P, S1, and S2 waveforms of the three validation cases.

Validation #	XGBoost Prediction R^2			KNN Prediction R^2		
	P-Wave	S1-Wave	S2-Wave	P-Wave	S1-Wave	S2-Wave
1	0.9747	0.9292	0.8988	0.9804	0.9375	0.9548
2	0.8849	0.0093	0.1065	0.7258	0.264	0.2974
3	0.9426	0.6423	0.6342	0.9452	0.9078	0.8384

4.4 Discussion

4.4.1 Features Importance Evaluation (SHAP Evaluation)

SHapley Additive exPlanations (SHAP) were utilized to reveal key features (i.e., model inputs) that influence the prediction of P, S1, and S2 waveforms from the XGBoost model, with some features being more impactful than others (Shapley and Roth, 1988; Lipovetsky and Conklin, 2001). For the P-waveform prediction, the most influential factors are bulk density, temperature, axial stress, diameter, and fracture volume. These factors suggest that the physical properties of the rock, such as its density and size, along with the stress conditions and thermal state, significantly affect the propagation of the P-wave (Figure 52.a). The impact of fracture volume also points to the role of fracture size in impacting the compressional propagation of P-wave.

In the case of S1-wave predictions, temperature and bulk density are dominant factors, indicating their consistent influence across different waveform types. Fracture strike and axial stress are closely followed, showing that the alignment of stress with respect to the fracture orientation is crucial for predicting S1-wave behavior. Additionally, the sample diameter also plays a role, reinforcing the importance of rock geometry in the model's predictions for the S1-wave amplitude (Figure 52.b).

For S2-wave predictions, temperature emerges as the most critical factor, followed by axial stress, diameter, density, and fracture strike. This highlights the importance of fracture orientation in determining shear wave characteristics, particularly for the S2 wave (Figure 52.c). Across all three waveforms, the number of fractures, rock condition, rock type, and sample length exhibit minimal impact on the predicted amplitudes. This indicates that these factors contribute less to the model's output compared to the other parameters, suggesting that their effects are less pronounced in shaping the waveforms' behavior.

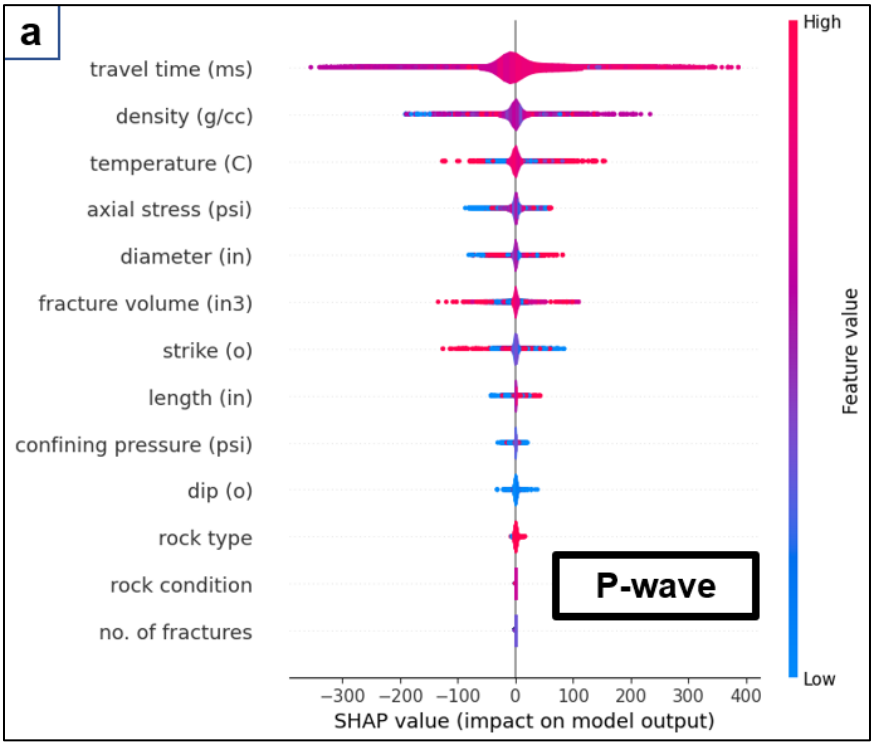

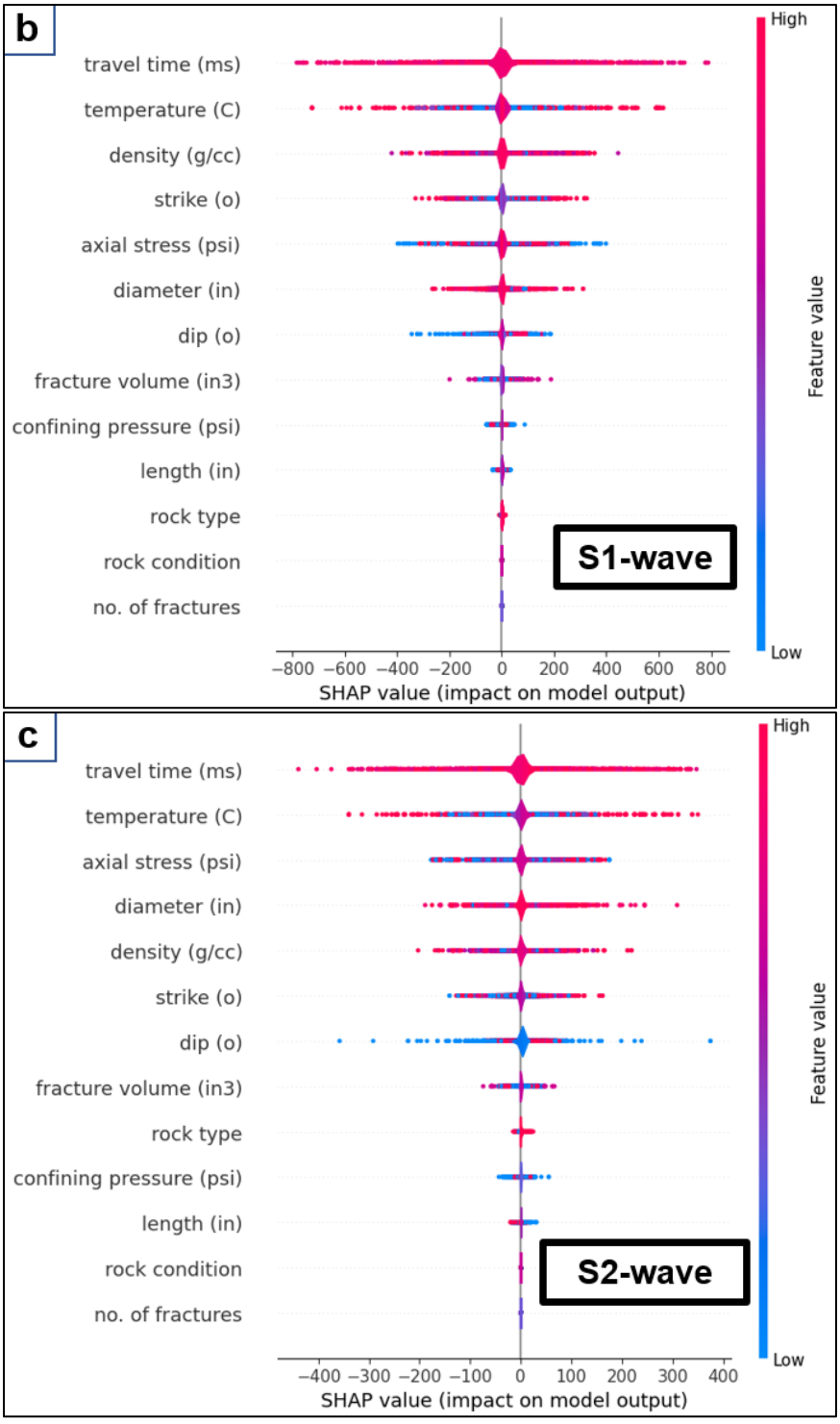

Figure 52: Features importance evaluation using SHAP for the XGBoost model for the prediction of: (a) P-wave, (b) S1-wave, and (c) S2-wave. The thicker the line, the higher the feature importance. The positive or negative correlation of each feature is explained by having the red-colored data to the right or to the left of the vertical axis, respectively.

4.5 Conclusions

This study investigated the effects of fracture characteristics, including strike, dip, and volume, along with temperature and stress on shear wave splitting (SWS), amplitude, and wavelength in five Caney and Eagle Ford shale samples. We measured P, S1, and S2 waveforms under controlled conditions using a triaxial Hoek cell. Results showed fracture strike negatively correlated with SWS, as misalignment with shear transducers caused wave attenuation. In contrast, a decrease in fracture dip increased SWS, likely due to greater shear tendency under anisotropic stress, creating larger fracture apertures. Fracture volume is also positively correlated with SWS. Amplitude correlated positively with axial stress and bulk density but negatively with fracture volume.

KNN and XGBoost machine learning models were trained to predict P, S1, and S2 waveforms based on sample dimensions, fracture properties, stress, and temperature. KNN consistently outperformed XGBoost, offering smoother predictions closely resembling actual waveforms, while XGBoost exhibited a step-like prediction pattern. SHAP analysis revealed that P was significantly influenced by bulk density, axial stress, and temperature. For S1, temperature, bulk density, and strike were primary influences, while axial stress and diameter were key for S2, with temperature as the dominant factor.

These findings enhance our understanding of the impact of fracture properties on P, S1, and S2 waveforms, enabling better predictions in the vicinity of the wellbore and aiding optimization of drilling and stimulation programs in unconventional shale plays.

4.6 Acknowledgments

The authors express their gratitude to the U.S. Department of Energy for their generous support under Grant # DE-FE0031776, as well as for granting permission to use the Caney

shale samples in this study. Special thanks are also extended to Professor Jim Puckette from the Boone Pickens School of Geology at Oklahoma State University, Dr. Gabriel Awejori, Dr. Ali Ettehadi, and Professor Mileva Radonjic from the Barrier Material and Geomimicry Laboratory at Oklahoma State University for their invaluable assistance.

CHAPTER V

5 Final Discussion and Conclusions

This dissertation investigated the behavior of acoustic waves under various subsurface conditions to improve the prediction of rock mechanical properties and natural fracture characteristics. The research combined experimental studies and machine learning techniques across three main topics to enhance understanding of how subsurface engineering applications such as carbon storage, well drilling, and stimulation can be optimized through improved geomechanical characterization. The key findings and contributions from each chapter are synthesized below, providing a comprehensive perspective on the significance of the work.

5.1 Integration of Poroelastic Properties for CO_2 Storage

The first study examined the effects of pore pressure and temperature on poroelastic properties, specifically the bulk modulus and Biot's coefficient, of Gray Berea sandstone under $scCO_2$ saturation. The results demonstrated that increased pore pressure positively correlated with Biot's coefficient due to reduced grain contact area, while elevated temperatures lowered Biot's coefficient, likely because of the thermal opening of microcracks. The finding that dynamic Biot's coefficient values were significantly higher than static values underscores the importance of considering dynamic measurements for subsurface modeling. Additionally, the results indicated that $scCO_2$ saturation at higher

temperatures increases storage capacity but poses more significant risks for fault stability due to critical stress path conditions. These insights provide valuable implications for geological carbon storage strategies, especially concerning reservoir integrity and long-term CO_2 sequestration.

5.2 Workflow for Predicting Dynamic-to-Static Correction Factor (F_{ds}) in Shale Reservoirs

The second study extended the investigation to unconventional reservoirs by focusing on the experimental evaluation of the dynamic mechanical properties of Caney shale under different triaxial stress conditions. Through a new workflow involving K-means clustering, principal component analysis (PCA), and inverse distance weighting (IDW), the research provided a method to predict the F_{ds}—ratio between static-to-dynamic Young's modulus—across stratigraphic zones. The workflow successfully identified key reservoir zones, differentiating between carbonate-rich and layered mudstone-siltstone facies. This zonation is crucial for optimizing drilling and stimulation strategies in unconventional plays. The results also highlighted the variability in mechanical behavior across ductile and reservoir layers, underscoring the need for tailored approaches when predicting static mechanical properties in heterogeneous formations. The workflow's applicability to other shale reservoirs emphasizes its potential for broader use in the oil and gas industry.

5.3 Influence of Natural Fracture Characteristics on Acoustic Waveforms and SWS

The third study experimentally investigated the impact of fracture properties (strike, dip, and volume) and triaxial conditions (stresses and temperature) on acoustic (P, S1, and S2) waveforms for Caney and Eagle Ford shale samples. The findings showed that fracture strike attenuates shear wave splitting (SWS) when the fracture is not aligned with either

one of the two orthogonal shear wave transducers. The increase in fracture volume resulted in a significant increase in SWS and a significant drop in wave amplitudes. The fracture dip had no clear impact on amplitude, while it showed a negative correlation with the SWS. These results provide insights into how fracture orientation and geometry influence acoustic signals, which are critical for interpreting subsurface conditions near wellbores. K-nearest neighbors (KNN) and extreme gradient boosting (XGBoost) models demonstrated the potential for predicting acoustic waveforms based on fracture and sample characteristics under triaxial conditions, with KNN achieving higher accuracy and smoother predictions facilitated arrival time estimation. These models offer a pathway to better understanding wave behavior in fractured media, aiding in the optimization of drilling and stimulation operations.

5.4 Suggested Future Work

The findings across all three studies present a cohesive framework for linking acoustic wave behavior with rock properties, advancing methods for monitoring and predicting subsurface geomechanical changes. Building on this dissertation's findings, future research could explore additional factors influencing acoustic wave behavior for fractured shale rocks, such as fluid viscosity and saturation changes. Expanding the machine learning models to include a wider range of datasets and testing environments could improve prediction accuracy and generalizability for acoustic waveforms. Furthermore, extending the methodologies to different rock types and fracture configurations would enhance the understanding of wave responses across various geological settings.

5.5 Final Remarks

The comprehensive investigation of acoustic wave behavior under varied subsurface conditions offers valuable contributions to the field of geomechanics. This dissertation not

only improves the understanding of rock mechanical properties and fracture characteristics but also advances practical techniques for subsurface monitoring and management. The integrated experimental and computational approach provides a foundation for future advancements in safe and efficient subsurface resource utilization.

BIBLIOGRAPHY

Abdelaal, M., Zeidouni, M., 2022. Injection data analysis using material balance time for CO2 storage capacity estimation in deep closed saline aquifers. Journal of Petroleum Science and Engineering 208, 109385. https://doi.org/10.1016/j.petrol.2021.109385

Abul Khair, H., Cooke, D., Hand, M., 2015. Paleo stress contribution to fault and natural fracture distribution in the Cooper Basin. Journal of Structural Geology 79, 31–41. https://doi.org/10.1016/j.jsg.2015.07.007

Abul Khair, H., Cooke, D., Hand, M., 2013. The effect of present day in situ stresses and paleo-stresses on locating sweet spots in unconventional reservoirs, a case study from Moomba-Big Lake fields, Cooper Basin, South Australia. Journal of Petroleum Exploration and Production Technology 3, 207–221. https://doi.org/10.1007/s13202-013-0082-x

Agofack, N., Lozovyi, S., Bauer, A., 2018. Effect of CO2 on P- and S-wave velocities at seismic and ultrasonic frequencies. International Journal of Greenhouse Gas Control 78, 388–399. https://doi.org/10.1016/j.ijggc.2018.09.010

Aguilera, R., 1980. Naturally Fractured Reservoirs, First Edition. ed. PennWell Books.

Alam, M.M., Hjuler, M.L., Christensen, H.F., Fabricius, I.L., 2014. Petrophysical and rock-mechanics effects of CO2 injection for enhanced oil recovery: Experimental study on chalk from South Arne field, North Sea. Journal of Petroleum Science and Engineering 122, 468–487. https://doi.org/10.1016/j.petrol.2014.08.008

Alpay, O.A., 1972. A Practical Approach to Defining Reservoir Heterogeneity. Journal of Petroleum Technology 24, 841–848. https://doi.org/10.2118/3608-PA

Alqahtani, A.A., Mokhtari, M., Tutuncu, A.N., Sonnenberg, S., 2013. Effect of Mineralogy and Petrophysical Characteristics on Acoustic and Mechanical Properties of Organic Rich Shale. Presented at the SPE/AAPG/SEG Unconventional Resources Technology Conference, p. URTEC-1619144-MS. https://doi.org/10.1190/urtec2013-045

AlQassab, M., Yu, W., Sepehrnoori, K., Kerr, E., Scofield, R., Johnson, A., 2020. Estimating the Size and Orientation of Hydraulic Fractures using Microseismic Events. Presented at the SPE/AAPG/SEG Unconventional Resources Technology Conference, p. D013S004R003. https://doi.org/10.15530/urtec-2020-2678

Al-Rubaye, A., Ben Mahmud, H.K., 2020. A numerical investigation on the performance of hydraulic fracturing in naturally fractured gas reservoirs based on stimulated rock volume. Journal of Petroleum Exploration and Production Technology 10, 3333–3345. https://doi.org/10.1007/s13202-020-00980-8

Ameen, M.S., Smart, B.G.D., Somerville, J.Mc., Hammilton, S., Naji, N.A., 2009. Predicting rock mechanical properties of carbonates from wireline logs (A case study: Arab-D reservoir, Ghawar field, Saudi Arabia). Marine and Petroleum Geology 26, 430–444. https://doi.org/10.1016/j.marpetgeo.2009.01.017

Asadollahpour, E., Ezazi, M., Mostafavi, I., Eshraghi, H., Mehrgini, B., Pezeshki, M., Ansari, M., 2021. Biot's coefficient determination of carbonate reservoir rocks by using static and dynamic experimental tests at ambient and reservoir temperatures - A case study from Iran carbonate field. Journal of Petroleum Science and Engineering 196, 108061. https://doi.org/10.1016/j.petrol.2020.108061

Awejori, G., Dong, W., Doughty, C., Radonjic, M., 2024. Geochemically-Driven Petrophysical Transformations in Caney Shale and Their Impact on Reservoir Productivity. Presented at the SPE/AAPG/SEG Unconventional Resources Technology Conference, p. D021S038R001. https://doi.org/10.15530/urtec-2024-4042958

Awejori, G.A., Dong, W., Doughty, C., Spycher, N., Radonjic, M., 2024. Mineralogy and reactive fluid chemistry evolution of hydraulically fractured Caney shale of Southern Oklahoma. Gas Science and Engineering 131, 205458. https://doi.org/10.1016/j.jgsce.2024.205458

Awejori, G.A., Luo, G., Grider, C., Katende, A., Radonjic, M., Doughty, C., Spycher, N., Paronish, T., O'Connell, L., Rihn, A., 2021. Fracturing Fluid-Induced Mineralogy Changes and Impact on Elastic Properties for the Caney Shale, Oklahoma. Presented at the 55th U.S. Rock Mechanics/Geomechanics Symposium, p. ARMA-2021-2004.

Bachu, S., 2008. CO2 storage in geological media: Role, means, status and barriers to deployment. Progress in Energy and Combustion Science 34, 254–273. https://doi.org/10.1016/j.pecs.2007.10.001

Bahorich, B., Olson, J.E., Holder, J., 2012. Examining the Effect of Cemented Natural Fractures on Hydraulic Fracture Propagation in Hydrostone Block Experiments. Presented at the SPE Annual Technical Conference and Exhibition, p. SPE-160197-MS. https://doi.org/10.2118/160197-MS

Ben, Y., Miao, Q., Wang, Y., Shi, G., 2012. Effect of Natural Fractures on Hydraulic Fracturing. Presented at the ISRM Regional Symposium - 7th Asian Rock Mechanics Symposium, p. ISRM-ARMS7-2012-087.

Benge, M., Katende, A., Rutqvist, J., Radonjic, M., Bunger, A., 2023. Creep Properties of Shale and Predicted Impact on Proppant Embedment for the Caney Shale, Oklahoma. Rock Mechanics and Rock Engineering 56, 5903–5921. https://doi.org/10.1007/s00603-023-03362-8

Benge, M., Lu, Y., Katende, A., Rutqvist, J., Crandall, D., Haecker, A., King, G., Renk, J.B., Radonjic, M., Bunger, A., 2021. Connecting Geomechanical Properties with Potential for Proppant Embedment and Production Decline for the Emerging Caney Shale, Oklahoma. Presented at the SPE/AAPG/SEG Unconventional Resources Technology Conference, p. D011S002R001. https://doi.org/10.15530/urtec-2021-5084

Benson, S.M., Cole, D.R., 2008. CO2 Sequestration in Deep Sedimentary Formations. Elements 4, 325–331. https://doi.org/10.2113/gselements.4.5.325

Bishop, C., 2006. Pattern Recognition and Machine Learning (Information Science and Statistics), 1st ed. ed.

Blanton, T.L., Olson, J.E., 1999. Stress Magnitudes from Logs: Effects of Tectonic Strains and Temperature. SPE Reservoir Evaluation & Engineering 2, 62–68. https://doi.org/10.2118/54653-PA

Bratton, T., Canh, D.V., Duc, N.V., Gillespie, P., Hunt, D., Li, B., Marcinew, R., Ray, S., Montaron, B., Nelson, R., Schoderbek, D., Sonneland, L., 2006. The Nature of Naturally Fractured Reservoirs. Oilfield Review.

Cai, M., Wu, H., Xin, Y., Liu, P., Zhang, C., Tang, J., Lin, M., Tan, L., 2022. Experimental Study on Shear Wave Transmission in Fractured Media. Sensors 22, 4047. https://doi.org/10.3390/s22114047

Cardott, B.J., 2017. Oklahoma shale resource plays. Oklahoma Geology Notes 76, 21–30.

Cataldo, R.A., Leite, E.P., Mattos, N.H.S., 2022. Impact of mineralogy on rock physics modeling: a Brazilian Pre-Salt Case Study, presented at: Second International Meeting for Applied Geoscience & Energy, SEG Technical Program Expanded Abstracts. Society of Exploration Geophysicists and American Association of Petroleum Geologists, pp. 2333–2337. https://doi.org/10.1190/image2022-3751121.1

Chadwick, R., Arts, R., Bernstone, C., May, F., Thibeau, S., Zweigel, P., 2008. Best practice for the storage of CO2 in saline aquifers - observations and guidelines from the SACS and CO2STORE projects. British Geological Survey Occasional Publication 14, 1–267.
Cheung, P.K.S., 1978. The Geothermal Gradient in Sedimentary Rocks in Oklahoma (MSc Thesis). Oklahoma State University, Stillwater, Oklahoma.
Comerlati, A., Ferronato, M., Gambolati, G., Putti, M., Teatini, P., 2006. Fluid-Dynamic and Geomechanical Effects of CO2 Sequestration below the Venice Lagoon. Environmental & Engineering Geoscience 12, 211–226. https://doi.org/10.2113/gseegeosci.12.3.211
Cox, P., Betts, R., Jones, C., Spall, S., Totterdell, I., 2000. Acceleration of global warming due to carbon-cycle feedbacks in a coupled climate model. Nature 408: 184-187. Nature 408. https://doi.org/10.1038/35041539
Crampin, S., 1985. Evaluation of anisotropy by shear-wave splitting. Geophysics 50, 142–152. https://doi.org/10.1190/1.1441824
Crampin, S., 1981. A review of wave motion in anisotropic and cracked elastic-media. Wave Motion 3, 343–391. https://doi.org/10.1016/0165-2125(81)90026-3
Dande, S., Stewart, R.R., Myers, M.T., Hathon, L., Dyaur, N., 2019. Elastic Properties of Propped and Unpropped Eagle Ford Shale and 3D-Printed Fractured Models Under Iso-static Stress. Presented at the SPE/AAPG/SEG Unconventional Resources Technology Conference, p. D013S007R001. https://doi.org/10.15530/urtec-2019-115
Delhomme, J.-P., Pilenko, T., Cheruvier, E., Cull, R., 1988. Reservoir Applications of Dipmeter Logs. Journal of Petroleum Technology 40, 180–186. https://doi.org/10.2118/15485-PA
Delle Piane, C., Sarout, J., 2016. Effects of water and supercritical CO2 on the mechanical and elastic properties of Berea sandstone. International Journal of Greenhouse Gas Control 55, 209–220. https://doi.org/10.1016/j.ijggc.2016.06.001
Denney, D., 2012. Improve Unconventional-Reservoir Completion and Stimulation Effectiveness. Journal of Petroleum Technology 64, 115–119. https://doi.org/10.2118/1012-0115-JPT
Ding, J., Clark, A.C., Vanorio, T., Jew, A.D., Bargar, J.R., 2021. Acoustic velocity and permeability of acidized and propped fractures in shale. Geophysics 87, MR13–MR24. https://doi.org/10.1190/geo2020-0873.1
Dje, L.B., Awejori, G.A., Radonjic, M., 2024. Comparison of Geochemical Reactivity of Marcellus and Caney Shale Based on Effluent Analysis. Presented at the 58th U.S. Rock Mechanics/Geomechanics Symposium, p. D041S053R004. https://doi.org/10.56952/ARMA-2024-1079
Donald, J.A., Jocker, J., Leaney, S., Dasgupta, S., Van Kleef, F., Brindle, F., 2018. TI elastic-property inversion on basis of walkaway VSP and full-waveform sonic, in: SEG Technical Program Expanded Abstracts 2018, SEG Technical Program Expanded Abstracts. Society of Exploration Geophysicists, pp. 286–290. https://doi.org/10.1190/segam2018-2995273.1
Dong, T., Harris, N.B., Ayranci, K., Yang, S., 2017. The impact of rock composition on geomechanical properties of a shale formation: Middle and Upper Devonian Horn River Group shale, Northeast British Columbia, Canada. AAPG Bulletin 101, 177–204.
Ehlig-Economides, C., Economides, M.J., 2010. Sequestering carbon dioxide in a closed underground volume. Journal of Petroleum Science and Engineering 70, 123–130. https://doi.org/10.1016/j.petrol.2009.11.002
Elsayed, M., El-Husseiny, A., Kwak, H., Hussaini, S.R., Mahmoud, M., 2021. New Technique for Evaluating Fracture Geometry and Preferential Orientation Using Pulsed Field Gradient Nuclear Magnetic Resonance. SPE Journal 26, 2880–2893. https://doi.org/10.2118/205505-PA

Falcon-Suarez, I., Best, A., North, L., Browning, F., 2016. Nondestructive assessment of static and dynamic geomechanical properties of sandstone samples for geological CO2 storage monitoring. pp. 3231–3235. https://doi.org/10.1190/segam2016-13527767.1

Fjær, E., Holt, R.M., Horsrud, P., Raaen, A.M., Risnes, R., 2008. Chapter 8 Mechanical properties and in situ stresses from field data, in: Fjær, E., Holt, R.M., Horsrud, P., Raaen, A.M., Risnes, R. (Eds.), Developments in Petroleum Science. Elsevier, pp. 289–308. https://doi.org/10.1016/S0376-7361(07)53008-6

Gale, J.F.W., Reed, R.M., Holder, J., 2007. Natural fractures in the Barnett Shale and their importance for hydraulic fracture treatments. AAPG Bulletin 91, 603–622. https://doi.org/10.1306/11010606061

Garg, A., Zwahlen, E., Patzek, T.W., 1996. Experimental and numerical studies of one-dimensional imbibition in Berea sandstone. Proceedings of the Sixteenth Annual American Geophysical Union Hydrology Days, Fort Collins, CO 15–18.

Geertsma, J., 1957. The Effect of Fluid Pressure Decline on Volumetric Changes of Porous Rocks. Transactions of the AIME 210, 331–340. https://doi.org/10.2118/728-G

Georgi, D.T., 1986. Guides For the Interpretation of Dipmeter Fracture Logs. Presented at the SPWLA 27th Annual Logging Symposium, p. SPWLA-1986-TT.

Gholami, R., Moradzadeh, A., Rasouli, V., Hanachi, J., 2016. Shear Wave Splitting Analysis to Estimate Fracture Orientation and Frequency Dependent Anisotropy. Acta Geophysica 64, 76–100. https://doi.org/10.1515/acgeo-2015-0060

Guo, W., Guo, Y., Cai, Z., Yang, H., Wang, L., Yang, C., Zhao, G., Bi, Z., 2023. Mechanical behavior and constitutive model of shale under real-time high temperature and high stress conditions. Journal of Petroleum Exploration and Production Technology 13, 827–841. https://doi.org/10.1007/s13202-022-01580-4

Gutierrez, M., Katsuki, D., Almrabat, A., 2013. Use of the Biot-Gassmann Equation in Modeling of the Seismic Velocity Changes During Supercritical CO 2 Injection in Sandstone, Poromechanics V - Proceedings of the 5th Biot Conference on Poromechanics. https://doi.org/10.1061/9780784412992.001

Hart, D.J., Wang, H.F., 1995. Laboratory measurements of a complete set of poroelastic moduli for Berea sandstone and Indiana limestone. Journal of Geophysical Research: Solid Earth 100, 17741–17751. https://doi.org/10.1029/95JB01242

Hesse, M.A., Orr Jr., F.M., Tchelepi, H.A., 2009. Gravity currents with residual trapping. Energy Procedia 1, 3275–3281. https://doi.org/10.1016/j.egypro.2009.02.113

Hudson, J.A., 1981. Wave speeds and attenuation of elastic waves in material containing cracks. Geophysical Journal International 64, 133–150. https://doi.org/10.1111/j.1365-246X.1981.tb02662.x

Jalil, M.A.A., Masoudi, R., Darman, N.H., Othman, M., 2012. Study the CO2 Injection and Sequestration in Depleted M4 Carbonate Gas Condensate Reservoir, Malaysia.

Jones, S.C., 1987. Using the Inertial Coefficient, ß, To Characterize Heterogeneity in Reservoir Rock, in: All Days. Presented at the SPE Annual Technical Conference and Exhibition, SPE, Dallas, Texas, p. SPE-16949-MS. https://doi.org/10.2118/16949-MS

Juanes, R., Spiteri, E.J., Orr Jr., F.M., Blunt, M.J., 2006. Impact of relative permeability hysteresis on geological CO2 storage. Water Resources Research 42. https://doi.org/10.1029/2005WR004806

Kasani, H.A., Selvadurai, A.P.S., 2022. A Review of Techniques for Measuring the Biot Coefficient and Other Effective Stress Parameters for Fluid-Saturated Rocks. Applied Mechanics Reviews 75. https://doi.org/10.1115/1.4055888

Katende, A., Allen, C., Massion, C., Awejori, A.G., Xiong, F., Radonjic, M., Rutqvist, J., Nakagawa, S., 2022. Experiments and Modeling of Proppant Embedment and Fracture Conductivity for the Caney Shale, Oklahoma, USA, in: All Days. Presented at the 56th

U.S. Rock Mechanics/Geomechanics Symposium, ARMA, Santa Fe, New Mexico, USA, p. ARMA-2022-0805. https://doi.org/10.56952/ARMA-2022-0805
Katende, A., Rutqvist, J., Benge, M., Seyedolali, A., Bunger, A., Puckette, J.O., Rhin, A., Radonjic, M., 2021. Convergence of micro-geochemistry and micro-geomechanics towards understanding proppant shale rock interaction: A Caney shale case study in southern Oklahoma, USA. Journal of Natural Gas Science and Engineering 96, 104296. https://doi.org/10.1016/j.jngse.2021.104296
Kholy, S.M., Lee, H.P., 2023. Experimental Investigation of Fracture Orientation in Rocks Using Shear Wave Splitting. Presented at the 57th U.S. Rock Mechanics/Geomechanics Symposium, p. ARMA-2023-0792. https://doi.org/10.56952/ARMA-2023-0792
Kholy, S.M., Lee, H.P., Radonjic, M., 2024. Integrating Experiments and Well Logs to Predict Caney Shale Static Mechanical Properties During Production with Supervised Machine Learning, in: The Unconventional Resources Technology Conference. Presented at the The Unconventional Resources Technology Conference, American Association of Petroleum Geologists, Houston, TX USA. https://doi.org/10.15530/urtec-2024-4038060
King, G.E., 2012. Hydraulic Fracturing 101: What Every Representative, Environmentalist, Regulator, Reporter, Investor, University Researcher, Neighbor and Engineer Should Know About Estimating Frac Risk and Improving Frac Performance in Unconventional Gas and Oil Wells. Presented at the SPE Hydraulic Fracturing Technology Conference, p. SPE-152596-MS. https://doi.org/10.2118/152596-MS
Kolmer, H.P., Mayibeki, D., Hareland, G., 2021. Using Drilling Data of Offset Wells and Core Data to Optimize Perforation Selection for the Caney Shale. Presented at the 55th U.S. Rock Mechanics/Geomechanics Symposium, p. ARMA-2021-1934.
Lamy-Chappuis, B., Angus, D., Fisher, Q.J., Yardley, B.W.D., 2016. The effect of CO2-enriched brine injection on the mechanical properties of calcite-bearing sandstone. International Journal of Greenhouse Gas Control 52, 84–95. https://doi.org/10.1016/j.ijggc.2016.06.018
Lee, H.P., Olson, J.E., 2017. The effect of remote and internal crack stresses on mixed-mode brittle fracture propagation of open cracks under compressive loading. Int J Fract 207, 229–242. https://doi.org/10.1007/s10704-017-0231-1
Lee, H.P., Olson, J.E., Holder, J., Gale, J.F.W., Myers, R.D., 2015. The interaction of propagating opening mode fractures with preexisting discontinuities in shale. Journal of Geophysical Research: Solid Earth 120, 169–181. https://doi.org/10.1002/2014JB011358
Lee, H.P., Olson, J.E., Schultz, R.A., 2018. Interaction analysis of propagating opening mode fractures with veins using the Discrete Element Method. International Journal of Rock Mechanics and Mining Sciences 103, 275–288. https://doi.org/10.1016/j.ijrmms.2018.01.005
Li, Z., Peng, Z., 2017. Stress- and Structure-Induced Anisotropy in Southern California from Two Decades of Shear Wave Splitting Measurements. Geophysical Research Letters 44, 9607–9614. https://doi.org/10.1002/2017GL075163
Liao, G., Du, Y., Zhang, F., E, J., 2023. Comprehensive review on physical properties of supercritical carbon dioxide calculated by molecular simulation. Korean Journal of Chemical Engineering 40, 11–36. https://doi.org/10.1007/s11814-022-1316-8
Likrama, F., Ouriri, F., Bouarfetine, D., Hammoudi, A., Ouargli, A., Iddir, M., 2019. Inferring Current Day and Paleo Stress Orientation from Natural Fracture Geometry. Presented at the 53rd U.S. Rock Mechanics/Geomechanics Symposium, p. ARMA-2019-0431.
Lipovetsky, S., Conklin, M., 2001. Analysis of regression in game theory approach. Applied Stochastic Models in Business and Industry 17, 319–330. https://doi.org/10.1002/asmb.446

Luffel, D.L., Hopkins, C.W., Schettler, P.D., Jr., 1993. Matrix Permeability Measurement of Gas Productive Shales. Presented at the SPE Annual Technical Conference and Exhibition, p. SPE-26633-MS. https://doi.org/10.2118/26633-MS

Ma, X., Zoback, M.D., 2017. Laboratory experiments simulating poroelastic stress changes associated with depletion and injection in low-porosity sedimentary rocks. Journal of Geophysical Research: Solid Earth 122, 2478–2503. https://doi.org/10.1002/2016JB013668

Maerten, L., Maerten, F., 2006. Chronologic modeling of faulted and fractured reservoirs using geomechanically based restoration: Technique and industry applications. AAPG Bulletin 90, 1201–1226. https://doi.org/10.1306/02240605116

Majidi, R., Miska, S.Z., Yu, M., Thompson, L.G., 2010. Quantitative Analysis of Mud Losses in Naturally Fractured Reservoirs: The Effect of Rheology.

Martin, M.A., Davis, T.L., 1987. Shear-wave birefringence: A new tool for evaluating fractured reservoirs. The Leading Edge 6, 22–28. https://doi.org/10.1190/1.1439333

Mayibeki, D.N., 2021. Drilling Optimization of a Caney Shale Well using Offset Well Drilling Data (MSc Thesis). Oklahoma State University, Stillwater, Oklahoma.

McPhee, C., Reed, J., Zubizarreta, I., 2015. Chapter 12 - Geomechanics Tests, in: McPhee, C., Reed, J., Zubizarreta, I. (Eds.), Developments in Petroleum Science. Elsevier, pp. 671–779. https://doi.org/10.1016/B978-0-444-63533-4.00012-3

Meinshausen, M., Meinshausen, N., Hare, W., Raper, S.C.B., Frieler, K., Knutti, R., Frame, D.J., Allen, M.R., 2009. Greenhouse-gas emission targets for limiting global warming to 2 °C. Nature 458, 1158–1162. https://doi.org/10.1038/nature08017

Mondol, N., 2008. Elastic properties of clay minerals. The Leading Edge.

Moore, C.H., Wade, W.J., 2013. Chapter 11 - Natural Fracturing in Carbonate Reservoirs, in: Moore, C.H., Wade, W.J. (Eds.), Developments in Sedimentology. Elsevier, pp. 285–300. https://doi.org/10.1016/B978-0-444-53831-4.00011-2

Narr, W., 2012. Naturally Fractured Reservoir Characterization. Society of Petroleum Engineers.

Newell, P., Ilgen, A.G., 2019. Chapter 1 - Overview of Geological Carbon Storage (GCS), in: Newell, P., Ilgen, A.G. (Eds.), Science of Carbon Storage in Deep Saline Formations. Elsevier, pp. 1–13. https://doi.org/10.1016/B978-0-12-812752-0.00001-0

Nielsen, R.M., Kohlhaas, C.A., 1979. Acoustic And Biaxial Measurement of Rock Mechanical Properties For Interpretation Of Logs For Design Of Well-Completion Operations. Presented at the SPE Annual Technical Conference and Exhibition, p. SPE-8238-MS. https://doi.org/10.2118/8238-MS

Nur, A., Byerlee, J.D., 1971. An exact effective stress law for elastic deformation of rock with fluids. Journal of Geophysical Research (1896-1977) 76, 6414–6419. https://doi.org/10.1029/JB076i026p06414

Onyebuchi, V.E., Kolios, A., Hanak, D.P., Biliyok, C., Manovic, V., 2018. A systematic review of key challenges of CO2 transport via pipelines. Renewable and Sustainable Energy Reviews 81, 2563–2583. https://doi.org/10.1016/j.rser.2017.06.064

Pan, X., Lu, C., Zhang, G., Wang, P., Liu, J., 2022. Seismic Characterization of Naturally Fractured Reservoirs with Monoclinic Symmetry Induced by Horizontal and Tilted Fractures from Amplitude Variation with Offset and Azimuth. Surveys in Geophysics 43, 815–851. https://doi.org/10.1007/s10712-022-09709-0

Pradhan, S., Stroisz, A.M., Fjær, E., Stenebråten, J.F., Lund, H.K., Sønstebø, E.F., 2015. Stress-Induced Fracturing of Reservoir Rocks: Acoustic Monitoring and μCT Image Analysis. Rock Mech Rock Eng 48, 2529–2540. https://doi.org/10.1007/s00603-015-0853-4

Pyale, D., Nieto, J.A., Austin, S.P., 1995. The effect of cementation on the static and dynamic mechanical properties of the Rotliegendes sandstone. Presented at the 35th U.S. Symposium on Rock Mechanics (USRMS), p. ARMA-95-0169.

Hill, R., 1952. The Elastic Behavior of a Crystalline Aggregate. Proceedings of the Physical Society. Section A 65, 349. https://doi.org/10.1088/0370-1298/65/5/307
Radonjic, M., Luo, G., Wang, Y., Achang, M., Cains, J., Katende, A., Puckette, J., Grammer, M., King, G.E., 2020. Integrated Microstructural Characterisation of Caney Shale, OK. Presented at the SPE/AAPG/SEG Unconventional Resources Technology Conference, p. D023S039R003. https://doi.org/10.15530/urtec-2020-2947
Razavi, O., Lee, H.P., Olson, J.E., Schultz, R.A., 2017. Drilling Mud Loss in Naturally Fractured Reservoirs: Theoretical Modelling and Field Data Analysis. Presented at the SPE Annual Technical Conference and Exhibition, p. D011S005R003. https://doi.org/10.2118/187265-MS
Raziperchikolaee, S., 2023. Impact of stress dependence of elastic moduli and poroelastic constants on earth surface uplift due to injection. Advances in Geo-Energy Research 10, 56–64. https://doi.org/10.46690/ager.2023.10.06
Raziperchikolaee, S., Singh, V., Kelley, M., 2020. The effect of Biot coefficient and elastic moduli stress–pore pressure dependency on poroelastic response to fluid injection: laboratory experiments and geomechanical modeling. Greenhouse Gases: Science and Technology 10, 980–998. https://doi.org/10.1002/ghg.2019
Reese, E.C., 2013. Lithofacies and Chemostratigraphic Evaluation of the Woodford Shale in the Western Arkoma and Eastern Anadarko Basins, Oklahoma.
Rial, J.A., Elkibbi, M., Yang, M., 2005. Shear-wave splitting as a tool for the characterization of geothermal fractured reservoirs: lessons learned. Geothermics 34, 365–385. https://doi.org/10.1016/j.geothermics.2005.03.001
Riziq Maulana, M., Syamsu Rosid, M., Farhan, Iskandar, C., 2019. Identification of Fracture Density and Orientation at "R" Geothermal Field Using Shear Wave Splitting Microearthquake Method. Journal of Physics: Conference Series 1351, 012050. https://doi.org/10.1088/1742-6596/1351/1/012050
Rutqvist, J., 2012. The Geomechanics of CO2 Storage in Deep Sedimentary Formations. Geotechnical and Geological Engineering 30, 525–551. https://doi.org/10.1007/s10706-011-9491-0
Rutqvist, J., Tsang, C.-F., 2005. Coupled hydromechanical effects of CO2 injection, in: Tsang, Chin-Fu, Apps, J.A. (Eds.), Developments in Water Science. Elsevier, pp. 649–679. https://doi.org/10.1016/S0167-5648(05)52050-1
Rybacki, E., Reinicke, A., Meier, T., Makasi, M., Dresen, G., 2015. What controls the mechanical properties of shale rocks? – Part I: Strength and Young's modulus. Journal of Petroleum Science and Engineering 135, 702–722. https://doi.org/10.1016/j.petrol.2015.10.028
Sakhaee-Pour, A., Bryant, S.L., 2011. Gas Permeability of Shale. Presented at the SPE Annual Technical Conference and Exhibition, p. SPE-146944-MS. https://doi.org/10.2118/146944-MS
Sanfillippo, F., Brignoli, M., Santarelli, F.J., 1997. Characterization of Conductive Fractures While Drilling.
Schoenberg, M., Sayers, C.M., 1995. Seismic anisotropy of fractured rock. Geophysics 60, 204–211. https://doi.org/10.1190/1.1443748
Shapley, L.S., Roth, A.E., 1988. The Shapley value: essays in honor of Lloyd S. Shapley. Cambridge University Press.
Shehata Ahmed Hussein, A.M., 2016. The role of mineral composition, rock permeability, and connate-water composition on the performance of low-salinity waterflooding in sandstone reservoirs.
Skempton, A., 1984. Effective stress in soils, concrete and rocks. Selected papers on soil mechanics 1032, 4–16.

Słota-Valim, M., 2015. Static and dynamic elastic properties, the cause of the difference and conversion methods – case study. Nafta-Gaz 71, 816–826. https://doi.org/10.18668/NG2015.11.02

Sokama-Neuyam, Y.A., Aggrey, W.N., Boakye, P., Sarkodie, K., Oduro-Kwarteng, S., Ursin, J.R., 2022. The effect of temperature on CO2 injectivity in sandstone reservoirs. Scientific African 15, e01066. https://doi.org/10.1016/j.sciaf.2021.e01066

Somerton, W.H., Janah, A.H., Ashqar, P.I., 1981. Thermal Expansion of Fluid Saturated Rocks Under Stress. Presented at the SPWLA 22nd Annual Logging Symposium, p. SPWLA-1981-D.

Sone, H., Zoback, M.D., 2013. Mechanical properties of shale-gas reservoir rocks — Part 1: Static and dynamic elastic properties and anisotropy. Geophysics 78, D381–D392. https://doi.org/10.1190/geo2013-0050.1

Suarez-Rivera, R., Handwerger, D., Kieschnick, J., Martin, W., Green, S., 2005. Accounting for Heterogeneity Provides a New Perspective for Completions in Tight Gas Shales. Presented at the Alaska Rocks 2005, The 40th U.S. Symposium on Rock Mechanics (USRMS), p. ARMA-05-758.

Tan, J., Xie, B., Lyu, Q., Chen, S., Ranjith, P.G., 2022. Mechanical Properties of Shale After CO2 and CO2-Based Fluids Imbibition: Experimental and Modeling Study. Rock Mechanics and Rock Engineering 55, 1197–1212. https://doi.org/10.1007/s00603-021-02702-w

Tang, X., Jiang, Z., Jiang, S., Li, Z., Peng, Y., Xiao, D., Xing, F., 2018. Effects of organic matter and mineral compositions on pore structures of shales: A comparative study of lacustrine shale in Ordos Basin and Marine Shale in Sichuan Basin, China. Energy Exploration & Exploitation 36, 28–42. https://doi.org/10.1177/0144598717723646

Tarokh, A., Makhnenko, R.Y., Kim, K., Zhu, X., Popovics, J.S., Segvic, B., Sweet, D.E., 2020. Influence of CO2 injection on the poromechanical response of Berea sandstone. International Journal of Greenhouse Gas Control 95, 102959. https://doi.org/10.1016/j.ijggc.2020.102959

Tavakoli, V., 2020. Carbonate Reservoir Heterogeneity: Overcoming the Challenges, Springer Briefs in Petroleum Geoscience & Engineering. Springer International Publishing, Cham. https://doi.org/10.1007/978-3-030-34773-4

Terzaghi, K., 1923. Dir Berenchnung der Durchlassigkeitsziffer des Tones aus dem Verlaug der Hidro-dynamischen Spannungsercheinungen. Akademie der Wissenschaften in Wein. Sitzungsberichte. Mathematish Naturwissenschaftliche Klasse 125–138.

Thompson, T.W., Kelkar, S.M., Gray, K.E., 1983. Effect of pore pressure on the elastic moduli, porosity and permeability of Berea sandstone and Leuders limestone. United States.

Tillotson, P., Sothcott, J., Best, A.I., Chapman, M., Li, X.-Y., 2012. Experimental verification of the fracture density and shear-wave splitting relationship using synthetic silica cemented sandstones with a controlled fracture geometry. Geophysical Prospecting 60, 516–525. https://doi.org/10.1111/j.1365-2478.2011.01021.x

Todd, T., Simmons, G., 1972. Effect of pore pressure on the velocity of compressional waves in low-porosity rocks. Journal of geophysical research 77, 3731–3743.

Vidal, S., Huguet, F., Mechler, P., 2002. Characterizing reservoir parameters by integrating seismic monitoring and geomechanics. The Leading Edge 21, 295–301. https://doi.org/10.1190/1.1463781

Vidal-Gilbert, S., Tenthorey, E., Dewhurst, D., Ennis-King, J., Van Ruth, P., Hillis, R., 2010. Geomechanical analysis of the Naylor Field, Otway Basin, Australia: Implications for CO2 injection and storage. International Journal of Greenhouse Gas Control 4, 827–839. https://doi.org/10.1016/j.ijggc.2010.06.001

Wang, H., 2000. Theory of linear poroelasticity with applications to geomechanics and hydrogeology. Princeton university press.

Wang, Y., Luo, G., Achang, M., Cains, J., Wethington, C., Katende, A., Grammer, G.M., Puckette, J., Pashin, J., Castagna, M., 2021. Multiscale characterization of the caney shale—an emerging play in Oklahoma. Midcontinent Geoscience 2, 33–53.
Warpinski, N., 2009. Microseismic Monitoring: Inside and Out. Journal of Petroleum Technology 61, 80–85. https://doi.org/10.2118/118537-JPT
Wennberg, O.P., Casini, G., Jonoud, S., Peacock, D.C.P., 2016. The characteristics of open fractures in carbonate reservoirs and their impact on fluid flow: a discussion. Petroleum Geoscience 22, 91–104. https://doi.org/10.1144/petgeo2015-003
Xiong, F., Awejori, G., Radonjic, M., 2024. Effects of Interactions Between Produced Formation Fluid and Rock Matrix on Pore Structure of Caney Shale, Southern Oklahoma. Presented at the 58th U.S. Rock Mechanics/Geomechanics Symposium, p. D041S053R002. https://doi.org/10.56952/ARMA-2024-0837
Xiong, J., Gan, R., Liu, X., Liang, L., Guo, X., 2023. Evaluation of the Rock Mechanical Properties of Shale Oil Reservoirs: A Case Study of Permian Lucaogou Formation in the Jimusar Sag, Junggar Basin. Applied Sciences 13, 12851. https://doi.org/10.3390/app132312851
Xiwei, C., Schmitt, D.R., Kessler, J.A., Evans, J., Kofman, R., 2015. Empirical relations between ultrasonic P-wave velocity, porosity and uniaxial compressive strength. csegrecorder 40.
Yale, D.P., Jamieson, W.H., Jr., 1994. Static and Dynamic Mechanical Properties of Carbonates. Presented at the 1st North American Rock Mechanics Symposium, p. ARMA-1994-0463.
Yang, B., Wang, H., Wang, B., Yi, Y., Zhao, C., Tian, G., 2023. Effect of Supercritical CO2-Water/Brine-Rock Interaction on Microstructures and Mechanical Properties of Tight Sandstone. Transport in Porous Media 149, 87–115. https://doi.org/10.1007/s11242-022-01834-z
Yang, G., Sun, J., Xie, D., Zhang, C., Pu, Y., 1998. CT identification of the mechanical characteristics of damage propagation of rock. Journal of Coal Science and Engineering 3, 21–25.
Yin, S., Xie, R., 2019. Experimental analysis of dynamic and static mechanical properties of deep thick anhydrite cap rocks under high-stress conditions. Carbonates and Evaporites 34, 807–823. https://doi.org/10.1007/s13146-018-0450-1
Yun, A., Song, I., 2022. Pore fluid substitution effects on elastic wave propagation in Berea sandstone: Implication to seismic monitoring of CO2 geologic storage. International Journal of Greenhouse Gas Control 115, 103609. https://doi.org/10.1016/j.ijggc.2022.103609
Zhang, D., Tang, J., Chen, K., Wang, K., Zhang, P., He, G., Tuo, X., 2022. Simulation of tectonic stress field and prediction of tectonic fracture distribution in Longmaxi Formation in Lintanchang area of eastern Sichuan Basin. Frontiers in Earth Science 10.
Zhou, J., Chen, M., Jin, Y., Zhang, G., 2008. Analysis of fracture propagation behavior and fracture geometry using a tri-axial fracturing system in naturally fractured reservoirs. International Journal of Rock Mechanics and Mining Sciences 45, 1143–1152. https://doi.org/10.1016/j.ijrmms.2008.01.001
Zhou, X., Zeng, Z., Liu, H., Boock, A., 2009. Laboratory Testing on Geomechanical Properties of Carbonate Rocks for CO2 Sequestration. Presented at the 43rd U.S. Rock Mechanics Symposium & 4th U.S. - Canada Rock Mechanics Symposium, p. ARMA-09-011.
Zoback, M.D., 2007. Reservoir Geomechanics. Cambridge University Press, Cambridge. https://doi.org/10.1017/CBO9780511586477

APPENDICES

Appendix A

K-Means Clustering

This technique aims to partition n observations of a dataset into k clusters as follows (Bishop, 2006):

1. The variables of a dataset are normalized using Equation (A.1)

   $$X_i = \frac{x_i - \mu}{\sigma} \quad \text{(A.1)}$$

   where X_i and x_i represent the normalized and unnormalized variables, respectively. σ is the standard deviation, and μ is the mean of the unnormalized variable.

2. Initial k centroids are assumed for the k clusters.

3. Each observation X_i is assigned to its nearest centroid.

4. The new k centroids are calculated so that each centroid is the average of its assigned observations.

5. Steps 3 and 4 are repeated until having stable centroids.

   Several k-values are evaluated following the above steps, and the optimum k corresponds to the lowest within-cluster sum of squares (WCSS), which is calculated from Equation (A.2).

   $$WCSS = \sum_{i=1}^{k} \sum_{x_j \epsilon C_i} \left\| X_j - \mu_i \right\|^2 \quad \text{(A.2)}$$

   where C_i is the i-th cluster, X_j is a datapoint in cluster C_i, μ_i is the centroid of the i-th cluster, and k is the number of clusters.

The optimum number of clusters (k) can be graphically identified through one of the following charts:

1. Elbow chart: the chart plots WCSS versus k, and the optimum k corresponds to the elbow point where the rate of decrease of WCSS sharply slows.
2. Silhouette chart: the chart plots the overall Silhouette score (S) versus k, so that the optimum k corresponds to the highest s value, which is calculated from Equations (A.3) and (A.4).

$$s(i) = \frac{b(i)-a(i)}{\max(a(i),b(i))} \quad \text{(A.3)}$$

$$S = \frac{1}{n}\sum_{i=1}^{n} s(i) \quad \text{(A.4)}$$

where *a(i)* and *b(i)* represent the average distance between the datapoint (*i*) and the other points in the same cluster and in the nearest neighboring cluster, respectively. *s(i)* is the Silhouette score of datapoint (*i*). *S* is the overall Silhouette score of a cluster and *n* is the number of datapoints in a cluster.

Principal Component Analysis (PCA)

The PCA calculation can be summarized as follows:

1. The variables of a dataset are normalized using Equation (A.1)
2. The covariance matrix (C) is computed, and it shows relationships between the variables of a dataset matrix (*X*), Equation (A.5), with n observations.

$$\mathrm{C} = \frac{1}{n-1} X^T X \quad \text{(A.5)}$$

3. Eigen values and Eigen vectors of the covariance matrix (C) are calculated then sorted in descending order: The eigenvalues and eigenvectors of the covariance matrix are computed. The top *K* Eigen vectors represent the *K* principal components.
4. The original data is projected onto the principal components to obtain the transformed dataset. Equation (A.6) shows the transformed dataset matrix (*Y*), where matrix (*W*)

contains the *K* Eigen vectors.

$$Y = XW \quad \text{(A.6)}$$

Inverse Distance Weighting (IDW)

The IDW estimation method predicts the value of unknown point as follows:

1. Calculate distance (d_i) between unknown datapoint *P* with coordinates (x, y, z) and each known datapoint P_i with coordinates (x_i, y_i, z_i)

$$d_i = \sqrt{(x_i - x)^2 + (y_i - y)^2 + (z_i - z)^2} \quad \text{(A.7)}$$

2. Calculate the weight (w_i) which is the inverse of distance (d_i) to the power (p), which is typically assumed as 2.

$$w_i = \frac{1}{d_i^p} \quad \text{(A.8)}$$

3. Normalize the weights so that their sum equals to 1, where m represents number of known *j* points, and λ_j is the normalized weight.

$$\lambda_j = \frac{w_i}{\sum_j^m w_j} \quad \text{(A.9)}$$

4. Estimate the value *V* at the unknown point *P*, where V_j is the known *j* point:

$$V = \sum_j^m \lambda_j V_j \quad \text{(A.10)}$$

Appendix B

CT Scans for Eagle Ford Shale Samples

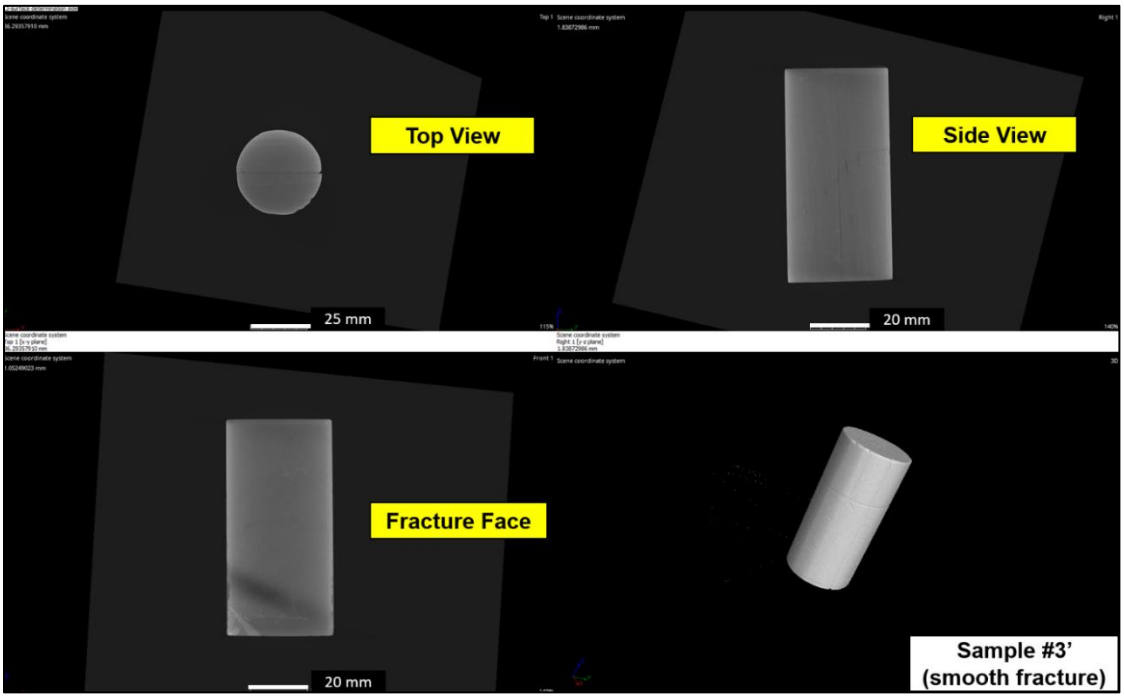

Figure *B*1: CT scan of Eagle Ford Sample #3', featuring a smooth fracture. The dark areas represent low-density or fractured regions, while the light areas indicate high-density zones.

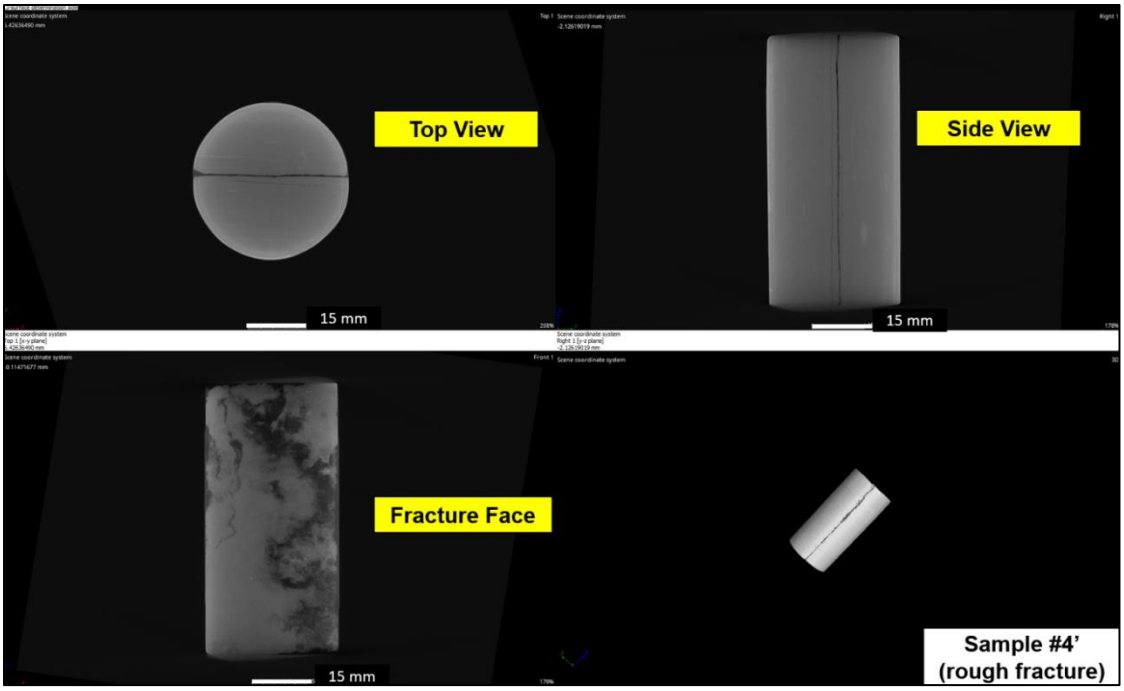

Figure *B*2: CT scan of Eagle Ford Sample #4', displaying a rough fracture. The dark areas correspond to low-density or fractured regions, while the light areas indicate high-density zones.

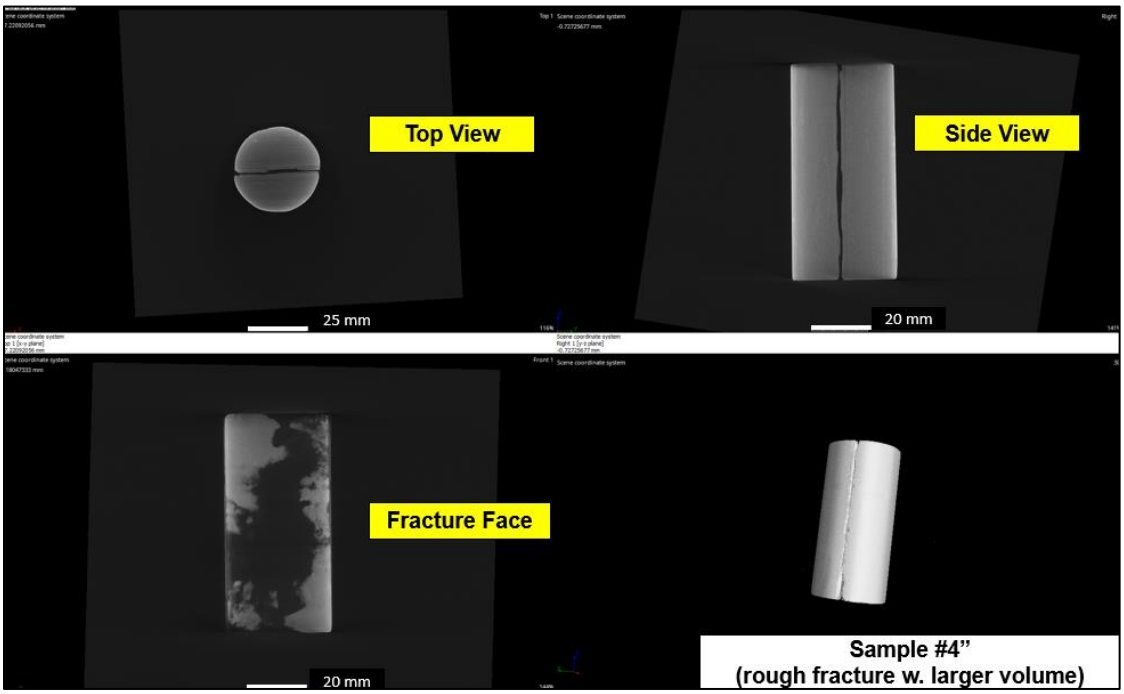

Figure *B*3: CT scan of Eagle Ford Sample #4", showing a rough fracture with larger volume. The dark areas represent low-density or fractured regions, while the light areas indicate high-density zones.

Appendix C

Extreme Gradient Boosting (XGBoost) Model

XGBoost is a sophisticated ensemble learning model that builds a sequence of decision trees to enhance prediction accuracy. In each iteration, XGBoost fits a new tree to the residuals from the previous tree and adds it to the model. The final prediction is a weighted sum of predictions from all trees, adjusted by a learning rate, as outlined in Equation (C1) (Bishop, 2006). For this model, the learning rate was set to 0.1. The hyperparameters include the number of trees, tested with values of 300, 400, 500, 600, 700, and 800, and the maximum tree depth, tested with values of 5, 10, and 15.

$$Y_{hi} = \sum_{t=1}^{T} \alpha_t Y_{ht} \quad \text{(C1)}$$

where α_t represents the learning weight for each tree (t).

K-Nearest Neighbors (KNN) Model

K-Nearest Neighbors (KNN) is another model that we utilized in our study, which predicts a continuous output by computing the distance (d) between a target point (p_i) and each of its nearest neighboring (K) points (q_i), then averaging their target K values (Bishop, 2006). The input and output data are first normalized to ensure equal influence of each feature using Equation (C2).

$$X_i = \frac{x_i - \mu}{\sigma} \quad \text{(C2)}$$

where X_i and x_i represent the normalized and unnormalized variables, respectively. σ is the standard deviation, and μ is the mean of the unnormalized variable.

The hyperparameters for this model include the number of neighbors (K) with values ranging from 2 to 10, and the distance metrics, which consist of Euclidean, Manhattan, Chebyshev, and Minkowski, as defined by Equations C3, C4, C5, and C6, respectively.

$$d_{Euclidean} = \sqrt{\sum_{i=1}^{n}(p_i - q_i)^2} \quad \text{(C3)}$$

$$d_{Manhattan} = \sum_{i=1}^{n}|p_i - q_i| \quad \text{(C4)}$$

$$d_{Chebyshev} = max_{i=1}^{n}|p_i - q_i| \quad \text{(C5)}$$

$$d_{Minkowski} = (\sum_{i=1}^{n}|p_i - q_i|^p)^{\frac{1}{p}} \quad \text{(C6)}$$

VITA

Sherif Elkholy

Candidate for the Degree of

Doctor of Philosophy

Dissertation: INVESTIGATION OF ACOUSTIC WAVES UNDER SUBSURFACE CONDITIONS TO IMPROVE THE PREDICTIONS OF ROCK MECHANICAL PROPERTIES AND NATURAL FRACTURE CHARACTERISTICS

Major Field: Petroleum Engineering

Biographical:

Education:

Completed the requirements for the Doctor of Philosophy in Petroleum Engineering at Oklahoma State University, Stillwater, Oklahoma in December, 2024.

Completed the requirements for the Master of Science in Petroleum Engineering at Heriot-Watt University, Edinburgh, United Kingdom in 2019.

Completed the requirements for the Bachelor of Science in Petroleum Engineering at Cairo University, Cairo, Egypt in 2010.

Experience:

- Reservoir Engineer Intern at Oxy, Houston, Texas: May-August 2023
- Geomechanical Engineer Intern at Oxy, Houston, Texas: May-August 2022
- Completions Engineer at Advantek, Houston, Texas: 2014-2019
- Applications Engineer at Advantek, Cairo, Egypt: 2011-2014

Professional Memberships:

- Society of Petroleum Engineers (SPE)
- Society of Exploration Geophysicists (SEG)